`

University of Southern Queensland

School of Engineering

Design of a Porous Femoral Stem to Reduce Stress Shielding in Total Hip Arthroplasty

A dissertation submitted by

Clay Twomey

in fulfilment of the requirements of

ENP4111 Professional Engineer Research Project

towards the degree of

Bachelor of Engineering Honours

2024

This page intentionally left blank

University of Southern Queensland

School of Engineering

ENP4111 Dissertation Project

(This is a 2-unit research project in Bachelor of Engineering Honours Program)

Limitations of Use

The Council of the University of Southern Queensland, its Academic Affairs, and the staff of the University of Southern Queensland, do not accept any responsibility for the truth, accuracy or completeness of material contained within or associated with this dissertation.

Persons using all or any part of this material do so at their own risk, and not at the risk of the Council of the University of Southern Queensland, its Faculty of Health, Engineering and Science or the staff of the University of Southern Queensland.

This dissertation reports an educational exercise and has no purpose or validity beyond this exercise. The sole purpose of this dissertation project is to contribute to the overall education within the student's chosen degree program. This document, the associated hardware, software, drawings, and other material set out in the associated appendices should not be used for any other purpose: if they are so used, it is entirely at the risk of the user.

Certification

I certify that the ideas, designs and experimental work, results, analyses and conclusions set out in this dissertation are entirely my own effort, except where otherwise indicated and acknowledged.

I further certify that the work is original and has not been previously submitted for assessment in any other course or institution, except where specifically stated.

Student Name: Clay Twomey

Student Number: [redacted]

[redacted]

_____

Signature

4/11/2024

Date

Abstract

This dissertation presents the design, simulation and analysis of a porous femoral stem to reduce the occurrence of stress shielding in Total Hip Arthroplasty (THA). Stress shielding occurs when rigid prosthetic structures prevent the natural elastic deformation of surrounding bone tissue that would normally stimulate the growth of new bone cells, resulting in a loss in bone density and increased risk of implant failure. This project introduces lattice-based porous structures within the femoral stem to replicate the elasticity of natural bone and reduce the occurrence of stress shielding.

Finite Element Analysis (FEA) was conducted on square, hexagonal and diamond-star lattice structures over a range of porosities to assess their mechanical performance. At the maximum tested porosity, the hexagonal and diamond-star lattices were able to achieve an elastic modulus lower than that of cortical femoral bone at 19.6GPa, indicating that they are suitable for use in a low elastic modulus femoral stem. Each lattice was incorporated into an in-situ porous femoral stem and FEA was conducted, measuring the occurrence of stress shielding. The hexagonal and diamond-star lattices reduced stress shielding to a maximum of 12% and completely negated stress shielding in some zones of the femur.

The results of the study show that hexagonal and diamond-star lattice-based porous femoral stems are highly effective in reducing the occurrence of stress shielding in THA, however, the surface cell layer is prone to failure and the proposed designs require further refinement.

Acknowledgements

I would like to thank my beautiful wife, Jessica, for her unwavering love and support throughout my studies. Thank you for being my chief proofreader, enduring the time I have spent locked away in the office, and listening with patience when I came to bed at midnight talking nonsense about lattices and strain. This achievement is as much yours as it is mine.

My sincere thanks go to my supervisor Dr Zachery Quince for his proactive guidance and constant availability for questions and feedback. His support greatly eased the challenges of this project and made the process feel much more manageable. Finally, I am grateful to my friends and peers whose valuable insights and willingness to discuss ideas were invaluable to my work at The University of Southern Queensland.

Contents

List of Tables

List of Figures

Nomenclature

Notation	Unit	Description
c	mm	Cell size
t	mm	Cell thickness
n		Number of cells
φ		Porosity
p	mm	Average pore size
F	N	Applied compressive force
A_{ave}	mm^2	Average cross-sectional area (excluding voids)
A_{total}	mm^2	Total cross-sectional area (including voids)
V_{ave}	mm^3	Average volume (excluding voids)
V_{total}	mm^3	Total volume (including voids)
σ_{max}	MPa	Maximum measured von Mises stress
σ_{min}	MPa	Minimum measured von Mises stress
σ_{VM}	MPa	Average von Mises stress
σ_c	MPa	Average analytically calculated normal stress
σ_{YY}	MPa	Measured normal stress
σ_a	MPa	Alternating stress
ε_{min}		Minimum measured strain in YY axis
ε_{max}		Maximum measured strain in YY axis
ε_m		Measured strain
ε_c		Displacement-calculated strain
ΔL	mm	Average vertical displacement of top face in YY axis
L_o	mm	Original length of cell or lattice
E	GPa	Elastic modulus of solid material
E_m	GPa	Measured equivalent elastic modulus
E_c	GPa	Calculated equivalent elastic modulus
K_m	%	Measured relative change in elastic modulus
K_c	%	Calculated relative change elastic modulus
S_e	GPa	Endurance limit
S_{ys}	MPa	Yield strength
N		Safety factor
SS	%	Stress shielding percentage

Glossary

Terminology	Description
AM	Additive Manufacturing
BCC	Body Centred Cubic
Bioactivity	The ability of a material to encourage bone cell growth on its surface.
Biocompatible	A material that is not harmful or toxic to living tissue.
Bioinert	A material that does not trigger a negative immune system response
CAD	Computer Aided Design.
Endoprosthesis	An artificial device placed inside the body to replace a body part removed by surgery.
FEA	Finite Element Analysis
Osteointegration	The fusing of a prosthetic component to living bone.
rTHA	Revisionary Total Hip Arthroplasty
SIMP	Solid Isotropic Material with Penalisation
SLS	Selective Laser Sintering
THA	Total Hip Arthroplasty
TPMS	Triply Periodic Minimal Surface
VM	von Mises

`

Chapter 1 Introduction

The objective of this project is to design a fully porous femoral stem to reduce the occurrence of bone density loss secondary to stress shielding and increase osteointegration in Total Hip Arthroplasty (THA) recipients. In THA the upper portion of the femur, the entire hip joint, and part of the hip bone are removed and replaced with prosthetic components. The prosthetic components are commonly made from stiff, inelastic alloys and ceramics which prevent the natural elastic deformation of the surrounding bone in a process known as stress shielding. This is particularly prevalent in the femur due to the long length of bone shielded by the femoral stem. The elastic deformation of bone tissue is the mechanism that triggers the growth of new bone cells which maintain bone density and strength. The stress shielding reduces the amount of new bone cells produced, resulting in lowered bone density and strength over time. The weakened proximal bone tissue leads to an increased chance of implant failure via ascetic loosening, periprosthetic fracture and misalignment dislocation, requiring revisionary surgery. Revisionary surgery leads to poorer patient outcomes, reduced mobility and increased risk of complications.

In this project, a fully porous lattice structure is incorporated into the femoral stem to increase the elasticity of the structure, reduce the occurrence of stress shielding, and allow for bone ingrowth. Three lattice types are tested for suitability through Finite Element Analysis (FEA), and their equivalent elastic modulus is measured over a range of porosities. The lattices are then incorporated into a sample in-situ femoral stem, and FEA conducted to measure the stress shielding in each implanted femur relative to its intact state.

Chapter 2 explores a detailed literature review focused on the significance of stress shielding, the factors effecting the occurrence of implant failure, and the current state of the art of endoprosthesis. Chapter 3 explains the methodology and rationale used to model, simulate and analyse various lattice and femoral stem types. Chapter 4 provides the results obtained from each FEA study and adjustments made to the initial methodology based on these observations. Chapter 5 explains the significance of the results, compares the findings of this project to existing work, and discusses the limitations of the study. Chapter 6 summarises the key findings of the project and provides recommendations for future work.

Chapter 2 Literature Review

THA is a commonly performed procedure that restores mobility and reduces the pain experienced by patients suffering from severe osteoarthritis. THA endoprosthesis have a high survivorship rate, however, over time revision surgery is often required due to implant degradation and failure. Revision surgery carries an increased risk of post-operative complications and yields poorer results than the initial procedure. Prolonging the lifespan of THA endoprosthesis and reducing the occurrence of unnecessary revision surgery is critical for ensuring the quality of life for those undergoing THA.

This literature review seeks to identify how the outcomes of THA can be improved through endoprosthesis design, with a focus on porous lattice femoral stems. The review will investigate current and historical trends in THA endoprosthesis design, the limitations of current THA outcomes, ongoing areas of THA endoprosthesis development and methods of mitigating stress shielding.

2.1 Background

2.1.1 Total Hip Arthroplasty

THA is a surgical procedure used to reduce pain and restore lower limb function to patients suffering from severe hip osteoarthritis (Mendiolagoitia et al. 2020). THA involves the complete replacement of the upper femur, hip socket and ball joint with internal artificial components (endoprosthesis), usually made from metals or ceramics (Patel et al. 2023). During the procedure, the femoral neck and head are removed, the core of the femur is bored out, the acetabular socket is widened and the prosthetic components are fixed to the bone using cementing compounds, screws or wedge-fit bone ingrowth (Katz et al. 2020). Figure 2-1 shows an example X-ray of a THA recipient with a cemented femoral stem.

Figure 2-1: X-Ray image of femur and hip after THA (Hacking, Worsley & Nicoletti 2023)

The first THA was conducted in 1951 using a cemented vitallium endoprosthesis design by E.J. Haboush. This first procedure reported poor results due to stress shielding of the bone. John Charnley introduced the modern THA endoprosthesis in 1962 and the basic design has remained largely unchanged (Markatos et al. 2020).

Modern hip prosthetics generally consist of four major modular components as indicated in Figure 2-2. The femoral stem, femoral head, acetabular cup, and acetabular cup liner. During THA, the top of the femur is removed, and a long cavity is bored out along the axis of the bone. The femoral stem is fixed within the cavity and the femoral head is attached to the upper neck of the femoral stem with a press fit. The acetabulum socket of the pelvis is

widened and houses the acetabular cup. The cup and head are almost always separated by a liner to reduce friction (Petis et al. 2015).

Figure 2-2: Schematic of common modern THA endoprosthesis designs (Crosby 2013).

2.1.2 Causes of Hip Prosthetic Failure

THA is becoming more common globally, and the average age of recipients is decreasing (Alontseva et al. 2023). Between 2011 and 2022, the number of THA recipients in the USA increased by 85% (Shanmugaraj et al. 2023). Younger patients have a more active lifestyle, so there is an increasing demand to maintain long-term mobility (Vickers et al. 2021).

Mendiolagoitia et al. (2020) used three-dimensional optoelectronic movement measurement to compare the gait kinematics of healthy individuals to those of pre-operative and post-operative THA recipients. It was found that THA produced a significant improvement in reported pain, hip and knee range of motion, step and stride length, walking speed, gait

pattern and support line symmetry when compared to the pre-operative state. However, when comparing post-operative THA recipients to healthy individuals, a decrease in all previously mentioned parameters was observed.

After receiving THA, patients reported increased difficulty performing actions such as walking and climbing stairs, with over 25% reporting an inability to participate in sports they previously played (Mendiolagoitia et al. 2020). In the short term, this can be attributed to post-surgery muscular damage (Vickers et al. 2021) and reduced range of motion (Chi et al. 2018), however long-term reduction in mobility is often attributed to the effects of stress shielding (Tan & van Arkel 2021).

Bone tissue relies on cyclic mechanical stresses to maintain its density and strength. When an endoprosthesis is made from a rigid material such as titanium, stainless steel, or ceramic, most of the loading that would normally be carried by the bone is transferred to the implant. The reduction of loading in the surrounding bone is referred to as stress shielding (Kharmanda 2016). Because the effected bone is not undergoing normal stresses, there is a resulting loss in bone density and strength. This compromises the mechanical integrity of the implant fixing and leads to aseptic implant loosening. Lowered bone density also increases the occurrence of peri-prosthetic fracture after THA (Arabnejad et al. 2017), which is the second most common cause of revision surgery, accounting for 18% of rTHA (Oltean-Dan et al. 2022). Over 60% of peri-prosthetic failure could be attributed to primary and secondary failure modes influenced by stress shielding (Emara et al. 2021).

Aseptic loosening is defined as a failure of fastening between an implant and tissue in the absence of infection (Puijk et al. 2023). Aseptic loosening occurs as a result of fatigue and deformation of fixings over time. Aseptic loosening is accelerated by particulate debris causing localised inflammation, known as osteolysis, but is most heavily effected due to loss

of bone density, known as osteopenia (Abu-Amer, Darwech & Clohisy 2007). The resulting misalignment further increases the occurrence of impingement dislocation (Chi et al. 2018). Aseptic loosening is the most common indication for revision surgery in THA (Vickers et al. 2021), and accounts for 52% of all revision surgeries conducted (Oltean-Dan et al. 2022).

2.1.3 Revisionary Total Hip Arthroplasty

Even with an extremely low failure rate, approximately 2 million revisionary total hip arthroplasty (rTHA) surgeries are carried out worldwide each year (Shanmugaraj et al. 2023). Reducing the occurrence of rTHA is critical to ensuring the highest quality of life to THA recipients. rTHA carries an increased risk of infection, prosthetic rejection, and delayed recovery time (Patel et al. 2023). The occurrence of peri-prosthetic fracture during, and post rTHA is increased, particularly in patients with decreased bone quality, as seen in osteopenia and osteoporosis (Wendler et al. 2022). Further, the occurrence of dislocation instability, and aseptic loosening are increased after rTHA (Patel et al. 2023). The increased recovery time associated with rTHA contributes to over 39% of recipients experiencing secondary complications post-surgery. Additionally, post-operative anaemia, hypertension (Patel et al. 2023), thrombosis, embolism and pneumonia (Wendler et al. 2022) are also commonly observed. Reducing the occurrence of rTHA is an ongoing area of research.

2.2 Areas of Current Research for Improving THA Outcomes

The following section will detail the current areas of research being conducted to improve hip prosthetic design and improve outcomes of THA recipients.

2.2.1 Surface Finishes

A prosthetic surface that mimics the mechanical, chemical, and geometric properties of bone is desirable for successful bone ingrowth (osteointegration). To reduce the chance of rejection, surface treatments can be applied to enhance the antibacterial, and bioactive surface properties of the endoprosthesis (Zhang, J. et al. 2022). The successful application and adhesion of surface finish is significantly improved on porous structures with rough surface finishes (Alontseva et al. 2023). High surface roughness increases the chance of bacterial infiltration and the amount of particulate debris created during the arthroplasty. Infiltration of particulate debris from implant surface damage may cause bone tissue necrosis, which contributes significantly to rejection rates (Alontseva et al. 2023). The effect of particulate debris is especially impactful when using a cemented implant (Emara et al. 2021).

2.2.2 Topology Optimisation

Topology optimisation is generally used to maximise stiffness of a component under loading conditions, but it may also be modified to maximise compliance while remaining below a stress threshold (Tan & van Arkel 2021). This is particularly useful in the design of low elastic modulus endoprosthesis. Tan and van Arkel (2021) demonstrate a Solid Isotropic Material with Penalisation (SIMP) algorithm, which has been modified to maximise the elasticity of a femoral stem, without loss in bearing load. Lu and Chen (2013) used topology optimisation to decrease the weight, increase the elastic properties, and ensure even stress distribution of a new compliant component within a knee prosthetic. There are numerous topology optimisation techniques that have been developed, however, SIMP is the most common type seen in commercial software (Kharmanda 2016). The bespoke geometry created by topology optimisation is enabled by advancements in additive manufacturing.

2.2.3 Advancements in Prosthetic Manufacturing

The onset of modern Additive Manufacturing (AM) techniques has allowed the design and production of prosthetic components with intricate internal cellular structures and complex geometries (Tan & van Arkel 2021).

Plasma spraying is an emerging technology that has been used to create porous femoral stem prototypes with complex geometries and controlled biocompatible surface coatings. Selective Laser Sintering (SLS) is an AM process that allows components to be directly constructed from hydroxyapatite powder, the major inorganic compound found in mammalian bones, encouraging high levels of osteointegration (Alontseva et al. 2023).

Titanium alloys are commonly used in biomedical AM applications. Titanium, Aluminium and Vanadium (Ti_6Al_4V) lattice structures have been manufactured with a range of AM techniques, such as electron beam melting, SLS and laser powder bed fusion (Zhang, Y. et al. 2022). The method of manufacture can also effect the mechanical properties of the finished component. Hezil et al. (2022) found the sintering temperature of SLS effected the phase distribution of Ti_6Al_7Nb grain structure which had a significant impact on the elastic modulus of the finished component.

Although there are a wide range of manufacturing techniques appropriate for porous lattice stems, there are currently none in commercial production (Liu et al. 2021). AM reduces waste but generally increases the component cost due to the software, equipment and expertise required (Alontseva et al. 2023). When using AM for biomedical applications, there are further limitations that must be considered. During the sintering process of powdered alloys, some unmelted particles will remain. Over time the loose particles will dislodge in the body and cause osteolysis in the surrounding tissue (Hezil et al. 2022).

2.2.4 Endoprosthesis Fixing Methods

The femoral stem is commonly fixed to the femur using a cementing compound or by relying on taper fit wedging (Emara et al. 2021). The use of screws and pins in the femur is generally avoided as their use increases the chance of periprosthetic fracture during surgery (Wendler et al. 2022). Porous structures allow for an improved cement bone interface and cement penetration, increasing the rate of bonding (Katz et al. 2020). The preference for cementless or cemented femoral stem varies by country, however cementless is more common in New Zealand and the United Kingdom (Emara et al. 2021).

A study carried out by Katz et al. (2020) found that uncemented femoral stems are more likely to require early revision surgery due to higher rate of aseptic loosening and post-operative fractures. Wendler et al. (2022) found cemented stems were able to rapidly achieve a high level of primary fixation, allowing for early mobilisation of the patient (Wendler et al. 2022). The rigid bond between the bone and prosthetic mantle of cemented stems has been shown to reduce short term aseptic loosening at the cost of increasing the long term effects of stress shielding (Corona-Castuera et al. 2021). Cemented implants are preferred for patients with already poor bone quality, particularly elderly females (Emara et al. 2021). For patients with good existing bone quality, the effects of cementing on stress shielding should be considered.

2.3 Stress Shielding

In THA, stress shielding is most prevalent in the lengthy bone-prosthetic interface between the femoral stem and femur (Arabnejad et al. 2017). This area is most effected by the transfer of normal loading to the rigid prosthetic. Rigid stem structures change the typical

compressive loads of the femur to shear stresses in the contact zone between the implant and bone (Alontseva et al. 2023).

Due to the complex loading conditions and geometry of the hip joint and femoral stem, there is not currently an agreed upon method of measuring the occurrence of stress shielding. There are various methods used in previous studies such as von Mises, principal and energy density stress and strain methods (Emara et al. 2021). Emara et al. (2021) propose an algorithm for calculating proximal stress shielding in the femur, however the authors highlight the need for experimental validation of theoretical stress measurement. Arabnejad et al. (2017) use a method of identifying 75 predetermined sample points across the femur to calculate stress shielding and preserve stress distribution measurement. Liu et al. (2021). Propose a simplified method of calculating the relative change in average stress using FEA and analytical calculations.

Altering component geometry to change loading conditions has been used to reduce the effect of stress shielding in previous research. Reduction in stem length, the inclusion of collars, stem grooves and tapered sections have been used to encourage greater load transfer to the surrounding femoral region and reduce shear stress concentration (Arabnejad et al. 2017). de Waard et al. (2021) conducted a systematic literature review and concluded that short femoral stems increased loading in the femur and reduced proximal bone loss by up to 15% over two years.

Many approaches to reduce occurrence of stress shielding focus on increasing elasticity of the component (Arabnejad et al. 2017). The elastic modulus of the endoprosthesis needs to be reduced below 19GPa to match that of bone (Hedayati & Fallah 2015). Low elastic modulus alloys have been developed, but it remains challenging to maintain the required load bearing properties and biocompatibility (Wang et al. 2021).

Increasing the bulk porosity of a structure is a commonly proposed method for decreasing the elastic modulus (Cilla, Checa & Duda 2017), and has been a particular focus in biomedical applications (Alontseva et al. 2023). Porous structures allow the continued use of biocompatible, mechanically stable, and proven materials while reducing the effects of stress shielding.

2.3.1 Porous Structures

Porous structures have been used with great success in biomedical applications. The modern generation of highly porous titanium alloy acetabular cups have a 99.3% survivorship rate after 10 years (Emara et al. 2021). The application of porous structures in the femoral stem is still the subject of research.

Liu et al. (2021) conducted a systematic review of porous lattice structures for femoral stems. The key features of lattice structures are controlled stiffness, high strength, isotropy and the ability to promote bone ingrowth. The ability to decrease the elasticity of the femoral stem, without sacrificing its strength makes porous lattice structures ideal for combating the effects of stress shielding. The lattice type (Tan & van Arkel 2021), average pore size, bulk porosity and relative density distribution are independent factors that can be adjusted to change the mechanical properties of a structure (Zhang, Y. et al. 2022). Figure 2-3 shows the relationship between elastic modulus, yield strength and porosity observed in a study of porous lattices by Mehboob et al. (2020).

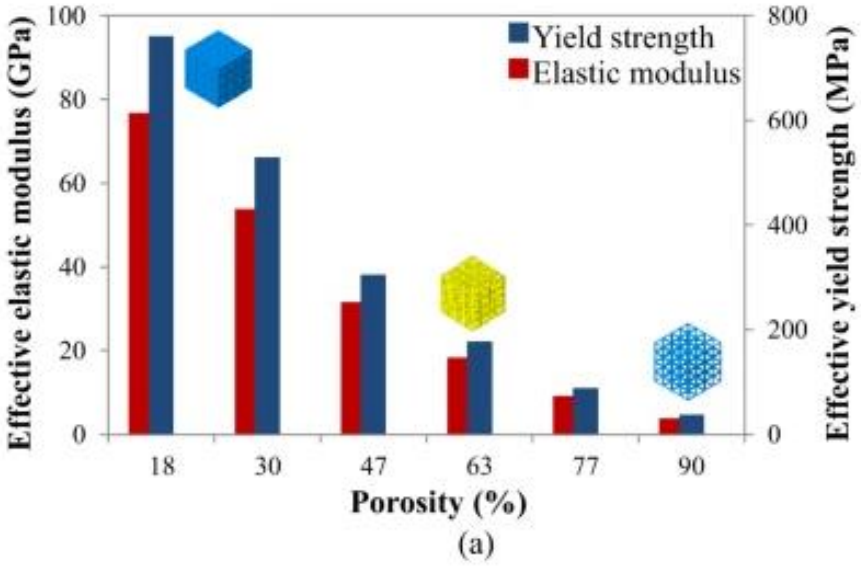

Figure 2-3: Change in effective elastic modulus and yield strength of BCC lattice at various porosities (Mehboob et al. 2020)

Cubic node arrangements are a commonly observed lattice structure. Body Centred Cubic (BCC), body-centred tetragonal, face-centred cubic, attached face-centred cubic, (Zhang, Y. et al. 2022) tetrahedral, (Tan & van Arkel 2021) and diamond structures, have been used in previous studies to form the femoral stem (Corona-Castuera et al. 2021). Cubic node structures are generally isotropic and have high strength, however, they commonly share the issue of stress concentration at node intersections, reducing the load bearing capacity (Liu et al. 2021). Tan and van Arkel (2021) propose a stochastic porous and selectively hollowed femoral stem structure, to reduce the occurrence of stress shielding. The authors were able to reduce the equivalent stiffness of the structure by approximately 40%. Jetté et al. (2018) used a diamond lattice, with an average pore size of 800µm and porosity of 68% to achieve 15% stress shielding, a reduction of 30% compared to a solid stem. Zhang, Y. et al. (2022) found that an optimal increase in elasticity while minimising reduction in yield strength of a Ti_6Al_4V cubic strut was at an average pore size of 600-700µm, as shown in Figure 2-4.

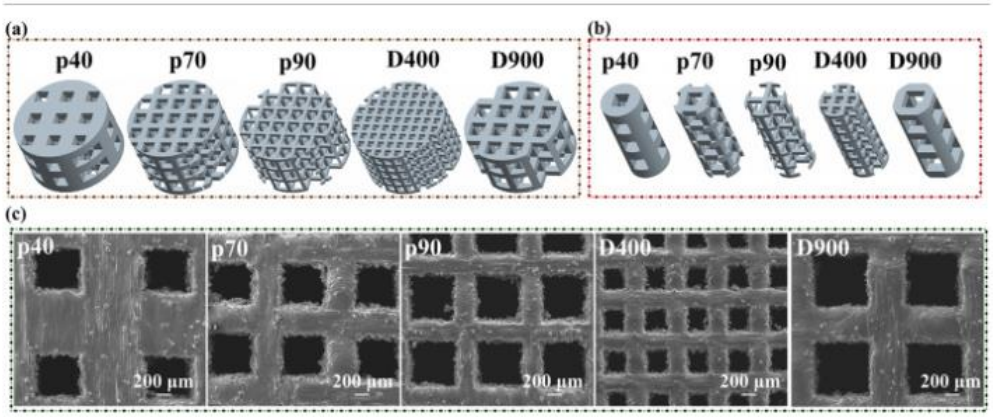

Figure 2-4: Cubic lattice samples of various porosities (Zhang, Y. et al. 2022)

The density, pore size and type of lattice structure can be varied to match the bone density distribution present in natural bone (Liu et al. 2021). This allows the elasticity of the structure to be maximised where load bearing requirements are lower. A limitation with variable density is that non uniform and sheet network lattice structures are more prone to failure as there is stress concentration at geometric discontinuities between layers or structures (Zhang, Y. et al. 2022). Arabnejad et al. (2017) present a design for a fully porous femoral stem with a density optimised tetrahedron lattice, as seen in Figure 2-5. The authors found that at an average pore size of 500μm, bone loss due to stress shielding could be theoretically reduced by up to 75%, when compared to a solid titanium implant. Fraldi et al. (2010) used topology optimisation to for a variable density femoral stem that was able to completely negate stress shielding across some portions of the femur.

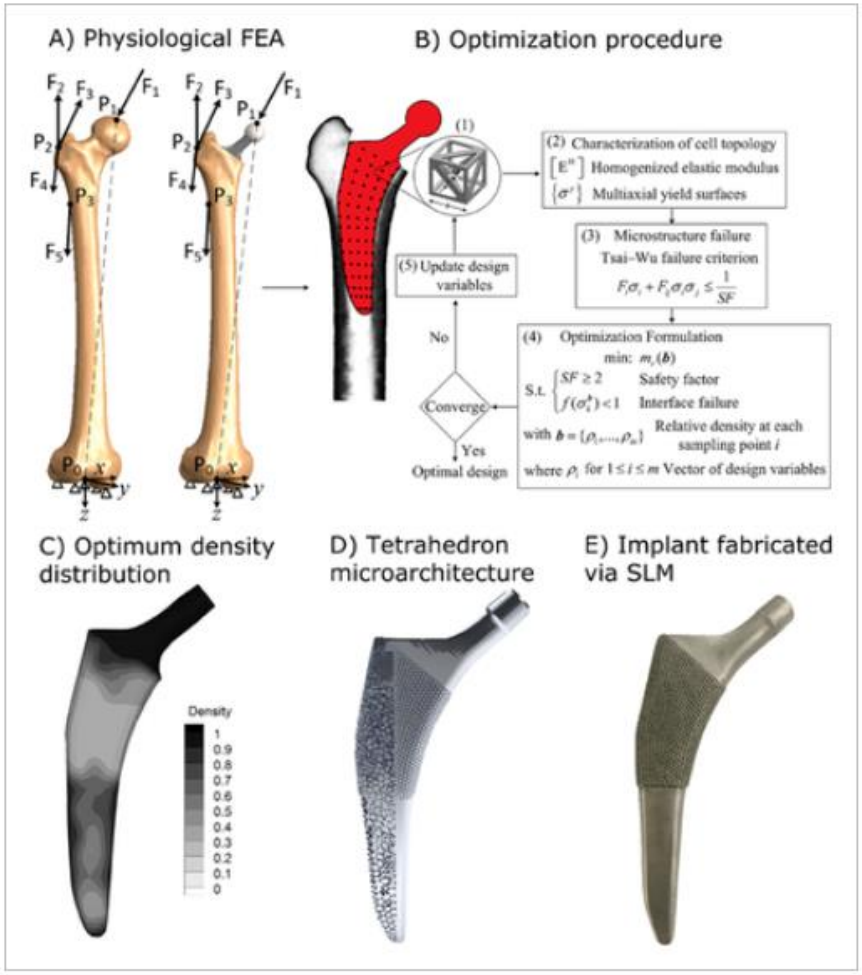

Figure 2-5: Example of tetrahedron lattice with optimised density distribution (Arabnejad et al. 2017)

The use of Triply Periodic Minimal Surface (TPMS) porous structures in the femoral stem has been proposed in many studies to improve on the properties of cubic node lattices. TPMS have continuous zero-mean curvature geometry, and highly interconnected pores, which allow for high strength and fatigue resistance, while reducing the occurrence of stress concentration (Zhang, Y. et al. 2022). Zhang, J. et al. (2022) tested TPMS of constant and linearly changing layer height and found that varying the layer height could be used to alter the localised mechanical properties of the structure, as seen in Figure 2-6.

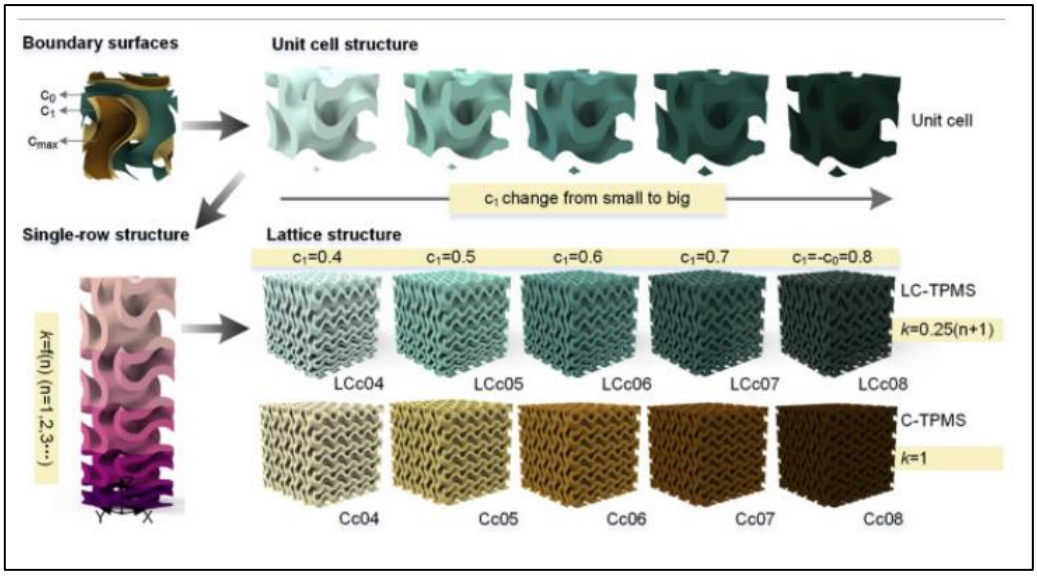

Figure 2-6: Example of Triply periodic minimal surface structures at variable porosity (Zhang, J. et al. 2022)

Porous structures provide a greater bonding surface area and allow the implant to be secured through osteointegration, where surrounding bone grows into the voids of the implant, resulting in a strong adhesion without the need for cementing or additional fasteners. As this is almost exclusively a surface interface phenomenon, only the porosity of the outer 700µm is considered significant for osteointegration (Alontseva et al. 2023). High porosity titanium alloy outer layers, with an average porosity of up to 70%, have been shown to achieve optimal levels of osteointegration, with pore sizes in the range of 100–700µm (Zhang, Y. et al. 2022). Irregular pore size has been shown to promote greater integrated bone growth and have superior mechanical properties (Wang et al. 2021).

Alontseva et al. (2023) conducted a literature review on the current state of porous coatings. The authors identified a lack of surface roughness and porosity standards under the International Organization for Standardization for medical implants, because they are an area of ongoing research. The authors highlight that further research needs to be conducted into developing novel designs for titanium scaffolds.

A review conducted by Tan and van Arkel (2021) highlighted the practical limitations of lattice structures. In small scale lattices, thin components with sharp edges become impractical to use during surgery and risk damage to the implant or bone. There has been no in vivo testing of porous stems on humans and limited testing in mammals, so the computational analysis of stress shielding still requires further validation. The effect of muscle and micromovement in the stem bone interface is often not considered, with most studies focused on porous stems not considering the effect of geometric properties in addition to elastic modification (Tan & van Arkel 2021). The type, size and distribution of porous lattice used in the femoral stem is intrinsically linked to the material it is made from.

2.3.2 Material Selection

The specific functionality of each prosthetic component requires different material properties to be considered. Hip prosthetics are required to last more than 10 years and undergo an average of 2.2 million gait cycles per year (Kinkel et al. 2009), with THA found to last 25 years in 58% of patients (Evans et al. 2019). The required service life means high strength, fracture toughness and fatigue resistance are important for all load bearing structural components. All materials should be corrosion resistant and biologically inert to ensure biocompatibility and reduce risk of inflammation or infection.

Articulating surfaces require high wear resistance and low coefficients of friction with good wetting properties, to avoid debris causing periprosthetic inflammation. Bishop, Waldow and Morlock (2008) conducted testing of material pairings for the hip socket ball joint. They found that ceramic on ceramic produced the lowest frictional moment and metal on metal surfaces produced the highest.

Where the prosthetic is interfacing with the bone, separate outer layers may be applied to alter biocompatibility while the structural scaffold may be made of a material with better mechanical properties. High bioactivity is desirable for osteointegration and cell growth, while particulate toxicity should be minimised (Alontseva et al. 2023).

Rahaman et al. (2007) found that most knee and hip joint replacement consisted of titanium alloy (Ti_6Al_4V) structural components and Alumina (Al_2O_3) bearing surfaces separated by ultrahigh-molecular-weight polyethylene liners. In 2023, the trend of metal and ceramic componentry has continued with titanium alloys, hydroxyapatite, zirconium, and tantalum being common materials for prosthetics (Alontseva et al. 2023).

Titanium

Titanium is by far the most popular structural scaffolding material, with the lowest component failure rate. In the USA, 89% of titanium alloy THA implants are over 10 years old. Titanium alloy is desirable for biomedical applications because of its high corrosion resistance, hardness and tribological properties compared to stainless steel and Co-Cr alloys. Of the Titanium alloys, Ti_6Al_4V is the most commonly used in endoprosthesis (Hezil et al. 2022).

A systematic review conducted by Liu et al. (2021) found that Ti_6Al_4V was the most viable alloy for constructing porous 3D lattice structures for femoral stems. It retains high strength at high bulk porosity and can be used in a wide range of modern AM techniques. The formation of a passive oxide outer layer on titanium alloys provides a corrosion resistant bioinert barrier (Alontseva et al. 2023). If this layer experiences wear due to frequent frictional movement, toxic vanadium and aluminium ions are released. Niobium has been proposed as an alternative non-toxic alloying compound due to its bioinert properties, but it has not been tested in vivo (Liu et al. 2021).

Ceramics

Ceramics are characterised as having high hardness, wear resistance, chemical inertness, and biocompatibility (Paulsen et al. 2024). The major drawback of ceramics is their brittleness and low fracture toughness, leading to increased risk of catastrophic in vivo bearing failure. This is rarely observed in practice due to modern ceramic compounds and advanced manufacturing processes providing excellent material properties (Rahaman et al. 2007).

Traditional monolithic ceramic oxides such as Al_2O_3 and stabilized zirconia (ZrO_2) have historically been the most common ceramics used in prosthetics (Lehil & Bozic 2014). Modern ceramic composites and surface modified refractory compounds provide much higher mechanical properties without sacrificing fracture toughness (O'Dwyer Lancaster-Jones & Reddiough 2023). The inclusion of Si_3N_4 can be used to create a passive oxide layer, phase mixed and nanocomposite ceramics increase fracture toughness and hard surface coatings such as titanium nitride or diamond-like carbon can be used to increase fatigue and wear resistance (Rahaman et al. 2007).

Modern manufacturing techniques allow the phase composition and distribution, micro and grain structure of ceramics to be controlled with high precision, allowing for the production of bio ceramics that comfortably exceed the material requirements of orthopaedic implants (Rahaman et al. 2007). The characteristic high stiffness of ceramics limits their use in elastic porous structures, and the required manufacturing techniques prevent the formation of complex geometry.

Polymers and Fibre Composites

Polymers and fibre composite materials are rarely used in load bearing components of endoprosthesis (Emara et al. 2021) because they are unable to withstand the repetitive loading

without undergoing plastic deformation. Composite materials often have poor fatigue strength and some composites do not show a fatigue limit (D'Amore & Grassia 2019). Additionally polymers generally have a lower bio inertness, and higher particulate toxicity (Stewart et al. 2019).

2.4 Conclusion

The increasing number of THA recipients and their decreasing age highlights a growing need to prolong the lifespan of hip endoprosthesis and reduce occurrence of rTHA. rTHA increases the risk of post-operative complications, and yields poorer overall results compared to the initial procedure. Current THA endoprosthesis use a solid titanium or stainless-steel alloy femoral stem, leading to long term loss of bone density through stress shielding. The resulting loss in bone density has been identified as a major contributor to aseptic loosening, impingement dislocation and periprosthetic fracture, which account for over 70% of rTHA procedures.

There has been a substantial amount of research conducted into how to prevent stress shielding of the femoral stem. Altering the geometry of a rigid stem has yielded limited success. The research indicates that lowering the stem's elastic modulus to match that of the surrounding bone is an effective way to reduce stress shielding. This may be achieved through material selection or increasing the bulk porosity of the structure. Material selection is limited by biocompatibility and manufacturing restrictions. Porous lattice strictures have been identified as a viable option for constructing low elastic modulus femoral stems, while maintaining the required material properties. Various lattice structures have been tested, however, there are currently no commercially produced fully porous femoral stems. There exists a need to further test and validate lattice designs to move fully porous femoral stems from theory to practical application.

Chapter 3 Methodology

3.1 Introduction

The following methodology details the steps taken to design, model, simulate and analyse a femoral stem which utilises a porous 3D lattice to reduce the effect of stress shielding and maximise osteointegration in THA. This was achieved in three stages.

The first stage focused on investigating and validating alternate methods and factors effecting the FEA and calculation of elastic modulus for lattice samples. A simple square unit cell and small lattice samples were modelled in Creo Parametric. FEA was then conducted in Creo Simulate and the results were compared against analytical calculations to validate the method. The effect of the number of cells in the sample, method for measuring stress and method for calculating elastic modulus were analysed and refined.

The second stage expanded the analysis to investigate the properties of alternate lattice types. A range of lattice samples were generated and analysed through FEA while varying the porosity. The elastic modulus was calculated at each porosity, indicating the lattice's suitability for use in a porous femoral stem. As identified in Chapter 2.4, reducing elastic modulus of a prosthetic component will reduce the effect of stress shielding in the surrounding bone. Additionally, the average cell size and porosity were calculated to indicate the effectiveness of the lattice for encouraging osteointegration.

The final stage focused on applying the lattice sample findings in a scale test of a porous femoral stem to measure the occurrence of stress shielding. A series of solid and fully porous femoral stems were modelled within a simulated femur under an example working load. FEA was conducted to measure the stress shielding percentage of the implanted femur compared

to an intact, unimplanted femur. A lower stress shielding percentage indicated a stress distribution closer to that of an intact femur, indicating a more successful lattice design.

The methodology used in this report was adapted from components of the systematic literature review conducted by Liu et al. (2021). This review consolidates the various methods for modelling and analysing porous femoral stems used in over 50 previous studies. Due to software limitations, numerous revisions were made to the initially planned methodology. The overall scope of the project was reduced, and further simplifications were made to allow for the conduct of analysis. The changes and rationale are discussed in further detail in this chapter.

3.2 Material and Access Requirements

The resources required for this project are shown in Table 3-1. As the results of the project were obtained using FEA, no physical testing was required. This limits the material and access requirements exclusively to computers and software. It is assessed there was no requirement to physically access University of Southern Queensland facilities during the conduct of the project.

Table 3-1: Resources and access requirements.

Task	Equipment	Source
General conduct	PC capable of running FEA simulations	Provided by author
	Microsoft Windows licence	Provided by author
	Microsoft Word	Provided by author
	Microsoft Excel	Provided by author
Conduct solid modelling	Creo Parametric access	Provided by University of Southern Queensland
Conduct FEA	Creo Simulate access	Provided by University of Southern Queensland
Conduct result analysis	MATLAB	Provided by author

3.3 Risk Analysis

A Workplace Health and Safety (WHS) risk assessment has been raised and approved in the SafeTrak WHS risk register to cover the conduct of this project. As the project is a desktop study, no additional control measures were required beyond the existing control measures implemented in the workspace. The full risk assessment can be found in Appendix C.

3.4 Modelling

The following section details the methods used to model, simulate and analyse the various lattice structures prosthetic components.

3.4.1 Square Unit Cell Modelling

The core component of a regular porous lattice structure is the individual unit cell (Yang et al. 2020). The unit cell represents the smallest repeating structure used to form the greater lattice. To check the validity of the modelled results, first a simple square unit cell was modelled in Creo Parametric using solid geometric features, as pictured in Figure 3-1. The simple geometry of this cell type allowed for analytical calculations to be conducted, and the results compared to the model data for validation.

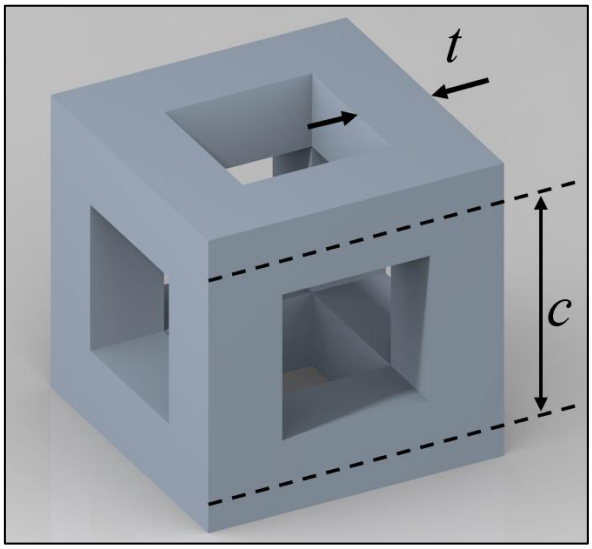

Figure 3-1: Square unit cell

The average porosity (φ) of the cell was controlled by altering the strut thickness (t) and cell size (c). φ was calculated as per Equation 3-1 (Arabnejad et al. 2017).

$$\varphi = \frac{V_{voids}}{V_{total}} = \frac{V_{total} - V_{model}}{V_{total}} \qquad \textit{Equation 3-1}$$

Where V_{voids} is the volume of voids, V_{total} is the total volume of the unit cell including voids, and V_{model} is the volume of the unit cell excluding voids.

V_{total} and V_{model} were calculated analytically as per Equation 3-2 and Equation 3-3 respectively, given that the corner nodes lay on the central axis of each strut.

$$V_{total} = (nc + t)^3 \quad \textit{Equation 3-2}$$

$$V_{model} = nt^2(c - t)(n + 1)^2 - t(n^2(c - t)^2 - (t + cn)^2)(n + 1) \quad \textit{Equation 3-3}$$

Where *n* is the number of cells along each axis of the square lattice.

Although V_{model} of the square unit cell was able to be calculated analytically, the complex geometry of subsequent cell types makes the calculation difficult. To set the conditions for calculating the porosity of more complex structures further in the methodology, V_{model} was recorded directly from the Creo model using the volume measurement tool. It was confirmed that the analytical value and modelled value were equal.

The average pore size (*p)* for each sample was calculated as per Equation 3-4.

$$p = c - t \quad \textit{Equation 3-4}$$

A porosity of up to 70% (Alontseva et al. 2023), and pore size between 100–700 μm have been identified as optimal for bone ingrowth (Arabnejad et al. 2017; Wang et al. 2021; Zhang, J. et al. 2022). To optimise these values, a parametric relationship was established in the model for strut thickness and cell size. An initial average cell size of 500μm was selected and the strut thickness varied to produce 5 sample cells with porosity within the range of $0.5 < \varphi < 0.9$.

3.4.2 Square Unit Cell Simulation

As noted in Chapter 2, specific material properties are required for use in endoprosthesis components. The material used for all analysis was Ti_6Al_4V with an elastic modulus (E) of 114GPa. The femoral stem requires a chemically inert material with low toxicity, high corrosion resistance for biocompatibility and high strength, fracture toughness, fatigue and wear resistance for the required longevity. Additionally, the material needs to be usable in AM processes to create the complex geometry of a porous lattice. Ti_6Al_4V fulfils all the required criteria, and has the lowest elastic modulus compared to other commonly used materials such as cobalt alloys at E = 230GPa, and stainless steels at E = 210GPa (Bliss et al. 2023). The material properties of Ti_6Al_4V were obtained from a datasheet sourced from MatWeb (2024). The project objectives were achieved using Ti_6Al_4V, so further analysis of alternate materials was not required.

To simulate the initial loading conditions, a compressive load of 4kPa was applied along the vertical YY axis to the top surface of the cell, and the displacement of the lower surface of the cell was fixed. The simplified loading allowed for analytical stress calculations to be conducted and compared against simulated results. The value of 4kPa was selected to represent an above average working load of 200kg, supported by an average 25mm diameter femur (Shanto et al. 2024).

A mesh was generated, the simulation was run, and mesh refinement was attempted. Due to the small element sizes and sharp internal corners of the structure, any reduction in maximum element size beyond the default resulted in stress singularities. The maximum stress did not converge on a single value and increased exponentially as element size was reduced. This could have been alleviated by adding rounds to the internal corners to avoid stress concentration points, however this would not be viable for use in subsequent tests involving

large numbers of cells, and tests involving the use of the automatic lattice feature. The default mesh was used for all subsequent tests.

The FEA simulation was run, and the results were recorded as per Table 3-2:

Table 3-2: Recorded data for lattice testing

Measurement	Notation	Units
Maximum model VM stress	σ_{max}	MPa
Minimum model VM stress	σ_{min}	MPa
Measured normal stress	σ_{YY}	MPa
Maximum model strain	ε_{max}	unitless
Minimum model strain	ε_{min}	unitless
Maximum displacement of upper surface	Δy_{max}	mm
Minimum displacement of upper surface	Δy_{min}	mm

Three methods for calculating stress were investigated and compared for validity. The measured normal stress (σ_{YY}) was recorded directly from the FEA results. The mean measured VM stress (σ_{VM}) was calculated based on minimum and maximum model VM stress values as seen in Equation 3-5. The average analytically calculated normal stress (σ_c) was determined based on the applied force and average cross-sectional area of the lattice as per Equation 3-6. Further, the assumption that $A_{ave} = A_{total}(1-\varphi)$ was checked analytically and shown to be true.

$$\sigma_{VM} = \frac{\sigma_{max} + \sigma_{min}}{2} \qquad \textit{Equation 3-5}$$

$$\sigma_c = \frac{F}{A_{ave}} = \frac{F}{A_{total}(1-\varphi)} \qquad \textit{Equation 3-6}$$

Where F is the applied load, A_{ave} is the average cross-sectional area of the structure, A_{total} is the cross-sectional area of the entire unit cell including voids, and φ is the porosity.

The absolute values and relative error between the three methods of stress calculation (σ_{VM}, σ_{YY}, and σ_c) was calculated and compared. σ_{max} was checked to be under the materials yield strength of 1070 MPa (MatWeb 2024).

Two methods for calculating strain were carried out and compared for validity. The mean measured strain (ε_m) was calculated as per Equation 3-7, using directly measured minimum and maximum strain values. Alternatively, a displacement-focused approach was used to determine displacement-calculated strain (ε_c) as seen in Equation 3-8 and Equation 3-9.

$$\varepsilon_m = \frac{|\varepsilon_{max}| + |\varepsilon_{min}|}{2} \qquad \textit{Equation 3-7}$$

$$\Delta L = \frac{\Delta y_{max} + \Delta y_{min}}{2} \qquad \textit{Equation 3-8}$$

$$\varepsilon_c = \frac{\Delta L}{L_o} \qquad \textit{Equation 3-9}$$

Where ΔL is the total change in length and L_o is the original length of the lattice.

The relative error between ε_m and ε_c was calculated and compared to assess the validity of each method.

Two methods for determining the effective elastic modulus (E) were carried out and compared for validity. The measured elastic modulus (E_m) was calculated based on the mean VM stress and mean measured normal stress as per Equation 3-10. The calculated effective elastic modulus (E_c) was determined based on the analytical average normal stress and displacement calculated stress, as per Equation 3-11.

$$E_m = \frac{\sigma_{VM}}{\varepsilon_m}$$ *Equation 3-10*

$$E_c = \frac{\sigma_c}{\varepsilon_c}$$ *Equation 3-11*

The measured relative change in elastic modulus (K_m) was determined as per Equation 3-12. The calculated relative change elastic modulus (K_c) was determined for comparison, as per Equation 3-13. These values were used to quantify the effectiveness of the unit cell in increasing elasticity compared to a solid material.

$$K_m = 100\ \frac{E_m - E}{E}$$ *Equation 3-12*

$$K_c = 100\ \frac{E_c - E}{E}$$ *Equation 3-13*

Where E is the elastic modulus of the solid material.

3.4.3 Square Lattice Modelling and Simulation

Once the results for the square unit cell were analysed, the model was scaled up to simulate a small sample of a square lattice structure consisting of a regular repeating structure of the unit cells, as seen in Figure 3-2. The lattice was generated as solid geometry using the pattern tool in Creo Parametric.

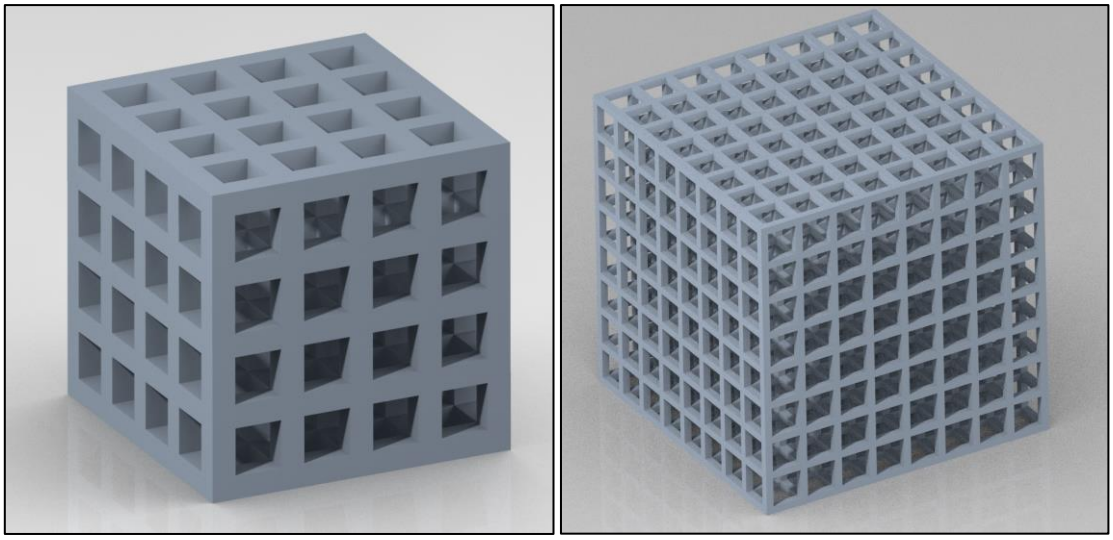

Figure 3-2: left: $n = 4$ square lattice, right: $n = 8$ square lattice

To test the effect that the number of cells within the lattice has on the results, two variations of n^3 cells were generated, where n is the number of cells along each axis. First, an $n = 4$ lattice was generated. It was noted that if the strut thickness remained constant as the number of cells was increased, the porosity also increased. The formula describing the porosity of a square lattice as a function of cell size, strut thickness and number of cells was derived as Equation 3-14. This analytically derived formula was checked against the measured value of porosity described by Equation 3-1 and shown to be correct.

$$\varphi = \frac{(t+cn)^3 + t(c^2(n-t)^2 - (t+cn)^2(c+1) - ct^2(n-t)(c+1)^2}{(t+cn)^3} \qquad \textit{Equation 3-14}$$

The same procedure used to analyse the unit cell was repeated for the lattice sample. The FEA simulation was run and σ_{max}, σ_{min}, σ_{YY}, ε_{max}, ε_{min}, Δy_{max} and Δy_{min} were recorded.

The measured E_m and K_m were compared against the calculated E_c and K_c, as well as the previous the values obtained from the unit cell analysis. The strut thickness was varied to produce 5 sample lattices with porosity within the range of $5 \leq \varphi \leq 0.9$ and the analysis was repeated. The analysis was repeated for a $n = 8$ lattice, and the results recorded and compared.

3.4.4 Hexagonal and Diamond-star Lattice Modelling and Simulation

A set of alternate lattices were generated for analysis using the previously stated methodology. Initially the intent of this project was to create custom novel lattice types based on gyroids, helical and curved beams, using patterned unit cells as was done with the square cell lattice. This operation proved too complex for the software to perform and resulted in constant crashing. Multiple attempts were made to simplify geometry, combine features and generate the lattice in sections to avoid overwhelming the software but these efforts yielded limited success.

To alleviate the issue of pattern generation, the inbuilt automatic lattice feature was used. The formula driven gyroid lattice feature only generated voxelated objects which could not be used in Creo Simulate for FEA. Numerous attempts were made to convert the voxelated features into solid bodies such as shrink wrapping, copying geometry to use a template for new parts, solidifying and processing in external software, however these attempts were unsuccessful. Using the custom cell function of the lattice feature, a full geometry custom lattice was generated based on curved struts. The software was, however, unable to mesh the lattice sample, again resulting in constant crashes. The curved structure resulted in a large number of elements being generated and attempts to reduce this number yielded limited success. It was noted that using a full geometry model for FEA testing was not viable at scale, considering how many cells were required for the subsequent full femoral stem tests.

The only viable option was to use the beam lattice type, which could be generated with simplified geometry especially designed for use in FEA and as full geometry at small sample scale. This reduced the scope of the project considerably to only analyse straight beam-based lattices.

Two beam-based lattice types were selected for testing, as seen in Figure 3-3. A hexagonal honeycomb-like structure, and diamond-star truss were generated as full geometry using the lattice feature. The alternate lattice designs were modelled and simulated as $n = 4$ lattices.

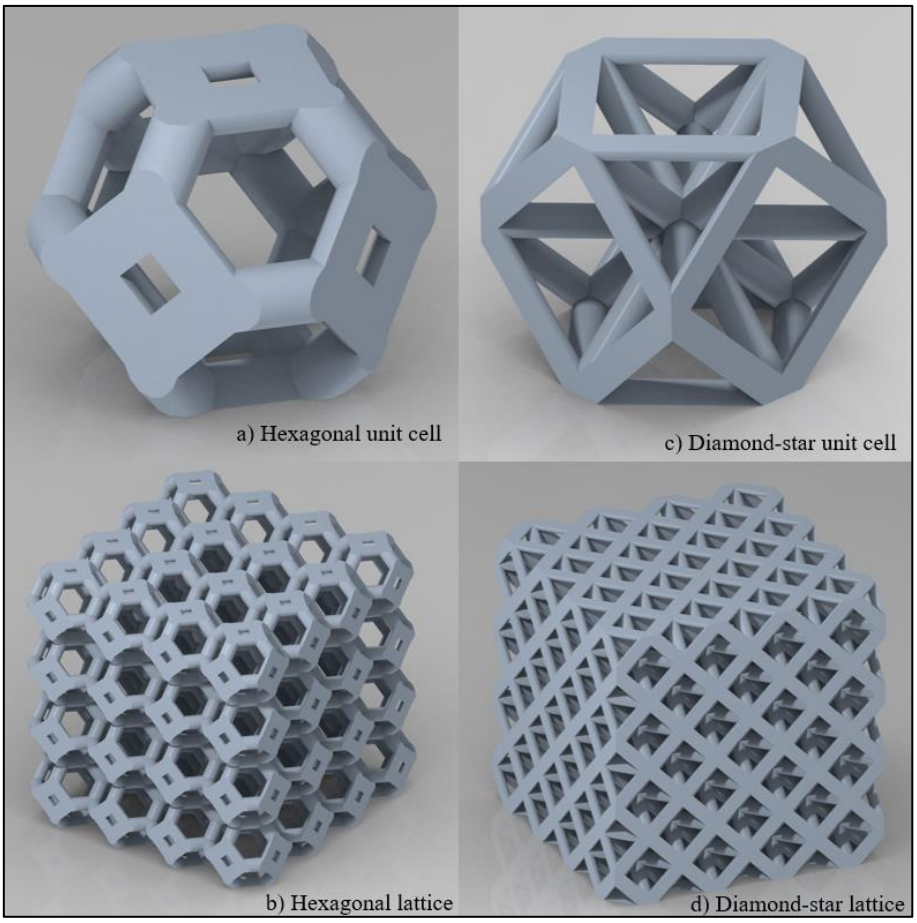

Figure 3-3: a) Hexagonal unit cell, b) Hexagonal lattice sample, c) Diamond-star unit cell, d) Diamond-star lattice sample

The minimum feature size for lattice generation was 0.1mm, to allow for the required strut thickness and porosity range, the cell size was increased to c = 1mm. The loading conditions

were varied slightly due to the upper surface no longer having the same total cross-sectional area as the complete unit cell. A 25N distributed force was used rather than the previous 4MPa distributed pressure. This new load represented the equivalent force placed on the $4mm^2$ cross sectional area under normal operating conditions of an 80kg person. The simulations were run using the same process as the square lattice and the results recorded.

3.4.5 Femoral Stem Modelling and Simulation

To determine the effectiveness of a porous femoral stem in reducing the occurrence of stress shielding, a femoral stem and example femur were modelled and analysed.

The femoral stem was modelled based on dimensioned drawings of the Kyocera A400 Standard Hip Stem (Kyocera 2024), sized for a recipient with an average cortical femur diameter of 25mm, and a neck angle (θ) of 51.4° from the horizontal plane. An example femoral head was added to the neck of the femoral stem to replicate realistic loading conditions. The stem and head were modelled as a single component and the dimensions of the head were visually estimated based on the x-ray imagery in Figure 2-1. The geometry and composition of the head is not relevant for the analysis.

The dimensions for the femur were modelled off the same x-ray imagery of a THA recipient (Hacking, Worsley & Nicoletti 2023). The femoral stem depicted in this image is not the same model that was used for the analysis, so it is dimensioned differently. The material for femoral bone was assumed to be solid and constant density. Real bone is porous and with varying density (Jones 2008) however this could not be represented in the model. The material properties of the bone were taken to be those of femoral cortical bone with a Poisson's ratio of 0.36 (Bazyar et al. 2023) and an elastic modulus of E = 19.6GPa (Hedayati & Fallah 2015). Figure 3-4 depicts the modelled stem, head and femur.

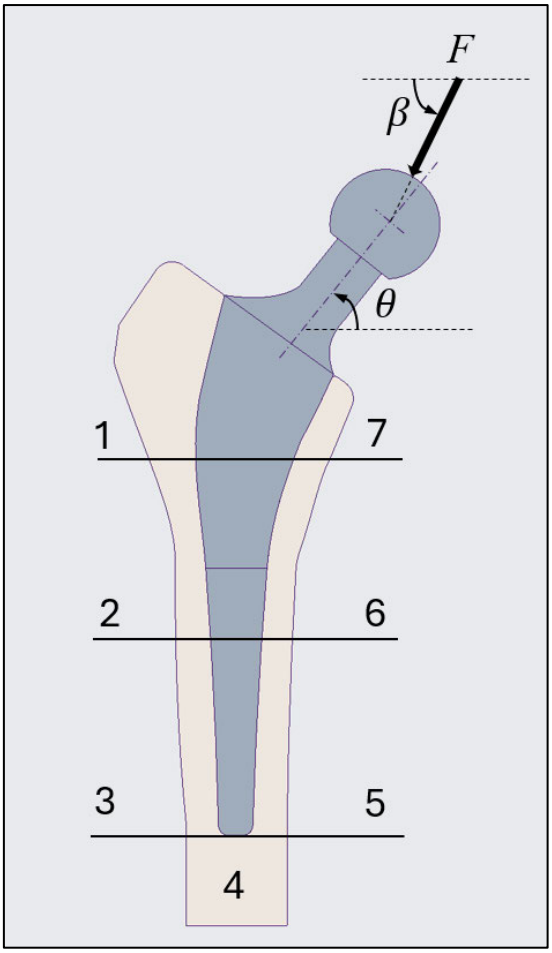

Figure 3-4: Cross sectional view of solid femoral stem and proximal femur by numbered Gruen zone

Multiaxial loading was applied to the head of the femoral stem, to simulate loading experienced in the body. The magnitude and direction of the resultant force was based on the findings of Eschweiler et al. (2012). The resultant three-dimensional force acting on the hip is a function of the applied force by the hip abductor muscles, bodyweight excluding the weightbearing leg, and lever arm length based on hip geometry. This force can be simplified to a two-dimensional representation by adjusting respective lever arm lengths. The mean resultant force (*F)* was determined to be 2.388kN acting at an angle (β) of 71.53° from the horizontal plane on the rotational centre of the femoral head. The existing body of medical and engineering literature examines the effect of THA on the femur using a series of predetermined zones, called Gruen zones (Tan & van Arkel 2021), depicted in Figure 3-4.

A three-dimensional (3D) solid femoral stem and femur were initially modelled. The material properties and loading conditions were set, and the FEA simulation was run, producing usable data, however difficulties were encountered when attempting to run the simulation for the porous stems. The simplified beam lattice could not transfer load to a separate part i.e. could not transfer stress from the stem to the femur. Additionally, the lattices contained too many elements to mesh.

To run the simulation, a solid, thin outer layer had to be added to the stem, the cell size was increased to c = 2mm and a 2.5-dimensional (2.5D) modelling approach was taken. A 4mm slice was taken through the frontal vertical plane of the stem and femur, as depicted in Figure 3-5. As the loading conditions were already simplified to a two-dimensional resultant force, the direction remained constant, however the magnitude of the force was adjusted by a factor of 0.1612 to account for the difference in average cross-sectional area between the 2.5D slice and the 3D stem.

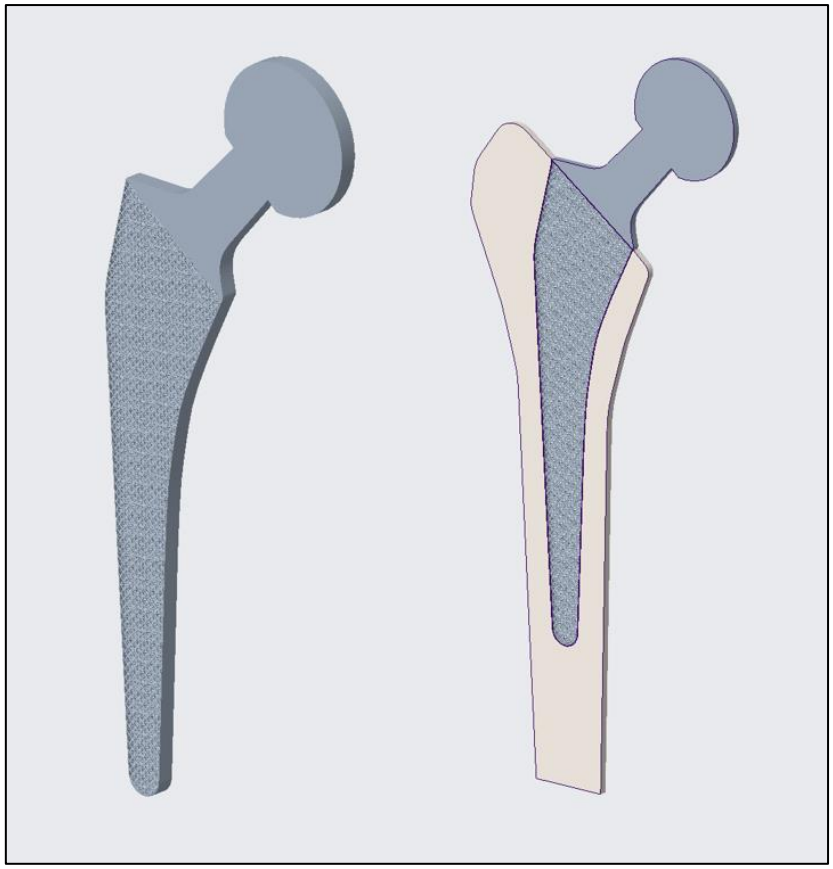

Figure 3-5: 2.5D model of porous femoral stem and proximal femur

The model was regenerated in the 2.5D slice format. The simulation was run for a solid stem and a porous stem of each lattice type at a porosity of $\varphi = 0.8$. To simulate an intact femur, the material for the solid stem was set to be that of bone and the simulation was run. For each simulation, the minimum and maximum VM stress in each Gruen zone of the proximal femur was recorded, as well as the VM stress distribution within the femoral stem.

The percentage of stress shielding (*SS*) experienced in each Gruen zone was calculated by comparing the relative change in average stress between the implanted proximal femur and intact femur in the corresponding Gruen zone, as shown in Equation 3-15 (Limmahakhun et al. 2017).

$$SS = 100\frac{\sigma_{intact} - \sigma_{implanted}}{\sigma_{intact}}$$ *Equation 3-15*

Where σ_{intact} is the mean VM stress in the intact femur and $\sigma_{implanted}$ is the mean VM stress in the implanted femur.

The fatigue strength of the lattice structure was calculated using Soderberg failure criteria (Mehboob et al. 2020). To do so, the alternating stress (σ_a) was calculated as per Equation 3-16.

$$\sigma_a = \frac{\sigma_{stem\ max} - \sigma_{stem\ min}}{2}$$ *Equation 3-16*

Where $\sigma_{stem\ max}$ and $\sigma_{stem\ min}$ are the maximum VM stress within the femoral stem.

The Soderberg line is plotted in intercept form as per Equation 3-17.

$$\frac{\sigma_a}{S_e} + \frac{\sigma_m}{S_{ys}} = \frac{1}{N}$$ *Equation 3-17*

Where σ_m in the mean VM stress within the femoral stem, S_e is the endurance limit of the material obtained from property tables, S_{ys} is the yield strength of the material at 1070MPa (MatWeb 2024), and *N* is the desired safety factor.

If the plotted points for σ_m and σ_a lay below the Soderberg line, the material was predicted to not fail due to fatigue. Finally, the maximum stress of the femoral stem was checked to be under the yield strength of the material.

Chapter 4 Results

The following chapter details the results obtained from all FEA and analytical calculations. The data from all simulations was recorded from Creo Simulate into an Excel spreadsheet for analysis. The complete spreadsheet, containing all data and calculations can be found in Appendix A.

4.1 Square Unit Cell

The FEA results for the single square unit cell are shown in Table 4-1, given $c = 0.5$ and an applied compressive load of 4kPa. The results show that as the porosity of the model increases, the relative reduction in elastic modulus increases for both the analytical and measured results. Variation between the analytical results and measured results was observed, particularly for stress measurements. The relative change in elastic modulus for the unit cell relative to other square lattice samples is plotted in Figure 4-10.

Table 4-1: Square unit cell results of FEA

		Sample 1	Sample 2	Sample 3	Sample 4	Sample 5
Geometric Properties	Strut thickness t (mm)	0.167	0.138	0.111	0.084	0.054
	Pore size c (mm)	0.333	0.362	0.389	0.416	0.446
	Porosity φ	0.500	0.600	0.700	0.800	0.900
Average Stress	von Mises σ_{VM} (MPa)	17.08	23.49	33.24	55.34	112.01
	Measured normal σ_{YY} (MPa)	6.55	11.17	22.70	52.30	121.00
	Analytical normal σ_c (MPa)	6.00	6.79	7.93	9.84	14.12
Average Strain	Measured ε_m (10^{-4})	0.163	0.243	0.393	0.715	1.590
	Displacement-calculated ε_c (10^{-4})	0.102	0.138	0.205	0.365	1.160
Elastic Modulus	Measured E_m (GPa)	104.85	96.49	84.61	77.38	70.49
	Calculated E_C (GPa)	59.06	49.22	38.73	26.92	12.17
Change in Elasticity	Measured K_m (%)	-8.02	-15.36	-25.78	-32.12	-38.16
	Calculated K_c (%)	-48.19	-56.83	-66.03	-76.38	-89.32

The relative error rates between the alternate methods for measuring stress and strain are tabulated in Table 4-2. The relative error between VM stress and normal stress to analytical stress is very high, indicating the model is not producing valid results. The relative error between measured and displacement-calculated strain is also high, but not to the same magnitude as the stress.

Table 4-2: Square unit cell measured to analytical error rates

Porosity φ	0.4999	0.6001	0.6997	0.8000	0.8996
σ_{VM} to σ_c relative error (%)	184.65	246.23	319.40	462.45	693.19
σ_{YY} to σ_c relative error (%)	9.18	64.63	186.59	431.85	759.30
ε_m to ε_c relative error (%)	60.3	76.6	92.1	95.8	37.4

A comparison of the results for the different methods of measuring stress are plotted in Figure 4-1. The VM stress and normal stress return similar values. At $\varphi = 0.5$, the measured and analytical normal stress are within 9.18%, however as the porosity increases, the VM and measured normal stress diverge exponentially from the analytically calculated normal stress.

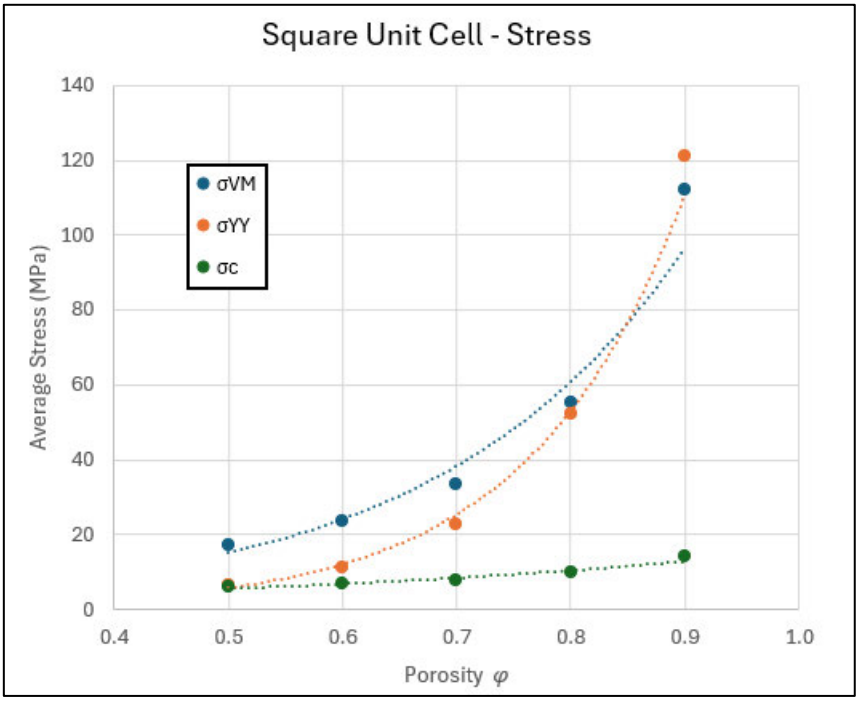

Figure 4-1: Comparison of VM stress, measured normal stress and analytically calculated normal stress for square unit cell

The VM stress and YY axis strain distributions for the square unit cell are shown in Figure 4-2. The stress and strain distribution for the models are similar and the absolute maximum and minimum values occur at the same points. This same trend was observed for all subsequent models.

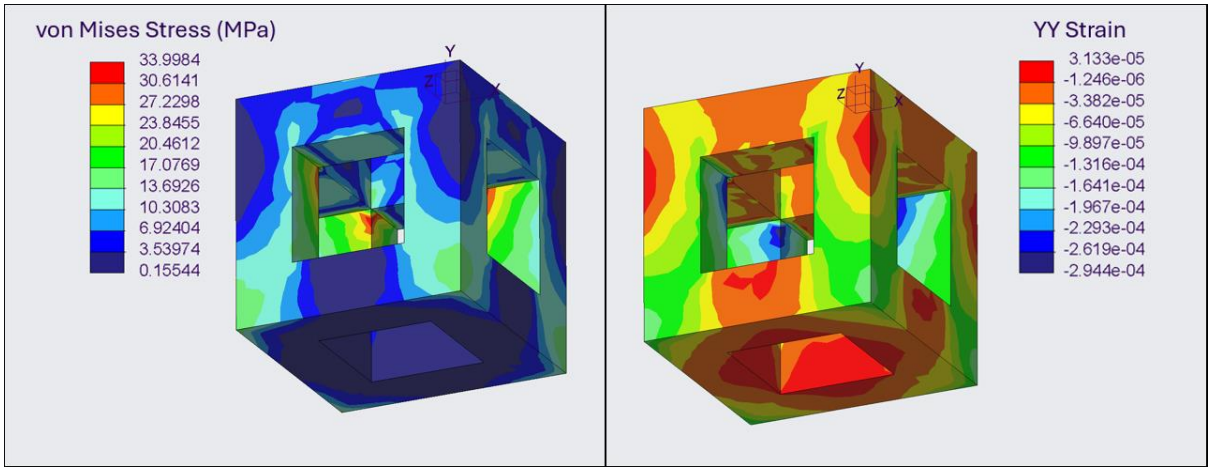

Figure 4-2: Left: VM Stress distribution for square unit cell, right: Maximum YY strain distribution for square unit cell

The displacement and deformation of the square unit cell are shown in Figure 4-3. Due to the loading being represented as an evenly distributed pressure on the top surface, bending of the top horizontal struts occurred. This is a contributing factor to the stress concentrations on the surface layer observed in Figure 4-2.

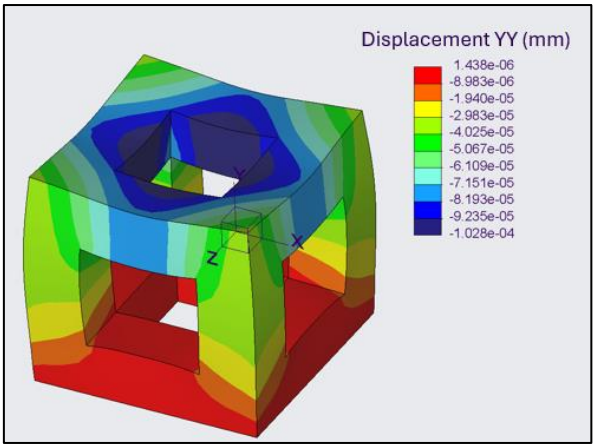

Figure 4-3: Vertical displacement for square unit cell

4.2 $n = 4$ Square Lattice

The model was expanded to an $n = 4$ lattice and the simulation repeated. The results are tabulated in Table 4-3. As with the unit cell, the relative reduction in elastic modulus increases as the porosity increased.

Table 4-3: n=4 Square lattice results

		Sample 1	Sample 2	Sample 3	Sample 4	Sample 5
Geometric Properties	Strut thickness t (mm)	0.167	0.138	0.111	0.084	0.054
	Pore size c (mm)	0.333	0.362	0.389	0.416	0.446
	Porosity φ	0.670	0.754	0.829	0.895	0.952
Average Stress	von Mises σ_{VM} (MPa)	18.209	24.386	32.621	51.400	102.528
	Measured normal σ_{YY} (MPa)	5.72	9.56	21.20	46.53	121.80
	Analytical normal σ_c (MPa)	7.53	8.82	10.68	13.77	20.66
Average Strain	Measured ε_m (10^{-4})	1.85	2.59	3.82	6.53	14.72
	Displacement-calculated ε_c (10^{-4})	1.19	1.50	1.94	2.22	5.032
Elastic Modulus	Measured E_m (GPa)	98.36	94.08	85.40	78.65	69.65
	Calculated E_C (GPa)	62.87	58.82	54.80	61.88	41.06
Change in Elasticity	Measured K_m (%)	-13.72	-17.48	-25.08	-31.01	-38.90
	Calculated K_c (%)	-44.85	-48.41	-51.93	-45.72	-63.98

There was still considerable error between the VM, measured normal stress and the analytically calculated normal stress. A high rate of error between the measured and displacement-calculated strain was also observed as seen in Table 4-4, indicating the model is not producing valid results.

Table 4-4: n=4 Square lattice results measured to analytical error rates

Porosity φ	0.6699	0.7545	0.8290	0.8950	0.9522
σ_{VM} to σ_c relative error (%)	141.8	176.4	205.4	273.1	396.2
σ_{YY} to σ_c relative error (%)	24.0	8.4	98.5	237.8	489.4
ε_m to ε_c relative error (%)	54.6	72.8	95.9	193.5	192.5

When plotting the different methods of measuring stress for the $n = 4$ square lattice, the same trend is observed for that of the unit cell. As shown in Figure 4-4, the VM and measured normal stress diverge from the analytically calculated normal stress as porosity increases.

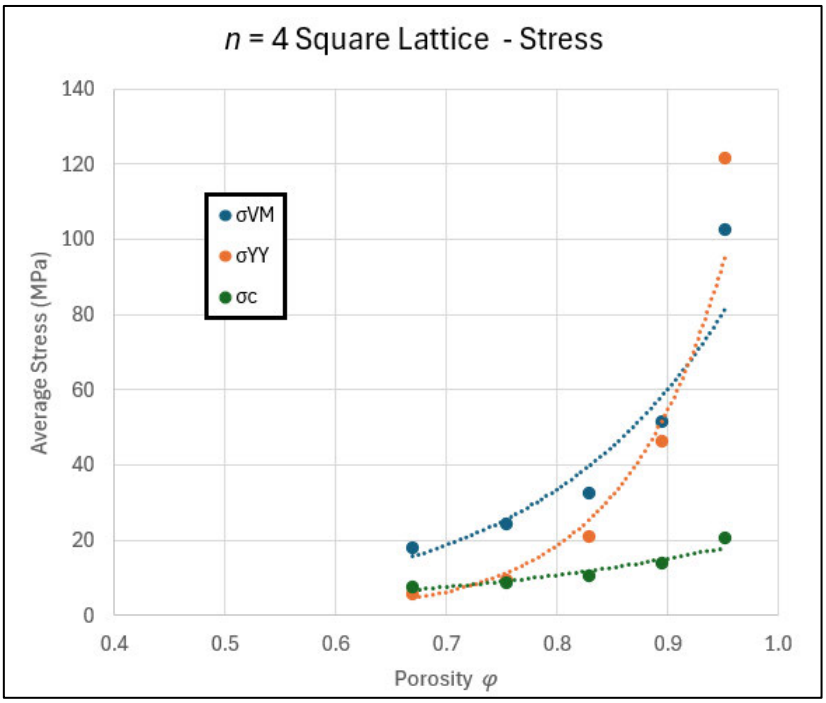

Figure 4-4: Comparison of VM stress, measured and analytically calculated normal stress for n=4 square lattice

The stress distribution for the $n = 4$ square lattice is shown in Figure 4-5. As with the unit cell, the point of maximum stress occurred on the surface layer at the internal corner nodes, furthest from the centroid of the upper surface. The minimum and maximum values for stress were used to calculate the median value, so it was noted that isolated stress concentrations skewed the results considerably. The stress distribution for the lattice followed the same trend. To alleviate the source of error, the results were adjusted to exclude the surface layer in subsequent tests.

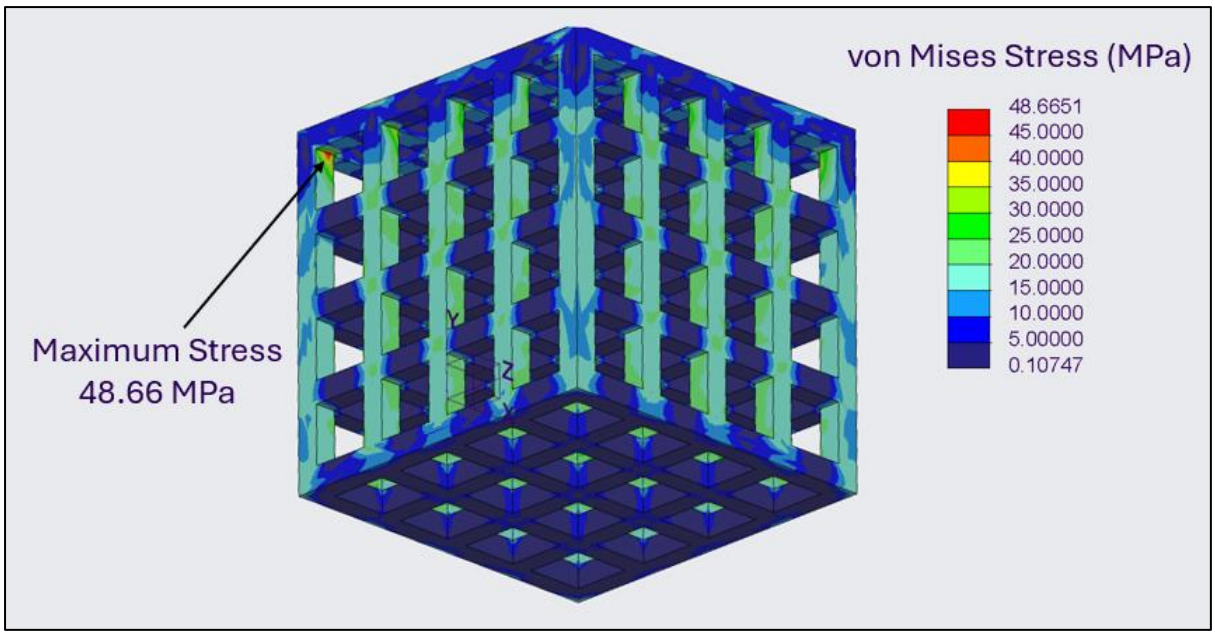

Figure 4-5: VM stress distribution of n=4 square lattice at $\varphi = 0.67$

4.3 $n = 8$ Square Lattice

The model was regenerated as an $n = 8$ square lattice, and the simulation was run again under the same loading conditions. In this iteration, the surface cell layer stress concentrations were excluded from the results, shown in Figure 4-6. The maximum stress and strain on the bulk structure were roughly half that observed in the surface layer. This provides much more accurate representation of average stress and strain throughout the entire structure. The results are presented in Table 4-5.

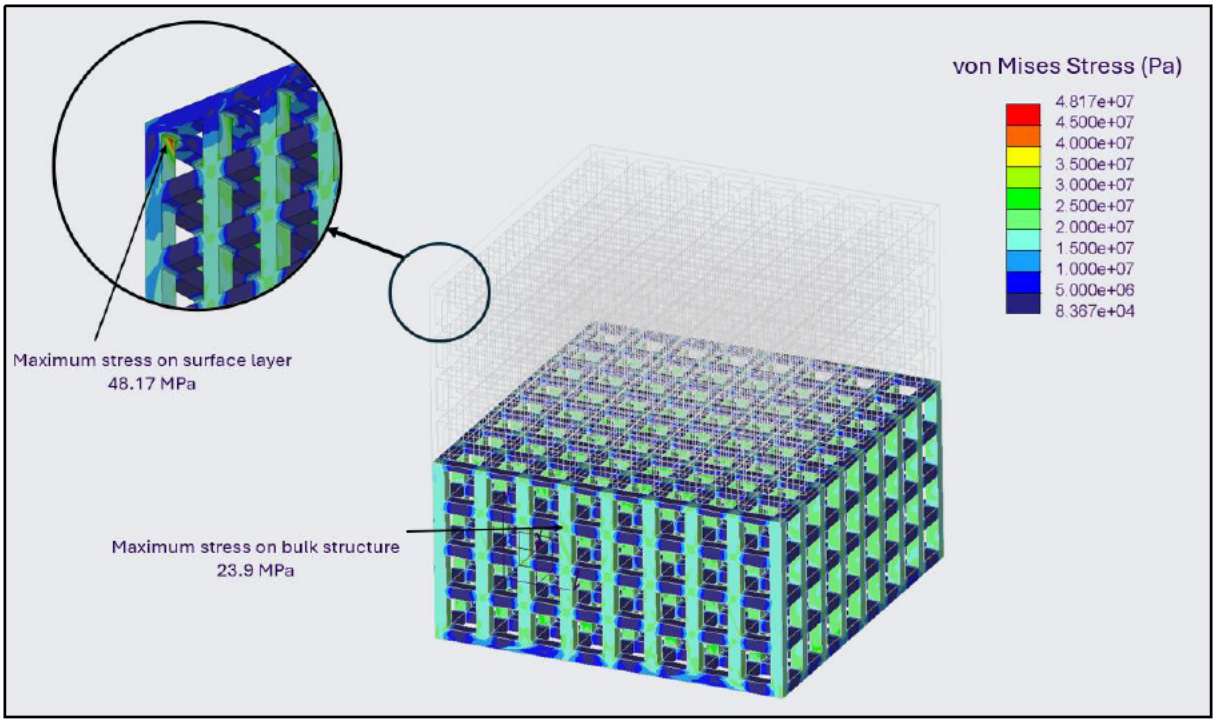

Figure 4-6: VM stress distribution of n=8 square lattice including surface layer effects at $\varphi = 0.32$

Table 4-5: n=8 Square lattice results

		Sample 1	Sample 2	Sample 3	Sample 4	Sample 5
Geometric Properties	Strut thickness t (mm)	0.25	0.22	0.18	0.14	0.10
	Pore size c (mm)	0.25	0.28	0.32	0.36	0.40
	Porosity φ	0.456	0.546	0.666	0.779	0.877
Average Stress	von Mises σ_{VM} (MPa)	10.45	10.41	13.5	13.24	14.39
	Measured normal σ_{YY} (MPa)	5.61	5.93	6.81	8.89	12.4
	Analytical normal σ_c (MPa)	5.72	6.33	7.48	8.74	12.67
Average Strain	Measured ε_m (10^{-4})	0.933	0.934	1.200	1.550	2.420
	Displacement-calculated ε_c (10^{-4})	0.763	0.909	1.180	1.750	2.420
Elastic Modulus	Measured E_m (GPa)	111.95	111.43	112.67	85.71	59.4
	Calculated E_C (GPa)	75.03	69.63	63.29	49.92	52.33
Change in Elasticity	Measured K_m (%)	-1.8	-2.26	-1.17	-24.82	-47.89
	Calculated K_c (%)	-34.18	-38.92	-44.48	-56.21	-54.09

The effect of removing the surface layer measurements can be clearly observed by the reduction in error rate shown in Table 4-6. The relative error for both stress and strain is reduced compared to the previous samples. Of note is the reduction in error rate between analytically calculated and measured normal stress, to between 2.12% and 8.96%.

Table 4-6: n=8 Square lattice measured to analytical error rates

Porosity φ	0.456	0.546	0.666	0.779	0.877
σ_{VM} to σ_c relative error (%)	82.60	64.47	80.44	51.51	13.56
σ_{YY} to σ_c relative error (%)	1.94	6.38	8.96	1.73	2.12
ε_m to ε_c relative error (%)	22.36	2.76	1.33	11.76	0.052

Figure 4-7 shows a comparison of the alternate methods for measuring stress in the $n = 8$ square lattices once the surface layer measurements have been excluded. The measured and analytically calculated normal stress are comparable in magnitude and follow the same linear trend as porosity is increased. The VM stress follows a similar linear relationship with porosity, however, is a higher magnitude than the normal stresses. The consistency between the measured and analytical normal stress indicate that the $n = 8$ lattice produced valid results.

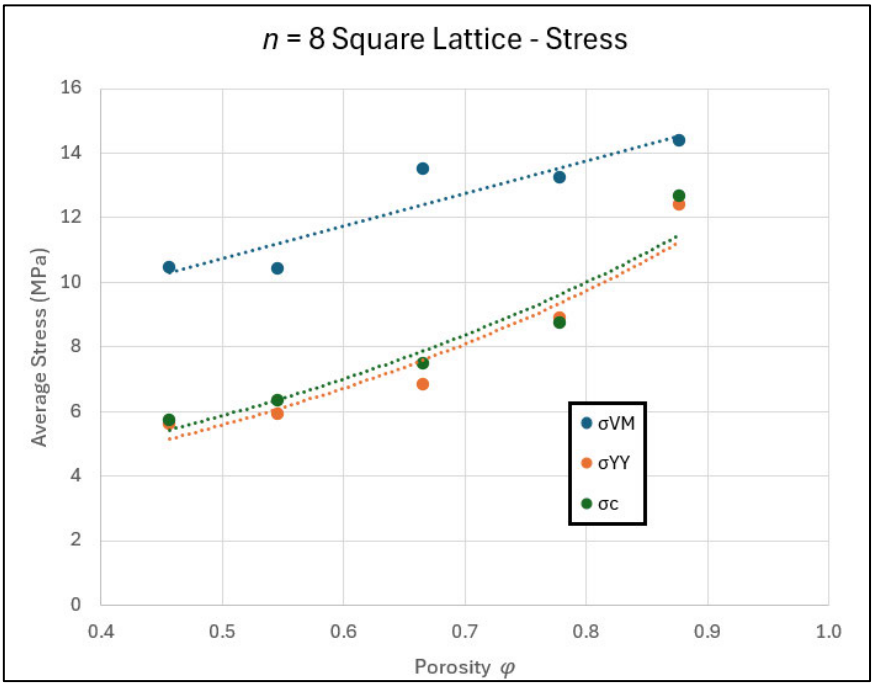

Figure 4-7: Comparison of VM stress, and measured and analytical normal stress for n=8 square lattice

The comparison between the relative error for the $n = 4$ lattice and $n = 8$ lattice can be observed more clearly in Figure 4-8 and. The figures illustrate how removal of surface layer measurements, drastically reduced the error rate between measured and analytical results in both stress and strain. Although Figure 4-8 still presents a high absolute error rate between measured VM stress and analytically calculated normal stress, the error can be attributed to the difference in methods of calculating stress. Importantly, the error no longer exponentially increases as porosity increases. All subsequent lattice sample analysis was conducted excluding surface layer measurement data.

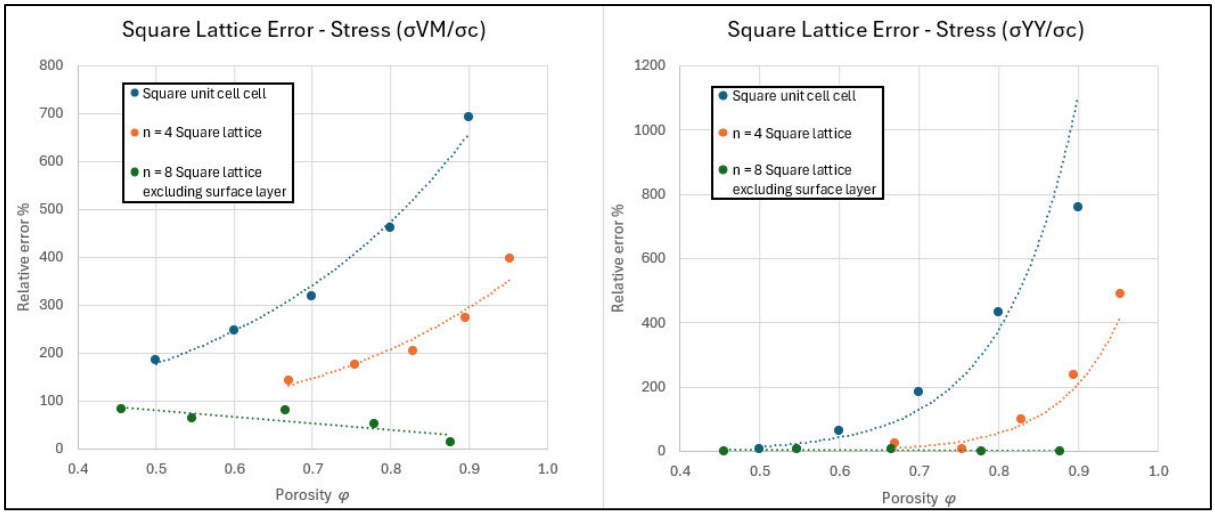

Figure 4-8: Comparison of Relative error % for each square lattice type. Left: σ_{VM} to σ_c error, Right: σ_{YY} to σ_c

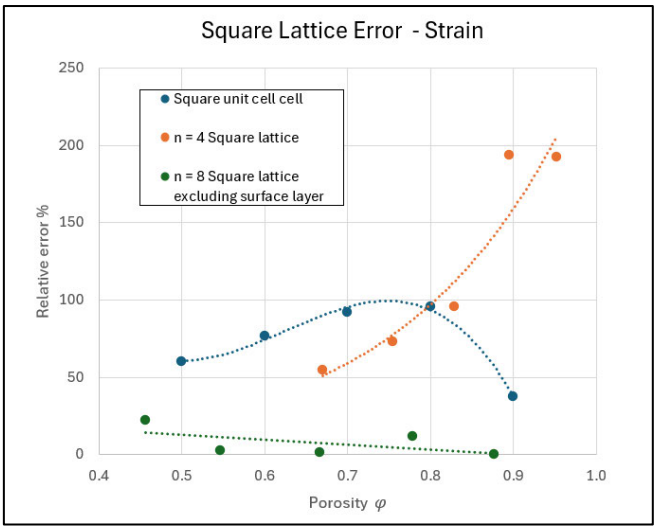

Figure 4-9: Comparison of Relative error % (ε_m to ε_c) for each square lattice type

The relative change in elastic modulus as a function of porosity for each square lattice is plotted in Figure 4-10. Although the results initially seem to suggest that the number of cells has an impact on the rate of change of K, it is important to note that the unit cell and n = *4* tests were carried out without excluding surface layer stress concentrations and were not producing valid results. Therefore, comparison between these datasets cannot be directly made. Regardless, there is a clear trend in all the data that as porosity increases, the equivalent elasticity of the structure increases.

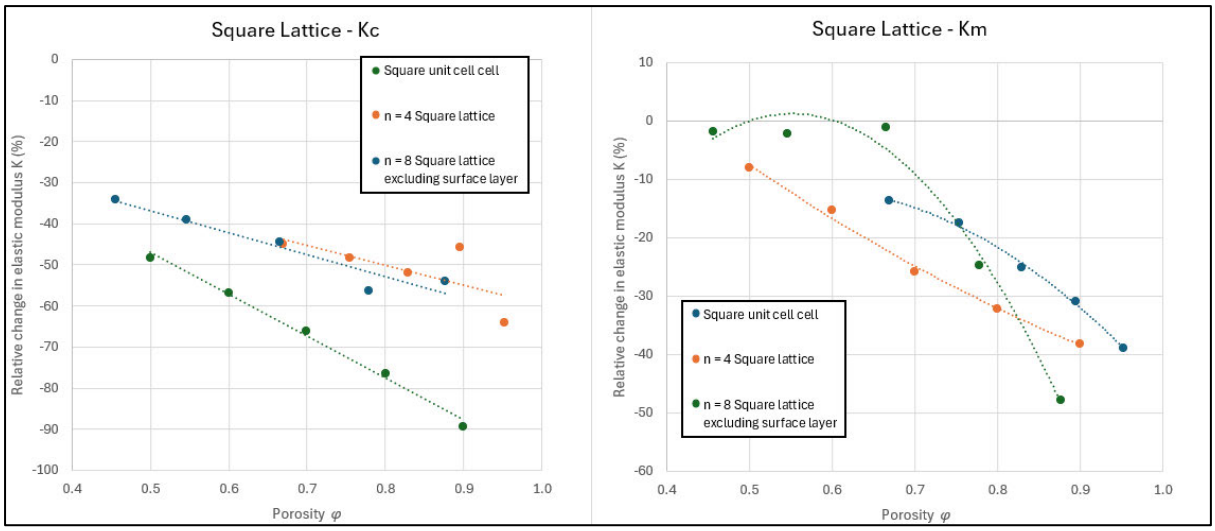

Figure 4-10: Comparison of K for each square lattice type. Left: Calculated relative change (Kc), Right: measured relative change (Km)

4.4 Porosity as a Function of Number of Cells

The effect that the number of cells has on the accuracy of lattice FEA results was analysed to confirm the reduction in error observed in the $n = 8$ square lattice was not due to the increased number of cells. Figure 4-11 shows a plot for porosity as a function strut thickness (t), number of cells (n) and cell size (c), as described in Equation 3-14, for a selected range of strut thicknesses at $c = 0.5$mm. The porosity of the structure converges on a value logarithmically as the number of cells increases, and this convergence occurs quicker at lower strut thickness. At $n = 4$, and $t = 0.2$mm the porosity within 10% of its value at $n = 1000$. At $n = 4$, and $t = 0.05$mm, the porosity within 3% of its value at $n = 1000$. These results show that conducting further analysis on single unit cells would not provide accurate data, and an $n \geq 4$ lattice sample would provide a close approximation of the full lattice behaviours.

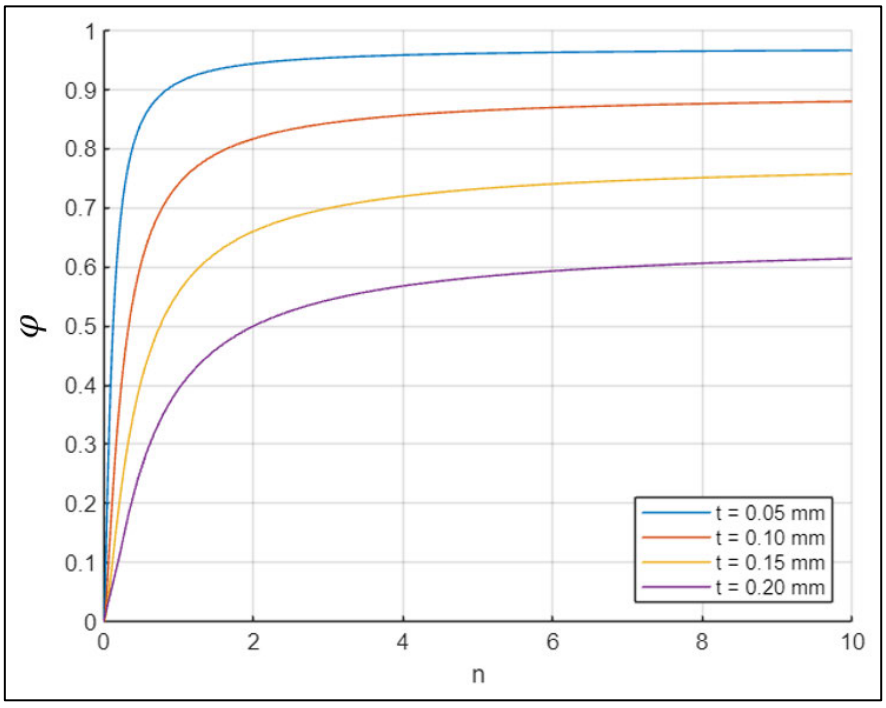

Figure 4-11: Porosity of square lattice as a function of the number of cells cubed at various strut thicknesses, at c=0.5mm

4.5 Hexagonal and Diamond-star Lattice

The hexagonal lattice was analysed at c = 1mm, n = 4 and F = 25N with the results shown in Table 4-7. The maximum viable strut thickness was limited by the geometry of the lattice. At $\varphi < 0.6$, the structure was no longer fully porous and contained internal sealed voids. For this reason, the minimum porosity of the hexagonal lattice was $\varphi = 0.6$. As porosity increases, the relative reduction in elastic modulus increases moderately for K_m and substantially for K_c. This relationship is illustrated more clearly in Figure 4-15, where the K_m and K_c for every lattice is compared.

Table 4-7: Hexagonal lattice results

		Sample 1	Sample 2	Sample 3	Sample 4	Sample 5
Geometric Properties	Strut thickness t (mm)	0.30	0.20	0.16	0.12	0.10
	Pore size c (mm)	0.70	0.80	0.84	0.88	0.90
	Porosity φ	0.605	0.794	0.86	0.917	0.941
Average Stress	von Mises σ_{VM} (MPa)	20.92	68.08	175.97	422.11	646.12
	Analytical stress σ_c (MPa)	3.95	7.58	11.18	18.85	26.46
Average Strain	Analytical normal σ_c (MPa)	1.930	6.730	18.500	49.600	81.900
	Measured ε_m (10^{-4})	0.813	3.190	7.570	23.400	51.600
Equivalent Elasticity	Displacement-calculated ε_c (10^{-4})	108.31	101.21	95.12	85.1	78.94
	Measured E_m (GPa)	48.65	23.73	14.76	8.06	5.13
Change in Elasticity	Calculated E_C (GPa)	-4.99	-11.22	-16.56	-25.35	-30.76
	Measured K_m (%)	-57.33	-79.18	-87.05	-92.93	-95.5

The stress distribution in the hexagonal lattice was similar to that observed in the square lattice and is shown in Figure 4-12. The surface layer had a larger stress concentration than the bulk of the body. The differential between the maximum stress on the surface layer compared to the rest of the body is less pronounced in comparison to the square lattice. In the hexagonal lattice, the stress concentrations occur at all cell joints at a similar value. It was also noted that the maximum stress of hexagonal lattice is relatively high compared to the other lattice samples.

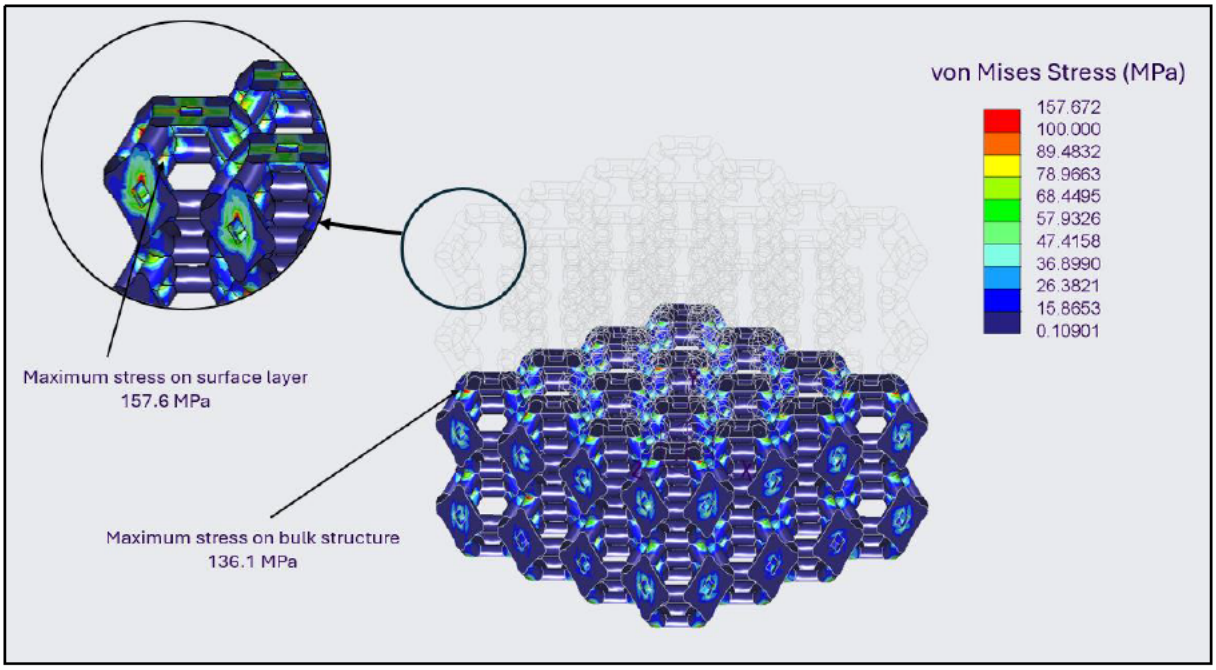

Figure 4-12: Hexagonal lattice VM stress distribution excluding surface layer effects at $\varphi = 0.79$

The model was then regenerated to a diamond-star lattice and the simulation run under the same conditions, with c = 1mm, n = 4 and F = 25N. The results are shown in Table 4-8. A moderate reduction in relative elastic modulus was observed as porosity increased in K_m, along with a substantial reduction in K_c.

Table 4-8: Diamond-star lattice results

		Sample 1	Sample 2	Sample 3	Sample 4	Sample 5
Geometric Properties	Strut thickness t (mm)	0.25	0.2	0.15	0.12	0.10
	Pore size c (mm)	0.646	0.717	0.788	0.83	0.859
	Porosity φ	0.469	0.621	0.765	0.841	0.886
Average Stress	von Mises σ_{VM} (MPa)	10.04	17.23	24.79	44.79	62.51
	Analytical stress σ_c (MPa)	2.94	4.13	6.66	9.85	13.71
Average Strain	Analytical normal σ_c (MPa)	0.971	1.620	2.480	4.810	7.140
	Measured ε_m (10^{-4})	0.616	1.170	2.640	4.280	9.370
Equivalent Elasticity	Displacement-calculated ε_c (10^{-4})	103.49	106.14	100.06	93.16	87.56
	Measured E_m (GPa)	47.77	35.14	25.2	23.05	14.63
Change in Elasticity	Calculated E_c (GPa)	-9.22	-6.9	-12.22	-18.28	-23.19
	Measured K_m (%)	-58.1	-69.18	-77.9	-79.78	-87.17

The VM stress distribution is shown in Figure 4-13. The surface layer maximum stress is roughly double the maximum stress of the bulk structure. Areas of stress concentration at strut intersections remain, however, the maximum stress is relatively low.

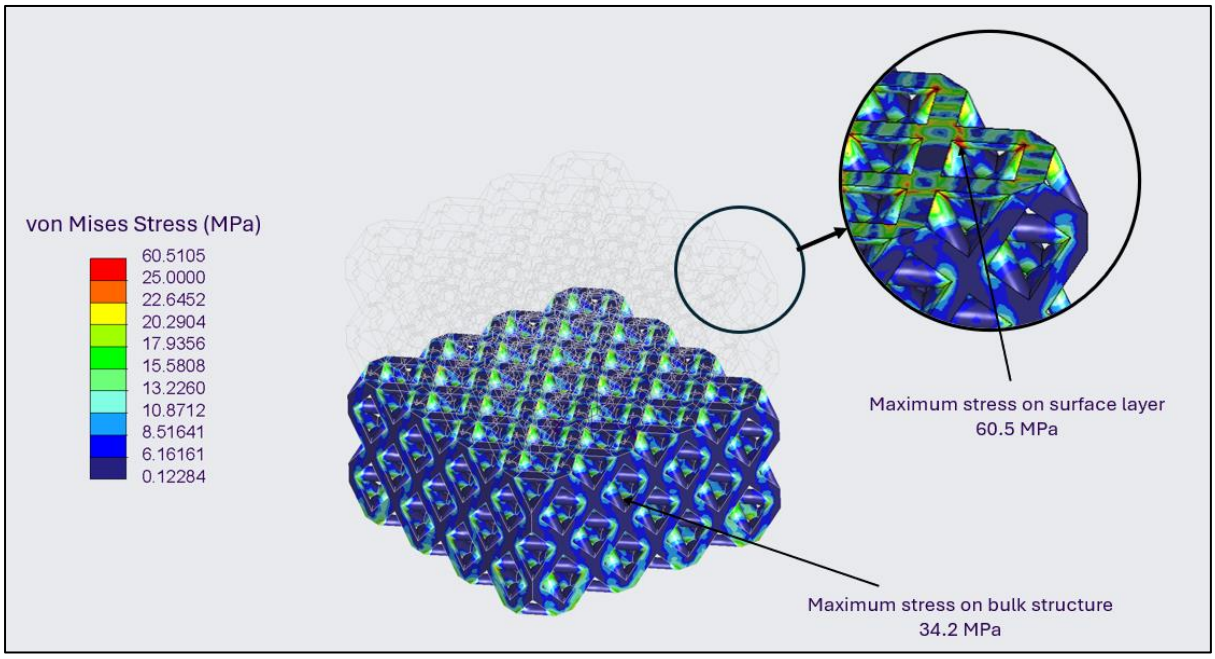

Figure 4-13: Diamond-star lattice VM stress distribution excluding surface layer effects at $\varphi = 0.62$

Figure 4-14 shows a comparison of the square, hexagonal and diamond star lattice's measured relative change in elastic modulus (K_m) as a function of porosity. The data was analysed in the MATLAB curve fitting toolbox, and a two-term exponential line of best fit for K_m was identified. The same trend was observed in all K_m datasets. As porosity increases, the equivalent modulus of elasticity decreases exponentially. Additionally, it appears that for the square lattice, below a minimum porosity no reduction in elastic modulus will occur.

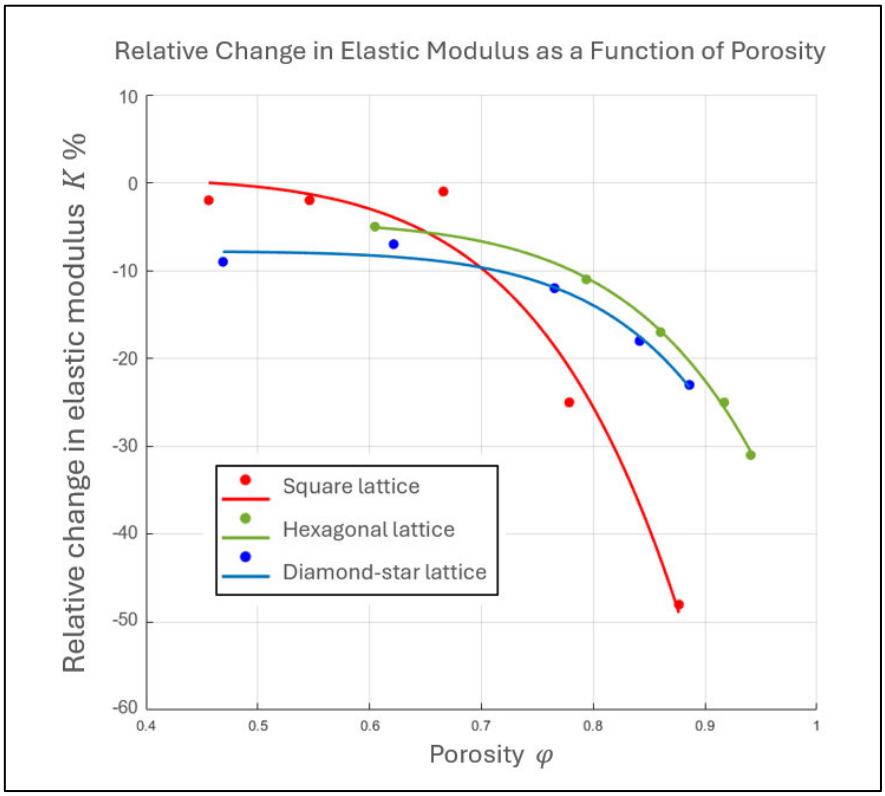

Figure 4-14: Comparison of K_m for all tested lattice types

Figure 4-15 shows the comparison of each lattice type's calculated relative change in elastic modulus (K_c). In contrast to Figure 4-14, The results for K_c show a linear relationship between porosity and reduction in elastic modulus. Additionally, K_c indicates that the diamond-star and hexagonal lattice achieve a far greater reduction in elastic modulus than the square lattice.

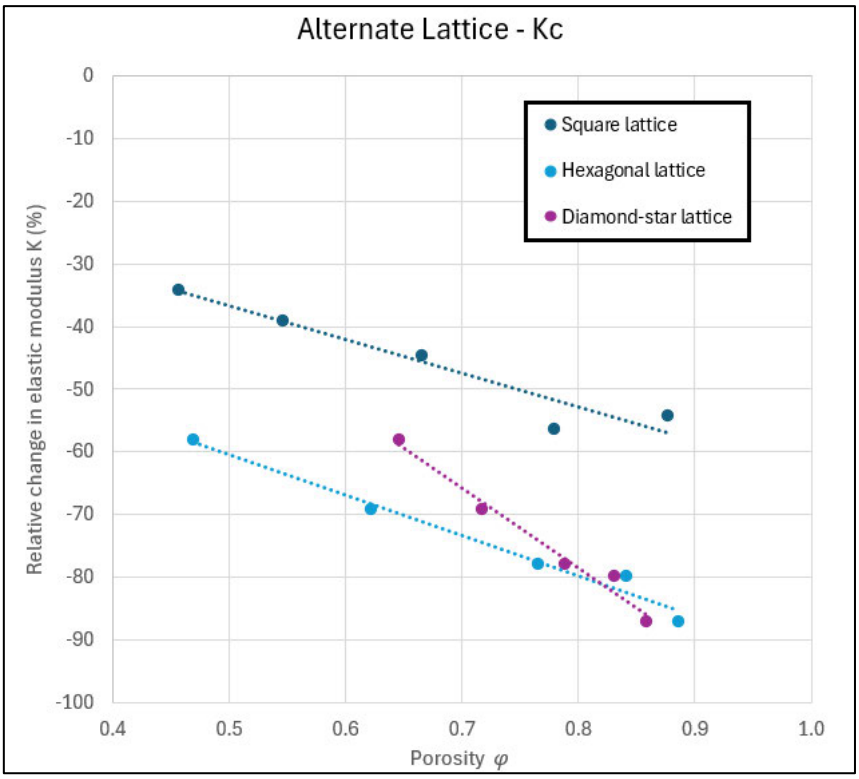

Figure 4-15: Comparison of K_c for all tested lattice types

4.6 Femoral Stem – FEA Results and Observations

This section covers the results for all femoral stem tests. The combined stress distributions for each femoral stem and corresponding femur are presented by lattice type with general observations noted in Chapter 4.6. Following this, the stress distribution of all femurs compared by Gruen zone and subsequent values for stress shielding are presented in Chapter 4.7. Finally, the stress distribution of all femoral stems are presented along with findings for fatigue and yield strength in Chapter 4.8.

The solid femoral stem and femur were modelled and analysed as a 2.5D representation of the 3D structure with an applied load of F = 384.9kN acting at an angle of β = 71.53°. The stress distribution of the central plane is shown in Figure 4-16. The stress within the stem is higher than in the proximal femur, however, the difference between the two is relatively low. The area of maximum stress occurs within the femoral neck; however, this is not relevant for the purpose of measuring stress shielding.

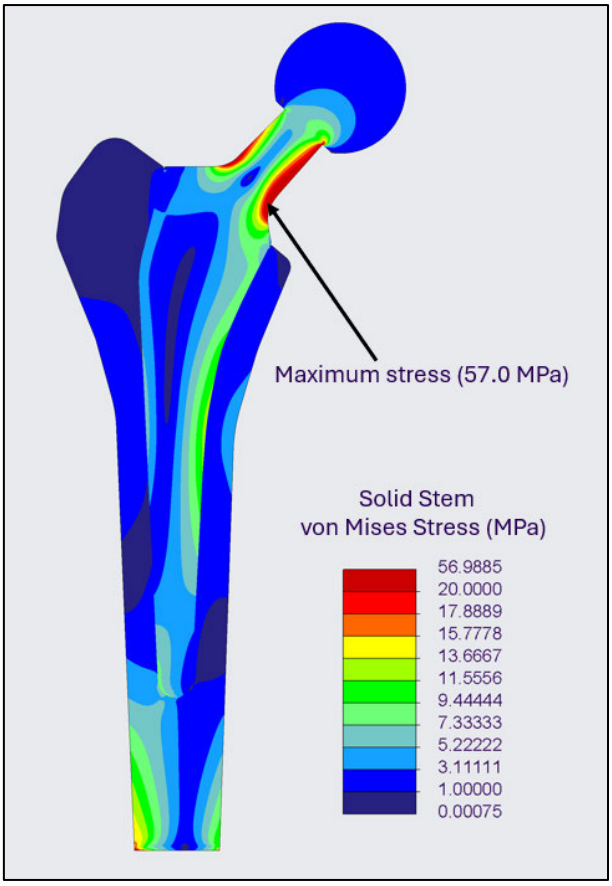

Figure 4-16: Solid stem and proximal femur stress distribution

The intact femur was simulated by changing the material of the solid femoral stem to bone. The stress distribution of the central plane of the intact femur is shown in Figure 4-17. The stress concentration on the bottom surface is a result of the simulation fixed displacement condition and was excluded from the analysis. The stress distribution throughout the remainder of the intact femur shows no stress concentrations and a smooth gradient.

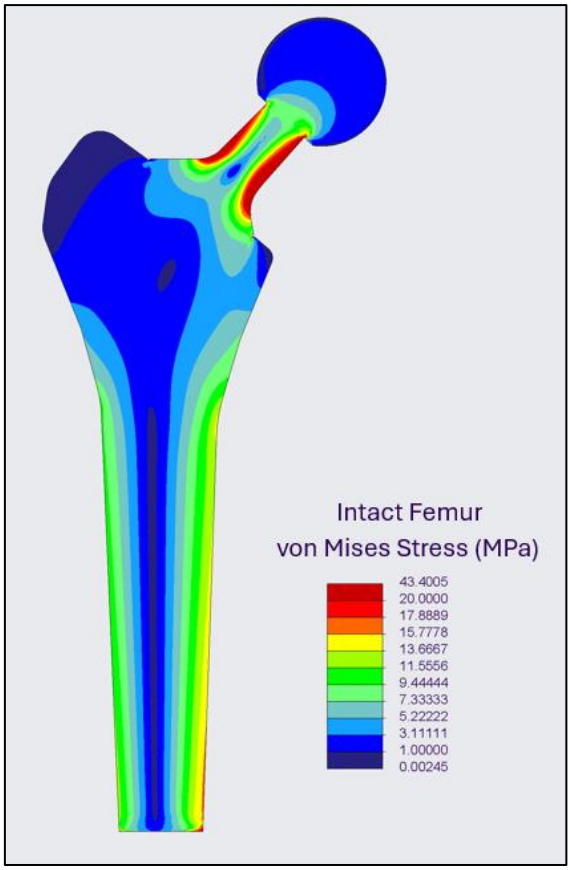

Figure 4-17: Intact femur stress distribution

The 2.5D model of the femoral stem was regenerated as a square cell lattice of Ti_6Al_4V, at a cell size of c = 2mm, and porosity of $\varphi = 0.8$, and the simulation run under the previous loading conditions. The stress distribution on the central plane of the porous stem and femur are shown in Figure 4-18. The maximum stress within the femoral stem now occurs at the corner of the intersection between the solid neck, and the porous lattice section. A substantial stress concentration is present at this corner, with a maximum value of 681MPa. The maximum stress outside this single point is approximately 154MPa at the node intersections in the same general vicinity. Additionally, the point of maximum stress occurs on the thin, solid outer wall of the porous section. As explained in Chapter 3.4.5, this solid outer wall was an idealisation needed to make the simulation run, and the behaviour indicated at the point of stress concentration will not reflect what would be observed in a true porous lattice. Figure

4-18 also shows the presence of irregularly formed surface layer cells. This is an artifact of the automatic lattice feature in Creo Parametric. These irregular surface layer cells appear to have little impact on the stress distribution of the square lattice type in contrast to the subsequent lattice tests. The average stress within the femoral stem is considerably higher than that of the surrounding femur. The same is true for the strain distribution, indicating a greater amount of deformation is occurring in the femoral stem, and therefore more stress is being placed on the femur.

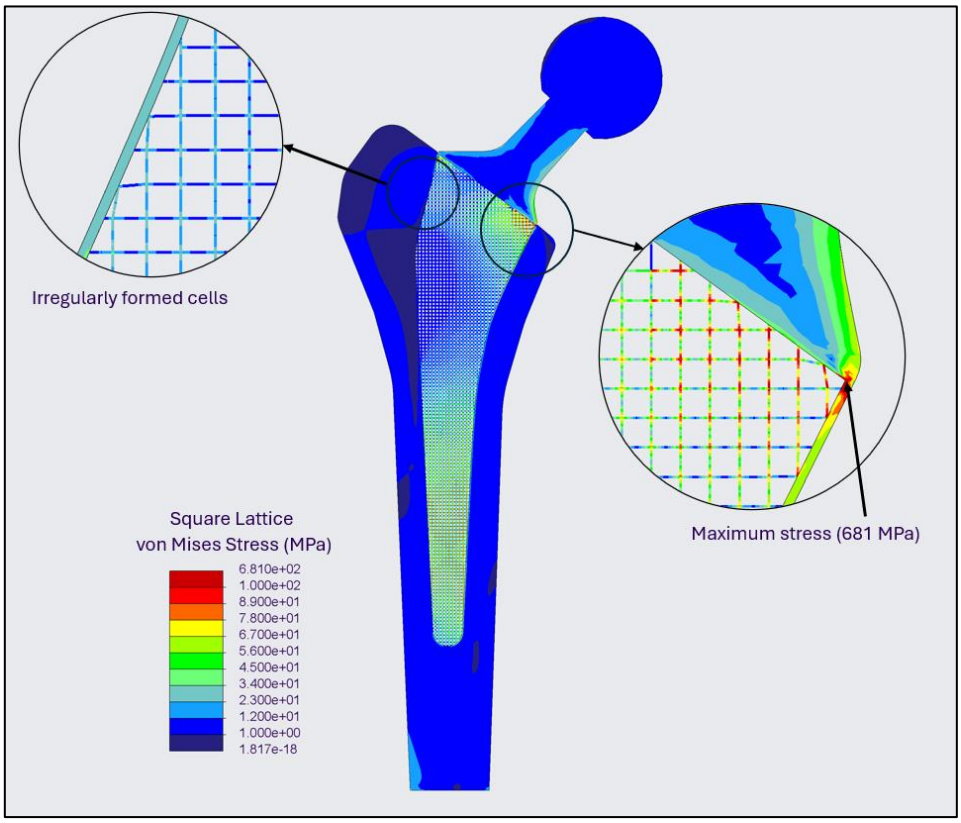

Figure 4-18: Square lattice porous stem and proximal femur stress distribution

The stress distribution of the hexagonal lattice femoral stem and its corresponding femur are presented in Figure 4-19. Similar to the square lattice, a main stress concentration occurs at the intersection region between the solid neck, porous lattice section and the solid outer wall. In this case, the point of maximum stress does not occur on the solid wall, but within the beam member of a partially formed surface lattice cell. The highest stress beam member is at 809MPa. Excluding the directly adjacent members, the next highest stress beam is at 132MPa. The partially formed surface cells appear to cause anomalous stress concentrations throughout the outer layer of the lattice. As with the square lattice the stress within the femoral stem is substantially higher than that of the surrounding femur indicating deformation is occurring.

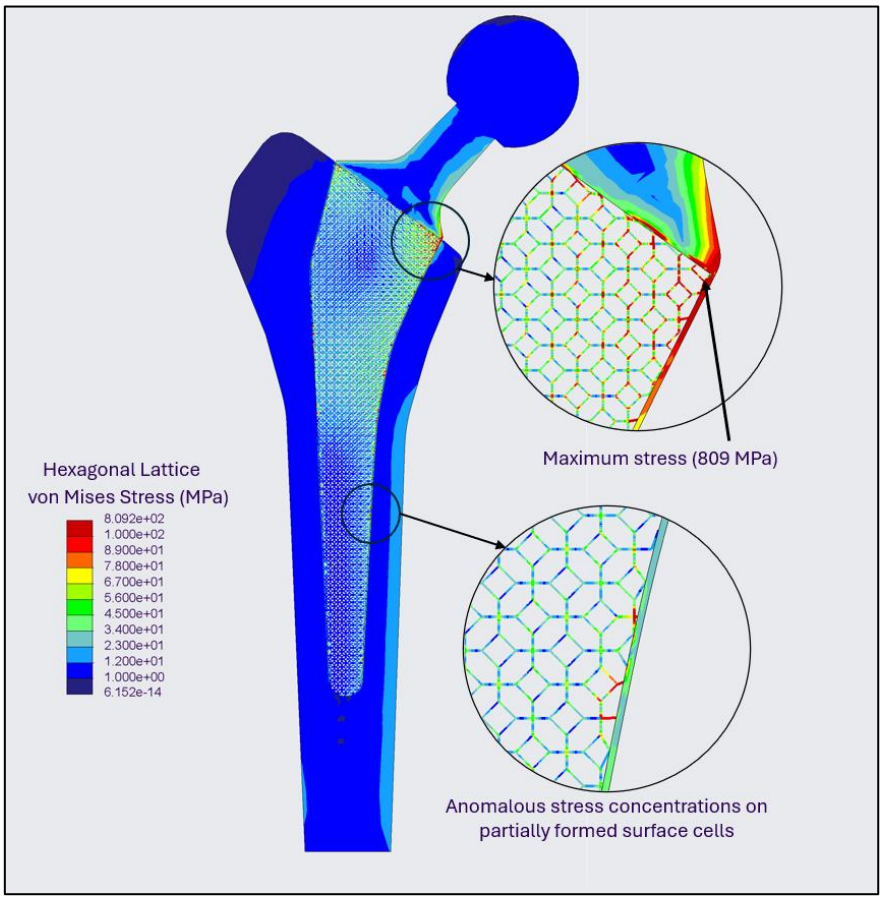

Figure 4-19: Hexagonal lattice porous stem and proximal femur stress distribution

The stress distribution for the centre plane of the diamond-star lattice femoral stem is shown in Figure 4-20. As with the hexagonal lattice, the point of maximum stress occurs on a partially formed, surface layer lattice member in the corner between the solid stem, lattice and wall section. The maximum stress observed in this member is approximately 3.92GPa. Excluding this member and those directly adjacent to it, the next highest stress member is 168MPa. The diamond-star lattice stem also shows the presence of anomalous stress concentrations at partially formed surface cells throughout the exterior of the model. In these instances, the stress concentrations do not occur on the beam member, but on the outer wall. As with all the porous lattices, the stress within the stem is substantially higher than the surrounding femur.

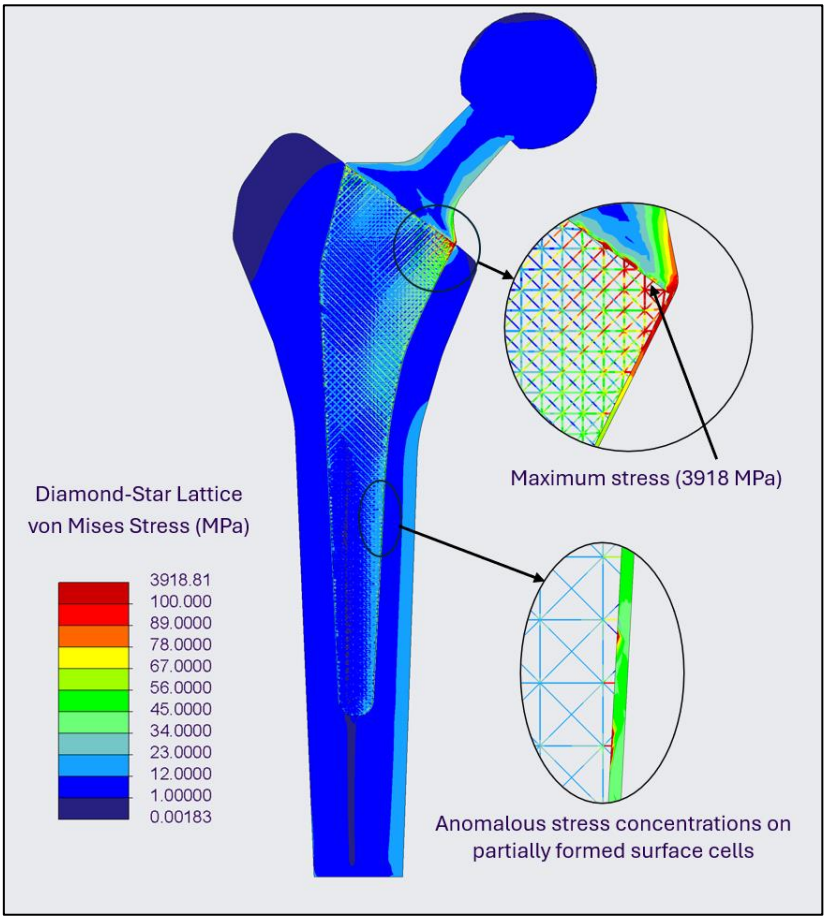

Figure 4-20: Diamond-star lattice porous stem and proximal femur stress distribution

4.7 Femoral Stem – Stress Shielding

The implanted femurs were analysed independent of their stems for the purpose of calculating stress shielding. Figure 4-21 shows a comparison of the stress distribution for each proximal femur. Because stress shielding is measured as a relative difference between the stress distribution of an intact femur and an implanted femur, the stress within the stem was not required for this calculation. A higher stress within the femur indicates a lower occurrence of stress shielding. The numbered zones in Figure 4-21 represent the seven Gruen zones.

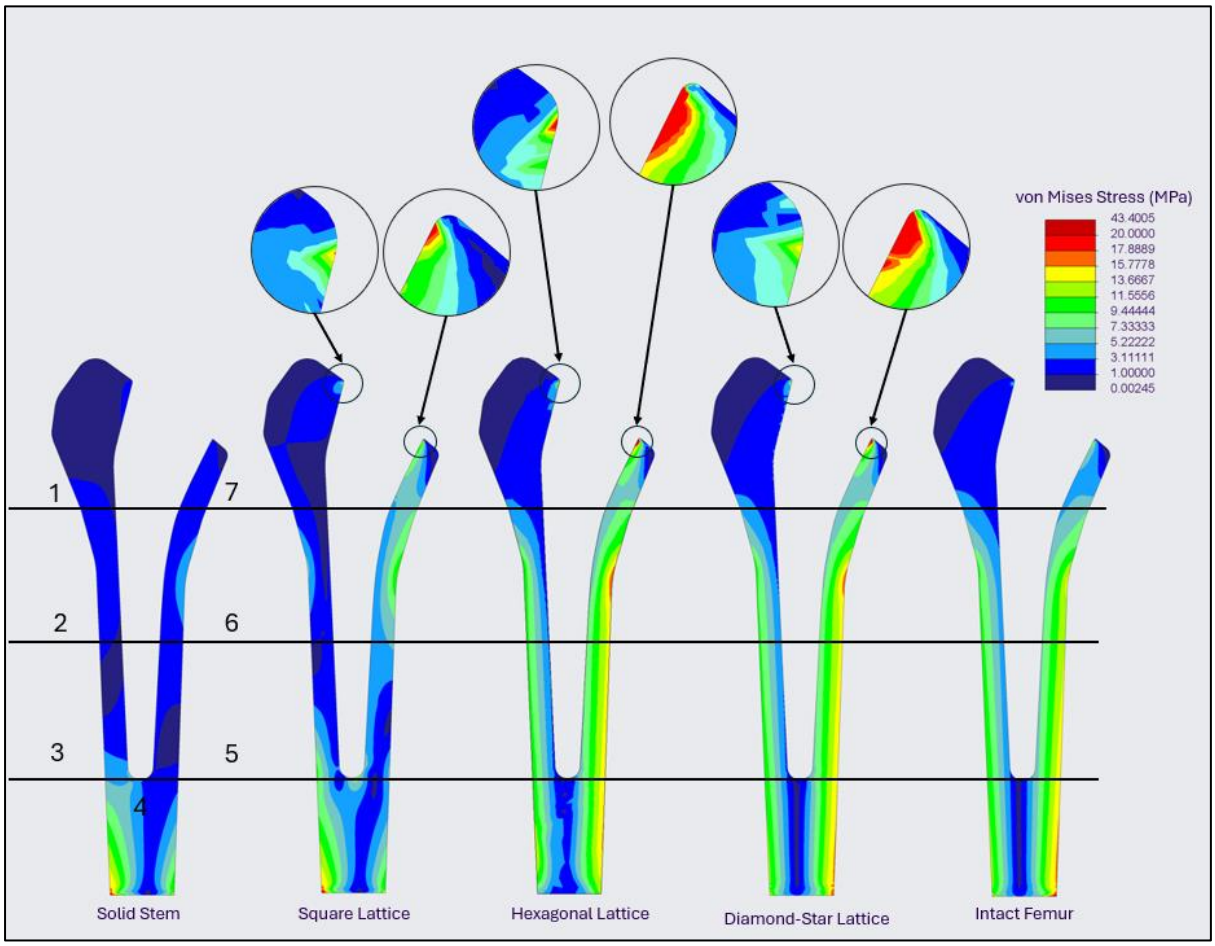

Figure 4-21: Comparison of stress distribution for each proximal femur split into 7 Gruen zones

It is observed that the average stress distribution of the square lattice is considerably less than that of the intact femur, more closely resembling the stress distribution of the solid stem. This indicates a relatively high amount of stress shielding is occurring in the square lattice femur.

In contrast, the hexagonal lattice and diamond-star lattice femurs appear to have a similar stress distribution to that of the intact femur. Further, the hexagonal and diamond-star lattices show higher maximum stress within Gruen zone 1, 6 and 7. All the porous stems show large stress concentrations in zones 1 and 7. These occur at the tangential intersection point between the rounded corners of the femur and femoral stem. The stress concentration in zone 7 is also coincident with the corresponding maximum stress concentration within each stem.

The results for all average stress calculations, and subsequent stress shielding values by Gruen zone are presented in Table 4-9. The stress concentrations in Gruen zone 1 and 7 resulted in large negative stress shielding values. A negative stress shielding value means there is a greater amount of stress placed on the proximal femur after implantation compared to an intact femur. Gruen zone 6 also returned negative stress shielding values for the hexagonal and diamond-star lattice types.

Table 4-9: Average stress and Stress shielding by Gruen zone for each stem type

		Intact Femur	Solid Stem	Square Lattice	Hexagonal Lattice	Diamond Lattice
Gruen zone 1	Average Stress (MPa)	2.032	0.604	13.135	6.656	8.103
	Stress Shielding (%)		70.272	-546.423	-227.545	-298.755
Gruen zone 2	Average Stress (MPa)	7.087	1.782	2.988	6.798	6.525
	Stress Shielding (%)		74.855	57.845	4.078	7.930
Gruen zone 3	Average Stress (MPa)	7.314	0.964	3.841	6.532	6.649
	Stress Shielding (%)		86.827	47.491	10.699	9.092
Gruen zone 4	Average Stress (MPa)	7.993	3.716	4.017	7.956	8.326
	Stress Shielding (%)		53.509	49.750	0.469	-4.160
Gruen zone 5	Average Stress (MPa)	10.608	1.422	2.232	10.537	9.330
	Stress Shielding (%)		86.599	78.955	0.669	12.048
Gruen zone 6	Average Stress (MPa)	10.347	3.251	7.428	11.338	11.838
	Stress Shielding (%)		68.579	28.212	-9.578	-14.416
Gruen zone 7	Average Stress (MPa)	10.855	2.754	12.361	15.617	13.779
	Stress Shielding (%)		74.628	-13.877	-43.869	-26.940

Figure 4-22 shows a visual comparison of the mean stress across each Gruen zone, including the effects of any stress concentration. The graph shows all porous stems result in a higher mean femoral stress than the solid stem across all Gruen zones. The mean stress in the solid stem femur is much lower than that of the intact femur across all Gruen zones. The hexagonal lattice and diamond lattice result in similar mean stress values which are within 2MPa of the intact femur, except for in Gruen zones 1 and 7, which contain substantial stress concentrations.

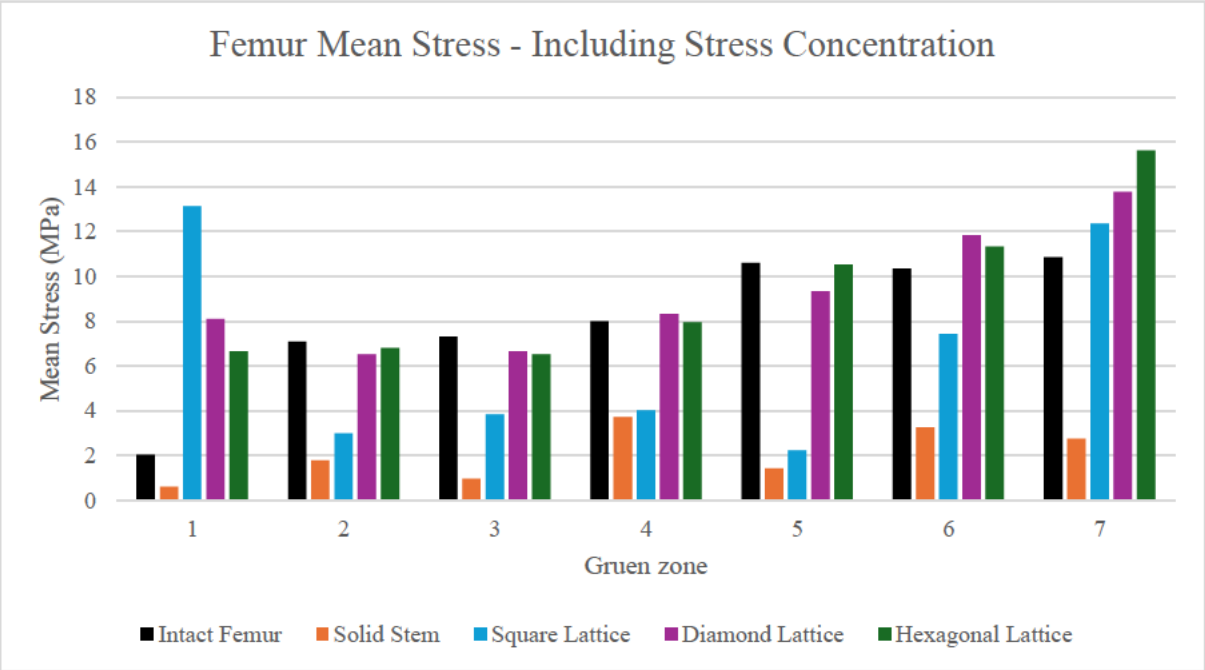

Figure 4-22: Comparison of mean stress in proximal femur across each Gruen zone, Including stress concentrations

Figure 4-23 shows the percentage of stress shielding in each femur including the effect of stress concentrations. The solid stem produced stress shielding values of between 53% and 87%. The results show that diamond-star and hexagonal lattices perform similarly, reducing stress shielding to below 12% in Gruen zones 2, 3, 4 and 5, and returning negative stress shielding values in zones 1, 6 and 7. In zones 2 to 6 the square lattice produced stress shielding between 28% and 79%, performing better than the solid stem, but considerably worse than the hexagonal and diamond-star. However, in zones 1 and 7 the square lattice also resulted in negative stress shielding, greatly outperforming the solid stem. The results show stress concentrations in zones 1 and 7 have a major effect on the performance of the stem.

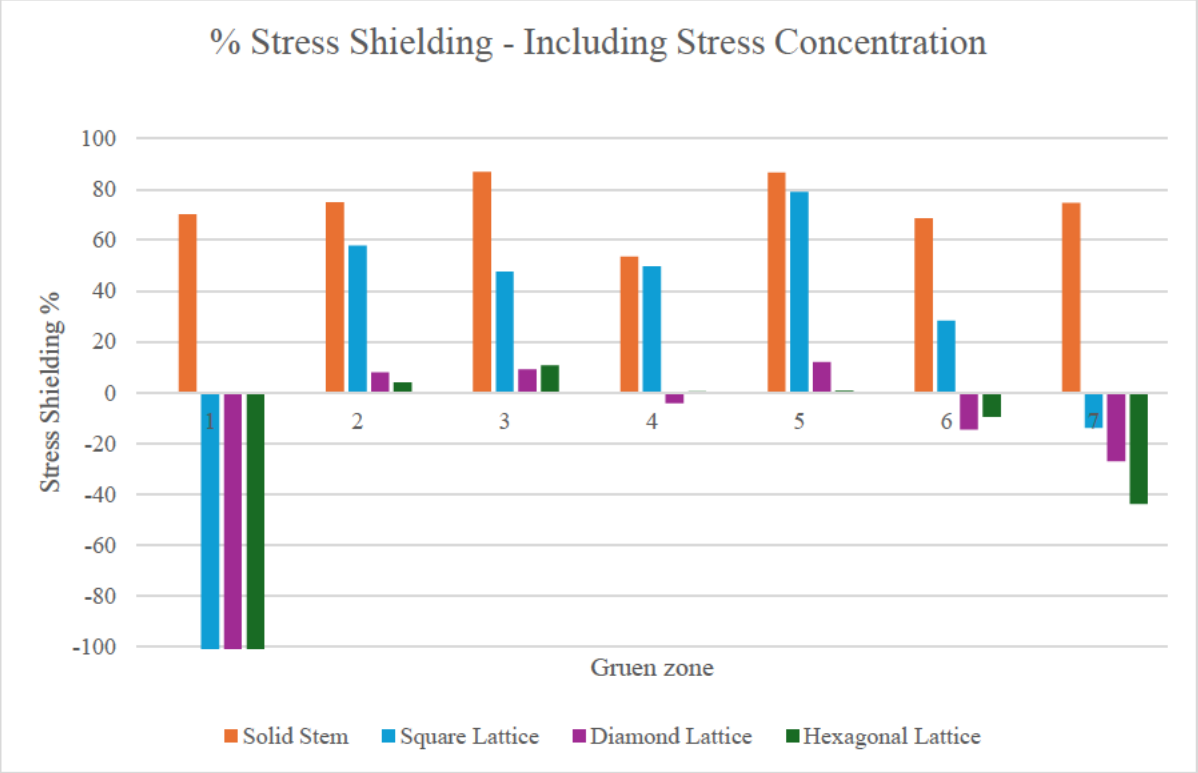

Figure 4-23: Comparison of stress shielding in proximal femur across each Gruen zone, Including stress concentrations

To reduce the effect of stress concentrations on the results, the mean stress in each Gruen zone was recalculated using measurements taken 1mm from the surface. The new results are presented in Table 4-10.

Table 4-10: Average stress and Stress shielding by Gruen zone for each stem type

		Intact Femur	Solid Stem	Square Lattice	Hexagonal Lattice	Diamond Lattice
Gruen zone 1	Average Stress (MPa)	2.032	0.604	2.361	1.979	2.677
	Stress Shielding (%)		70.272	-16.169	2.603	-31.733
Gruen zone 2	Average Stress (MPa)	7.087	1.782	2.988	6.798	6.525
	Stress Shielding (%)		74.855	57.845	4.078	7.930
Gruen zone 3	Average Stress (MPa)	7.314	0.964	3.841	6.532	6.649
	Stress Shielding (%)		86.827	47.491	10.699	9.092
Gruen zone 4	Average Stress (MPa)	7.993	3.716	4.017	7.956	8.326
	Stress Shielding (%)		53.509	49.750	0.469	-4.160
Gruen zone 5	Average Stress (MPa)	10.608	1.422	2.232	10.537	9.330
	Stress Shielding (%)		86.599	78.955	0.669	12.048
Gruen zone 6	Average Stress (MPa)	10.347	3.251	7.428	11.338	11.838
	Stress Shielding (%)		68.579	28.212	-9.578	-14.416
Gruen zone 7	Average Stress (MPa)	10.855	2.754	6.761	8.337	9.589
	Stress Shielding (%)		74.628	37.713	23.199	11.660

Figure 4-24 shows the values for mean stress in each Gruen zone when stress measurements were made 1mm from the surface to mitigate stress concentration. The figure shows the mean stress in zone 1 for all porous lattice types has been reduced to a similar value to that of the intact femur. The mean stress for all stem types in zone 7 has also been reduced to below that of the intact femur, but the reduction is less pronounced in this zone.

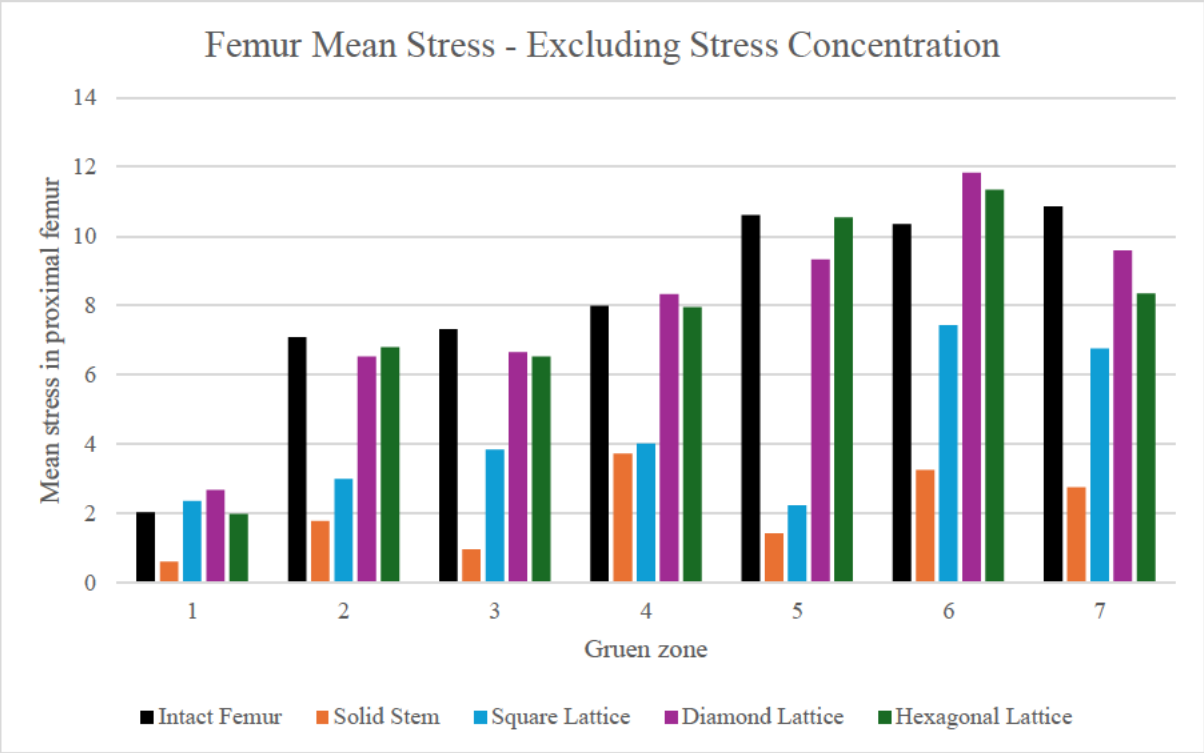

Figure 4-24: Comparison of mean stress in proximal femur across each Gruen zone, excluding stress concentrations

Figure 4-25 shows the stress shielding in each Gruen zone when stress measurements were made 1mm from the surface. The results show that negative stress shielding is still occurring in zones 1, 4 and 6, however the negative stress shielding values for zone 7 no longer occur. The square lattice stem performs much better in zone 1 than in all other zones, maintaining the negative stress shielding value. The diamond-star and hexagonal lattice types remain the highest performing stems in terms of reducing stress shielding, resulting in a stress shielding of between -32% and 37%. The measurement offset distance of 1mm was an arbitrarily chosen value, however it was done to show how susceptible the results are to stress concentration and measurement techniques.

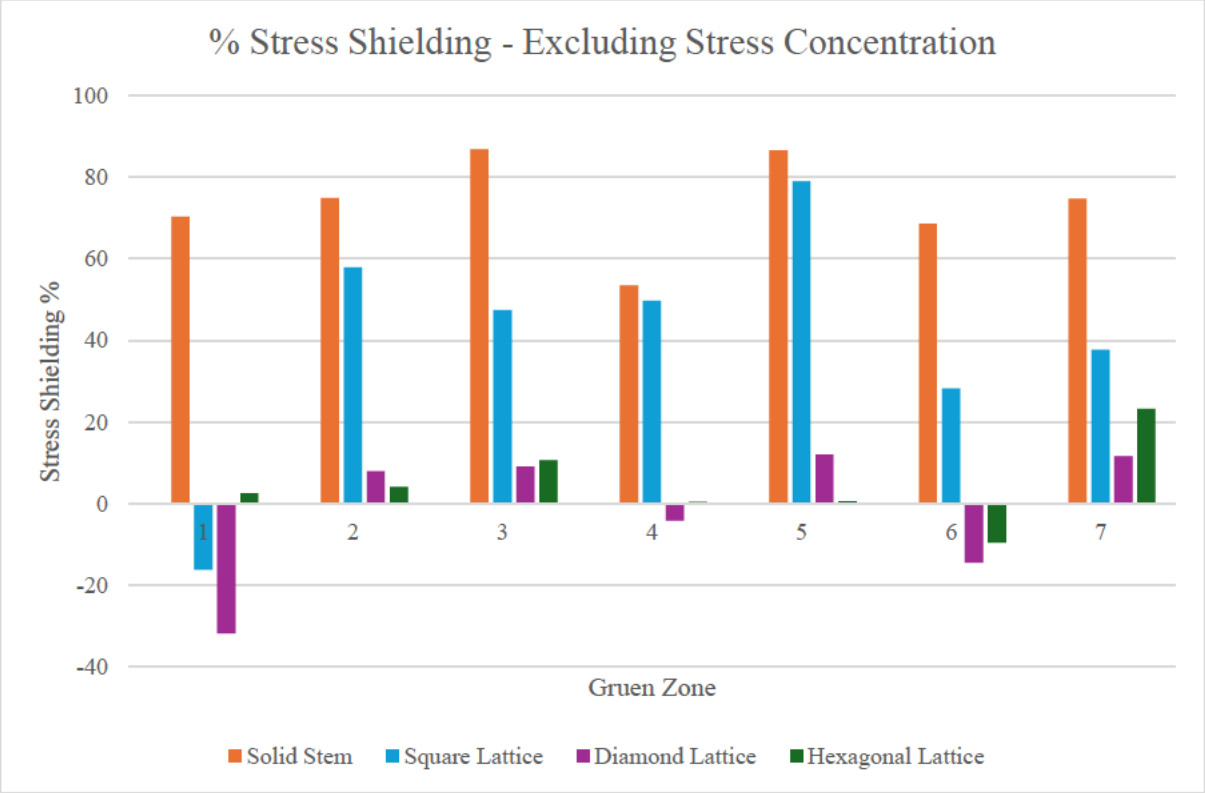

Figure 4-25: Comparison of stress shielding in proximal femur across each Gruen zone, excluding stress concentrations

4.8 Femoral Stem – Stem Strength and Fatigue Life

The maximum and minimum stress within the lattice structure of each femoral stem were recorded and used to calculate the alternating stress and mean stress to determine the fatigue life, and structural integrity of the stem. As with the calculation of stress shielding, this process was noted as highly susceptible to stress concentration and partially formed cells. Table 4-11 shows the results including all cells, and Table 4-12 shows the results excluding the partially formed surface cells. The maximum stress in all porous stems is drastically reduced when removing the effect of these problematic cells.

Table 4-11: Stress for each femoral stem - including surface cell stress concentrations

	σ_{min} (MPa)	σ_{max} (MPa)	σ_a (MPa)	σ_m (MPa)
Solid Stem	0.00075	56.99	28.49	28.49
Hexagonal lattice	0.00271	809.0	404.59	404.60
Square lattice	0.00191	681.1	340.4	340.50
Diamond-star lattice	0.00183	3918.2	1959	1959

Table 4-12: Stress for each femoral stem - excluding surface cell stress concentrations

	σ_{min} (MPa)	σ_{max} (MPa)	σ_a (MPa)	σ_m (MPa)
Solid Stem	0.00075	56.99	28.49	28.49
Hexagonal lattice	0.00271	132.30	66.14	66.15
Square lattice	0.00191	153.60	76.79	76.80
Diamond-star lattice	0.00183	168.50	84.24	84.25

Figure 4-26 shows a graph of the Soderberg failure criteria, with the alternating and mean stress values for each lattice type plotted, assuming a safety factor of 3, at 10^7 cycles. If the points lay below the line, the structure should not fail at the given stresses. The points marked with circles indicate when partially formed surface cell stress measurements are used, and the points marked with an x indicate the stress values without considering these cells. All porous stems fail when including the effect of partially formed cells, however all stems do not fail when removing the effect of surface cells. The yield strength of the material is 1070MPa. Even with a safety factor of 2, all porous stems do not meet the required strength when considering the effects of surface cells, however without the surface cells the structures pass a safety factor of 6. This is another example of how susceptible the model is to individual stress concentrations.

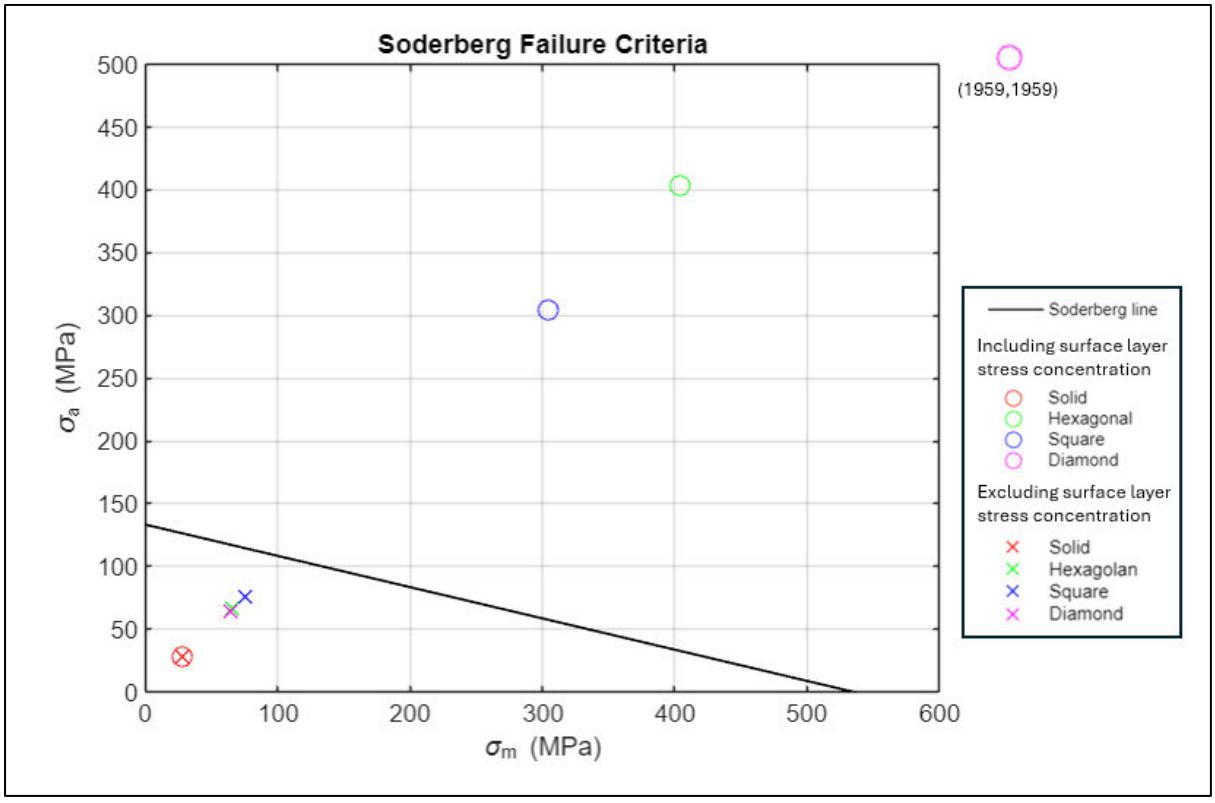

Figure 4-26: Soderberg Line Failure criteria

Chapter 5 Discussion

This chapter will discuss the accuracy, validity and relevance of the results obtained in Chapter 4. The discussion is broken down by the three stages of the methodology. Section 5.1 focuses on model validation by comparing measured and analytical error rates of the square lattice FEA. Section 5.2 discusses the different methods used for calculating elastic modulus, comparing the change in elastic modulus between various lattice types and the issues encountered during the process. Lastly, section 5.3 discusses the stress shielding values achieved by each porous stem, design considerations and limitations of the results.

5.1 Square Lattice FEA – Model Validation

The objective of the square lattice tests was to confirm the accuracy and validity of the model, identify potential sources of error, compare the suitability of different methods for measuring stress and strain, and identify the minimum number of cells required to accurately represent a lattice. These objectives were achieved, and some incidental findings were noted.

In the square lattice testing, it was observed that the behaviour of the surface cell layer under load does not accurately represent the behaviour of the bulk structure. This became a persistent issue in all subsequent tests. For all square lattice sample tests, the compressive load was applied as an evenly distributed pressure acting on the top surface of the lattice. This meant a portion of the load was applied to the horizontal lattice struts on the upper surface, which would not normally bear a load perpendicular to their axis. The resulting bending moment in the upper struts generated maximum values of stress and strain far higher than those observed in the bulk of the structure. Additionally, the outer cells shared fewer supporting faces with adjacent cells, leading to a greater degree of displacement occurring along their vertical plane. This was especially prevalent in the corner cells, which being

furthest from the centroid of the structure, and having the least amount of adjacent support showed the greatest degree of deformation. The maximum stress and strain were therefore always located within an outer surface cell. The behaviour of the outer cell layer varying from the bulk of the structure was also observed in the hexagonal and diamond-star lattice samples and femoral stem simulations. In the case of the femoral stem simulations, the variation in behaviour was primarily due to partially formed and non-uniform cells rather than the applied loading conditions. Measuring the maximum stress and deformation in the outer cell layer is important for analysing the occurrence of structural failure, however, to accurately model the elastic behaviour of the entire lattice, the surface layer measurement had to be removed.

The value of von Mises stress (σ_{VM}), measured strain (ε_m) and measured normal stress (σ_{YY}) were highly influenced by the presence of stress concentrations. σ_{VM}, σ_{YY} and ε_m were calculated as the arithmetic mean of their minimum and maximum respective values. Where large stress concentrations with steep gradients were present within the structure, such as those occurring on the upper surface cell layer, it skewed the mean values. The effect of this can be observed when comparing measurements including the surface layer to measurements excluding the surface layer. When including the surface layer, the relative error between σ_{YY} and analytically calculated stress (σ_c) was high as 759.3%, the relative error between σ_{VM} and σ_c was up to 693.2%, and the relative error between ε_m and the displacement-calculated strain (ε_c) was up to 193.5%. After removing the surface layer measurements, the error across all measurements dropped substantially, to a maximum of 82.6% between σ_{VM} and σ_c, 8.96% between σ_{YY} and σ_c, and 20.36% between ε_m and ε_c. The large reduction in error rate when removing the surface layer can be more clearly observed across all samples in Figure 4-8 and Figure 4-9. Although excluding the surface layer removed the largest stress concentration, smaller stress concentrations were still present across the lattice structure,

primarily at internal corners. These remaining stress concentrations contribute to the residual error.

The measured normal stress (σ_{YY}) and analytically calculated normal stress (σ_c) are closely correlated, indicating that the model is producing valid results. The only direct comparison that can be made to validate the model between analytical and measured results is between σ_c and σ_{YY}. Both methods calculate principal stress normal to the axis of loading and can therefore be directly compared. Once the surface cell layer effects were removed, the relative error of σ_{YY} to σ_c was between 1.73% and 8.96%. σ_c was calculated analytically based on applied force and average cross-sectional area, and σ_{YY} was directly measured from the FEA model. The low error rate between the analytical calculation of stress and measured value show that the model is producing accurate, valid data. It is noted that the low error rate only occurs when the surface cell measurements of σ_{YY} are removed.

The measured VM stress (σ_{VM}) varies from both the analytically calculated stress (σ_c) and measured normal stress (σ_{YY}), indicating that VM stress may not be suitable for calculating the elastic modulus. The relative error between the VM and analytically calculated normal stress was between 13.56% and 82.6% even after surface cell effects were removed. σ_{VM} is not a measure of principal stress and therefore cannot be directly compared to σ_c or σ_{YY}.

The measured strain (ε_m) is closely correlated with the displacement-calculated strain (ε_c), once the effect of surface stress concentration was removed. Removing the surface layer cell stress concentrations significantly reduced ε_m. ε_c was calculated using the average displacement of the upper surface measured at the corner nodes, so was unaffected by the increased strain on the outer cells. After removing surface cell measurements, the relative error between ε_m and ε_c was between 0.05% and 22.36%. Both methods for calculating strain are based on measured FEA data so cannot be directly used to validate the model, however,

they can be compared to each other for accuracy. Displacement-calculated strain was shown to be less prone to the effects of surface loading conditions and stress concentrations than the directly measured strain. This indicates ε_c is a more accurate method for measuring strain.

An $n = 4$ lattice was shown to sufficiently approximate the behaviour of a full-scale lattice. The lattice porosity was identified as a function of number of cells (n) as well as strut thickness (t) and cell size (c). It was observed that over the range of t and c used, the porosity of an $n = 4$ lattice was within 3% to 10% of the value obtained from an $n = 100$ lattice. It is important to note that these exact error values were calculated based on a square lattice type at a cell size of $c = 0.5$mm and a strut thickness of $0.05\text{mm} < t < 0.20\text{mm}$, and the error rate for different lattice types will vary. It was not possible to analytically calculate the porosity error rate as a function of number of cells for the more complex lattices. A similar analysis was carried out by Mehboob et al. (2018), and the authors concluded that for diamond, cubic and BCC lattice types, the measured change in elastic modulus converged on a single value at $n = 4$ cells. It was therefore assessed that the error rate introduced by using an $n = 4$ lattice sample in this paper for all lattices was less than or equal to 10%.

5.2 FEA of Various Lattice Types - Elastic Modulus

The analysis of the square, hexagonal and diamond-star lattice utilised two different methods for calculating the equivalent elastic modulus and its relative change, over a range of porosities. The two methods are compared with each other and existing literature to test their validity. Both methods for calculating the equivalent elastic modulus showed that as porosity increased, the equivalent elastic modulus decreased across all lattice types, however, the magnitude and shape of the function varied by method.

The measured equivalent elastic modulus (E_m) decreased exponentially as porosity (φ) was increased, in all tested lattice types. The hexagonal and diamond-star lattice performed similarly, achieving a moderate measured relative change elastic modulus (K_m), of up to 30.1% at 90% porosity, and 22.19% at 88.6% porosity respectively. The square lattice performed marginally better, achieving a 47.89% reduction at 87.7% porosity.

The calculated equivalent elastic modulus (E_c) decreased linearly as porosity (φ) was increased, in all tested lattice types. The hexagonal and diamond-star lattice performed similarly, achieving a large reduction in calculated relative change elastic modulus (K_c) of up to 95.5% at 90% porosity, and 87.17% at 88.6% porosity respectively. The square lattice performed considerably worse, achieving a 54.09% reduction at 87.7% porosity.

Other similar studies of Ti_6Al_4V lattices show a linear decrease (Rotta, Seramak & Zasińska 2015), (Kováčik 1999), or slight exponential decay relationship between porosity and elastic modulus (Mehboob et al. 2018), (Wang et al. 2013). Only studies involving alternate materials such as alumina, gypsum and silica (Boccaccini & Fan 1997), or femoral bone (Jones 2008) show the same exponential decrease observed in E_m. Additionally, previous studies of Ti_6Al_4V achieve a relative reduction in elastic modulus similar to those observed with K_c. Eldesouky et al. (2017) achieved a 92% reduction at a porosity of 57%, Eldesouky, El-Hofy and Harrysson (2017) achieved a 95% reduction at 64% porosity. Mehboob et al. (2018) achieved a 95% reduction at 89.6% porosity.

The calculated equivalent elastic modulus (E_c) of each lattice type much more closely aligns with the existing literature than the measured equivalent elastic modulus (E_m). Additionally, the E_c value for each lattice type correlates with the results of stress shielding testing. In the stress shielding testing, the diamond-star and hexagonal lattices performed similarly, eliminating almost all stress shielding, and the square lattice performed worse, only

marginally reducing stress shielding. These factors indicate that the analytical stress-based approach of E_c is a more appropriate method for calculating elastic modulus than the measured VM stress-based approach of E_m.

Initially it was hypothesised that the use of σ_{VM} would be beneficial to allow for analysis of more complex lattice types. The VM stress is not directional, so if measurements could be taken under multiaxial loading, the results would be less dependent on cell orientation and strut angle. Additionally, mean VM stress was used to calculate stress shielding and fatigue strength in the femoral stem analysis, so using it to calculate *E* would allow for a more direct comparison of these results. However, the variance observed in the results compared to existing literature, the susceptibility to error due to stress concentrations and the lack of correlation between elastic modulus measurement and stress shielding when using VM stress indicate that VM stress is not suitable for calculating elastic modulus.

An additional source of error for calculation of elastic modulus is that, in this study, only a single value of *E* was calculated at a fixed load for each porosity value. If *E* was calculated over multiple loads for each porosity value and plotted, It would provide a more accurate value (Eldesouky, El-Hofy & Harrysson 2017).

5.3 Femoral Stem FEA – Stress Shielding

The results of the femoral stem simulations illustrate that using a porous femoral stem is an effective method for reducing the occurrence of stress shielding. At 80% porosity the diamond-star and hexagonal lattice produced similar results, reducing stress shielding in Gruen zones 2-6 to a maximum 12%, with stress shielding completely negated in some zones. The square lattice performed worse, achieving a stress shielding between 28% and 78% in Gruen zones 2-6. Arabnejad et al. (2017) found that bone reabsorption and density loss are

likely to occur at stress shielding of greater than 50%, so all porous lattices modelled in this project were effective in reducing or preventing the occurrence of bone reabsorption. Although a positive outcome was achieved within this project, the results were prone to a large degree of error. The method for calculating average stress, assumptions and idealizations made within the model mean the simulated results may not accurately reflect real world outcomes.

In all simulations, Gruen zones 1 and 7 contained large stress concentrations at the bone-prosthetic interface which effected the validity of their calculated stress shielding values. As with the lattice samples, stress values within the femur were calculated as the arithmetic mean of minimum and maximum VM stress. The anomalous stress concentrations in zones 1 and 7 resulted in mean stress values that did not represent the behaviour of the bulk of the bone in their respective zone. All porous stems returned a very large negative stress shielding value in zone 1 and a smaller negative value in zone 7, indicating the stress in the femur after implantation is much higher in these zones than the intact femur. In the case of the hexagonal lattice, a negative stress shielding value as large as -546% was observed in zone 1. The negative stress shielding observed in zones 1 and 7 did not correlate with the occurrence of stress shielding across zones 2-6. When the stress value of the outer 1mm of femoral tissue was excluded the stress shielding observed in Gruen zones 1 and 7 across all porous stems increased dramatically to between -31.7% and 2.60% in zone 1 and between 11.6% to 37.7% in zone 7. Removing the outer 1mm measurements did not have a significant effect on the stress values of zones 2-6. Because of the susceptibility of the stress shielding values in zones 1 and 7 to the measurement technique, all stress shielding results for these zones must be considered invalid. To accurately calculate average stress in these zones, a multi-point method of calculating average stress is required, such as that conducted by Arabnejad et al. (2017) who used 75 sample points across the femur. The use of a multi-point system for

calculating average stress and strain would have also improved the accuracy of the lattice sample tests and elastic modulus calculations.

Using an average value to calculate stress shielding in each Gruen zone does not indicate how the stress is distributed within the zone. Femoral bone is of variable density, so even if the average stress within a section of the femur is the same after implantation, if the stress distribution is altered, some degree of stress shielding may still occur. The results indicate that the stress distribution remained comparable between the implanted and intact femurs, however the model did not consider the change in geometry of the femoral head and trochanter that would have occurred during a real THA procedure. In the model, the intact femur was simulated using the geometry of a solid stem-implanted femur, with the material of the stem being set to bone. This simplification was made for ease of comparing results, however the geometry of an actual intact femur would be considerably different in Gruen zones 1 and 7. In these zones, large portions of bone are removed during the THA procedure, which is not reflected in the model. Therefore, the modelled stress distribution of the intact femur in zones 1 and 7 is not an anatomically accurate representation. The geometry of the femur in zones 2-6 is unaffected by this problem, however the stress distribution in these zones may still be affected by the change in zones 1 and 7. Using 3D imaging and AM techniques, bespoke designs for femoral stems can be produced that focus on replicating the original geometry of the femoral head to maintain the pre-implanted stress distribution and reduce the effects of stress shielding, such as the design by Corona-Castuera et al. (2021).

The effect of completely negating stress shielding for the diamond-star and hexagonal lattices was expected, given the large reduction in elastic modulus that was achieved. The study assumed bone to have an elastic modulus of E = 19.6GPa. At approximately 80% porosity the hexagonal and diamond-star lattices had an elastic modulus of $E_C = 23.73$GPa, and

$E_C = 25.20$GPa respectively. Given how close the values of elastic modulus are to that of bone, it was expected that the effect of stress shielding would be almost completely negated. The square lattice showed the lowest reduction in equivalent elastic modulus as a function of porosity in the sample tests when calculated as E_c. At 80% porosity the elastic modulus for the square lattice is $E_C = 49.94$GPa, roughly twice that of the other two lattice types, however this resulted in an average stress shielding value 4038% greater than the hexagonal lattice and 2399% greater than the diamond-star lattice across Gruen zones 2-6. The higher stress shielding of the square lattice compared to the diamond-star and hexagonal lattice was expected, but not to the degree that was observed. This suggests that the relationship between elastic modulus and stress shielding may be nonlinear, however given the lack of additional data points, this relationship was unable to be proven in this study. Alternatively, the inconsistency between the elastic modulus tests and the stress shielding tests for the square lattice may be attributed to the orientation of the square lattice struts.

The elastic modulus was calculated using uniaxial loading in the orientation of the square struts, however the stress shielding simulations were run under multiaxial loading. The hexagonal and diamond-star lattices contained struts at multiple angles which made them behave in an isotropic manner across the varying loading conditions. The 90-degree orientation of the square lattice struts may have resulted in a poorer load distribution under the multiaxial loading, leasing to a variation between elastic modulus and stress shielding results.

The reduction in stress shielding achieved by the diamond-star and hexagonal lattice across Gruen zones 2-6 is comparable to a range of similar studies. Jetté et al. (2018) used a diamond lattice, with an average pore size of 800μm and porosity of 68% to achieve 15% stress shielding, a reduction of 30% compared to a solid stem. Fraldi et al. (2010) used

topology optimisation and a variable density femoral stem that completely negated stress shielding in Gruen zones 2-6, however up to 15% stress shielding remained in zones 1 and 7. Singh and Tandon (2018) used a heterogeneous lattice with variation of material and porosity to reduce stress shielding by 31% compared to a solid implant. He et al. (2018) achieved a stress shielding of 10-16% using a variable density titanium lattice, which was a 57.3% reduction compared to the solid stem. Bliss et al. (2023) reported an 18% reduction in stiffness, and a corresponding 30% reduction in stress shielding compared to a solid stem using a hexagonal lattice. The stress shielding observed in the diamond-star and hexagonal lattice across Gruen zones 2-6 aligns with these previous studies, indicating the results are valid. The reduction in stress shielding compared to a solid stem cannot be directly compared across studies since they all use a different baseline, however the stress shielding compared to the intact femur can be directly compared.

The bone used in this study was assumed to be solid and a constant density, which is a notable source of error. Real bone is porous and of variable density. The elastic modulus of bone can be described as a function of the density (Arabnejad et al. 2017) or as a function of porosity (Jones 2008). Additionally, the properties of the bone depend largely on the type of bone tissue, with the outer trabecular layer being higher density, with a higher elastic modulus than the inner coronal tissue (Sheridan et al. 2021). The properties of bone depend on age, gender and individual health (Havaldar, Pilli & Putti 2014). Havaldar, Pilli and Putti (2014) reported the elastic modulus of femoral tissue to be as low as 330MPa, and Hezil et al. (2022) report it as 3GPa, however many studies analysing stress shielding use a value of approximately 20GPa (Hedayati & Fallah 2015), (Liu et al. 2021). Because the effect of stress shielding in this paper is measured as a relative change in mean stress between an implanted and intact femur, the error introduced by simplifying bone tissue to a solid homogeneous structure will be reduced, however this will still affect the results.

The requirement to include a solid outer shell to contain the lattice members meant the objective of designing a fully porous femoral stem to encourage bone ingrowth was not achieved. As explained in Chapter 3, due to the limitations of the modelling software the lattice structure had to be modelled using simplified beam geometry, which could not directly interact with other solid parts in the FEA environment. This required the inclusion of a thin, solid outer shell to the femoral stem, allowing the part to interact with the surrounding femur. The overall effect of the shell on the stress shielding properties of the stem was assessed to be negligible. The shell was the same thickness as the lattice struts, and the stem was modelled as a 4mm slice of the full 3D structure, so the additional volume added by the shell accounted for less than 0.1% over the overall structure. Given that the method for calculating stress shielding was highly prone to error at points of stress concentration, the inclusion of a solid surface shell likely improved the accuracy of the results by evenly distributing load to the surrounding femur, rather than the near-point loads that would have been experienced by the partially formed surface cell struts. The inclusion of a solid shell does however significantly change the structural analysis of the stem itself.

The results obtained for the fatigue and failure analysis were highly dependent on the inclusion of surface cell and shell interaction. When surface cell and shell interactions were considered, all the porous stems failed under the Soderberg failure criteria and did not meet the required yield strength, however the bulk of the lattice remained comfortably below these thresholds with a safety factor of 3. This illustrates one of the key findings of this project, being that to design a successful porous femoral stem, the design of the surface layer cells is critical.

Creating the required 3D curvature of the femoral stem using a regularly repeating lattice with constant porosity is not possible at a feasible cell size. The surface cells will always be

intersected and partially formed, impeding their ability to regularly distribute load, creating points of stress concentration and increasing the chance of localised failure. The common failure point of a regular lattice could be removed by trimming all partially formed cell struts and including a solid outer layer of variable thickness to match the geometry of the stem to the geometry of the femur. Even if a surface treatment is applied to the stem's outer surface to allow for improved osteointegration, this design would only be partially porous. A more comprehensive solution to the design of a fully porous femoral stem would be to use an irregular lattice such as that used by Wang et al. (2021) or a lattice with variable density and cell size, used by Singh and Tandon (2018). These irregular designs allow for complete surface cells to be generated as close to their intended geometry as possible, while conforming to the required curvature of the femur, eliminating partially formed cells.

The inclusion of variable density and cell size allows for topology optimisation to be conducted, allowing the stem to mimic the variable porosity and elasticity of the surrounding bone. Conventionally, topology optimisation has been used to maximise stiffness while minimising the amount of material used. In the use case of reducing the effect of stress shielding, the opposite outcome is required from topology optimisation, where it will be optimised for minimising rigidity while retaining as much material as possible. The same problem occurs when examining lattice type for use in reducing stress shielding. Conventional engineering lattices commonly used in AM, such as those used in this project, are generally designed to maintain rigidity while minimising the amount of material used. Again, this does not align with what is desired when trying to increase elasticity. This project has highlighted the need for further research into the design of irregular lattices and topology optimisation techniques that focus on surface cell optimisation, and maximising elasticity while maintaining structural strength.

Chapter 6 Conclusions and Further work

In this project, three porous low elastic modulus femoral stems were designed, simulated and analysed with the objective of reducing stress shielding and maximising osteointegration after Total Hip Arthroplasty (THA).

Finite Element Analysis (FEA) was conducted on square, hexagonal, and diamond-star Ti_6Al_4V, lattice structures over a range of porosities, to evaluate their effectiveness in replicating the mechanical properties of natural bone by reducing their elastic modulus. The square lattice achieved a 54.1% reduction in elastic modulus at 87.7% porosity, the hexagonal lattice achieved a 95.5% reduction at 94.1% porosity, and the diamond-star lattice achieved an 87.2% reduction at 88.6% porosity. The results established a linear relationship between the increase in porosity and reduction in elastic modulus. At the maximum tested porosity, the hexagonal and diamond-star lattices were able to achieve an elastic modulus lower than that of cortical femoral bone at 19.6GPa, indicating that they are suitable for use in a low elastic modulus femoral stem.

FEA was conducted on a 2.5-dimensional representation of a 3-dimensional human femur and in-situ porous femoral stem to measure the occurrence of stress shielding between an implanted and intact femur. At 80% porosity the hexagonal and diamond-star lattices performed comparably well, reducing stress shielding in Gruen zones 2-6 to a maximum of 12% and completely negating the stress shielding in some zones. The square lattice achieved a stress shielding value between 28% and 78% in Gruen zones 2-6, moderately reducing the effect of stress shielding in comparison to a solid stem. The results indicate that both the hexagonal and diamond-star lattices are highly effective in reducing the effect of bone density loss secondary to stress shielding. The reduction in stress shielding achieved in this project

reflects what has been observed in previous studies, indicating that the results are valid. The stress shielding values measured for Gruen zones 1 and 7 were assessed to be invalid, due to large stress concentrations in these zones skewing the average stress calculation.

The objective of designing a fully porous femoral stem to maximise osteointegration was not achieved. Due to computational limitations, a solid outer shell was required to surround the porous lattice of the femoral stem. It was observed that the loading conditions and resultant stresses of surface cells varied considerably from the bulk of the structure in both fully and partially porous lattices. Additionally, any partially formed surface cells had compromised structural integrity and were prone to stress concentration, deformation and failure.

To build upon the findings of this project, several recommendations for future work have been identified. Physical testing is required to validate the computationally modelled results. This should cover both the lattice sample elasticity testing under uniaxial compressive load and the testing of a manufactured porous femoral within a bovine femur. The development of a sophisticated multi-point method for measuring the average stress, and stress distribution in the femur will increase the accuracy of stress shielding calculations in future studies. The design of future porous stems will be enhanced by the development of an algorithm to generate irregular fully porous lattices that conform to the required geometry of the femoral stem while avoiding the formation of partial surface cells. Developing femoral stem designs with neck and head geometry that mimics a natural femur will aid in maintaining the pre-implantations stress distribution. The development of lattice types and topology optimisation techniques which optimise for maximum elasticity will further enhance future engineering lattices used in low elastic modulus biomedical applications.

References

Abu-Amer, Y, Darwech, I & Clohisy, JC 2007, 'Aseptic loosening of total joint replacements: mechanisms underlying osteolysis and potential therapies', *Arthritis Res Ther*, vol. 9 Suppl 1, no. Suppl 1, p. S6.

Alontseva, D, Azamatov, B, Safarova , Y, Voinarovych, S & Nazenova, G 2023, 'A Brief Review of Current Trends in the Additive Manufacturing of Orthopedic Implants with Thermal Plasma-Sprayed Coatings to Improve the Implant Surface Biocompatibility', *Coatings*, vol. 13, no. 7, p. 1175.

Arabnejad, S, Johnston, B, Tanzer, M & Pasini, D 2017, 'Fully porous 3D printed titanium femoral stem to reduce stress-shielding following total hip arthroplasty', *Journal of Orthopaedic Research*, vol. 35, no. 8, pp. 1774-83.

Bazyar, P, Baumgart, A, Altenbach, H & Usbeck, A 2023, 'An Overview of Selected Material Properties in Finite Element Modeling of the Human Femur', *Biomechanics*, vol. 3, no. 1, pp. 124-35.

Bishop, NE, Waldow, F & Morlock, MM 2008, 'Friction moments of large metal-on-metal hip joint bearings and other modern designs', *Medical Engineering & Physics*, vol. 30, no. 8, pp. 1057-64.

Bliss, O, Swadener, JG, Pearce, G & F. Zidane, I 2023, 'Finite element analysis of a stemmed hip prosthesis to reduce stress shielding in the proximal femur', *JOURNAL OF MECHANICAL ENGINEERING AND SCIENCES*.

Boccaccini, A, R & Fan, Z 1997, 'A new approach for the Young's modulus-porosity correlation of ceramic materials', *Ceramics International*, vol. 23, no. 3, pp. 239-45.

Chi, WM, Lin, CC, Ho, YJ, Lin, HC & Chen, JH 2018, 'Using nonlinear finite element models to analyse stress distribution during subluxation and torque required for dislocation of newly developed total hip structure after prosthetic impingement', *Med Biol Eng Comput*, vol. 56, no. 1, pp. 37-47.

Cilla, M, Checa, S & Duda, GN 2017, 'Strain shielding inspired re-design of proximal femoral stems for total hip arthroplasty', *Journal of Orthopaedic Research*, vol. 35, no. 11, pp. 2534-44.

Corona-Castuera, J, Rodriguez-Delgado, D, Henao, J, Castro-Sandoval, JC & Poblano-Salas, CA 2021, 'Design and Fabrication of a Customized Partial Hip Prosthesis Employing CT-Scan Data and Lattice Porous Structures', *ACS Omega*, vol. 6, no. 10, pp. 6902-13.

Crosby, K 2013, 'Titanium-6Aluminum-4Vanadium For Functionally Graded Orthopedic Implant Applications'.

D'Amore, A & Grassia, L 2019, 'Principal Features of Fatigue and Residual Strength of Composite Materials Subjected to Constant Amplitude (CA) Loading', *Materials (Basel)*, vol. 12, no. 16.

de Waard, S, van der Vis, J, Venema, P, Sierevelt, IN, Kerkhoffs, G & Haverkamp, D 2021, 'Short-term success of proximal bone stock preservation in short hip stems: a systematic review of the literature', *EFORT Open Rev*, vol. 6, no. 11, pp. 1040-51.

Eldesouky, I, El-Hofy, H & Harrysson, O 2017, 'Research: Design and Analysis of a Low-Stiffness Porous Hip Stem', *Biomed Instrum Technol*, vol. 51, no. 6, pp. 474-82.

Eldesouky, I, Harrysson, O, Marcellin-Little, DJ, West, H & El-Hofy, H 2017, 'Pre-clinical evaluation of the mechanical properties of a low-stiffness cement-injectable hip stem', *J Med Eng Technol*, vol. 41, no. 8, pp. 681-91.

Emara, AK, Ng, M, Krebs, VE, Bloomfield, M, Molloy, RM & Piuzzi, NS 2021, 'Femoral Stem Cementation in Hip Arthroplasty: The Know-How of a "Lost" Art', *Curr Rev Musculoskelet Med*, vol. 14, no. 1, pp. 47-59.

Eschweiler, J, Fieten, L, Dell'anna, J, Kabir, K, Gravius, S, Tingart, M & Radermacher, K 2012, 'Application and evaluation of biomechanical models and scores for the planning of total hip arthroplasty', *Proceedings of the Institution of Mechanical Engineers. Part H, Journal of engineering in medicine*, vol. 226, pp. 955-67.

Evans, JT, Evans, JP, Walker, RW, Blom, AW, Whitehouse, MR & Sayers, A 2019, 'How long does a hip replacement last? A systematic review and meta-analysis of case series and national registry reports with more than 15 years of follow-up', *The Lancet*, vol. 393, no. 10172, pp. 647-54.

Fraldi, M, Esposito, L, Perrella, G, Cutolo, A & Cowin, S 2010, 'Topological optimization in hip prosthesis design', *Biomechanics and modeling in mechanobiology*, vol. 9, pp. 389-402.

Hacking, C, Worsley, C & Nicoletti, D 2023, *Case 1, Total hip arthroplasty* viewed 05 Oct 2024, <.

Havaldar, R, Pilli, S & Putti, B 2014, 'Insights into the effects of tensile and compressive loadings on human femur bone', *Advanced biomedical research*, vol. 3, p. 101.

He, Y, Burkhalter, D, Durocher, D & Gilbert, JM 2018, 'Solid-Lattice Hip Prosthesis Design: Applying Topology and Lattice Optimization to Reduce Stress Shielding From Hip Implants', *Proceedings of the*.

Hedayati, R & Fallah, M 2015, 'Effect of Window Geometry on Strength of Shaft Part of Femur Bone', *Periodica Polytechnica Mechanical Engineering*, vol. 59.

Hezil, N, Aissani, L, Fellah, M, Abdul Samad, M, Obrosov, A, Timofei, C & Marchenko, E 2022, 'Structural, and tribological properties of nanostructured α + β type titanium alloys for total hip', *Journal of Materials Research and Technology*, vol. 19, pp. 3568-78.

Jetté, B, Brailovski, V, Dumas, M, Simoneau, C & Terriault, P 2018, 'Femoral stem incorporating a diamond cubic lattice structure: Design, manufacture and testing', *Journal of the Mechanical Behavior of Biomedical Materials*, vol. 77, pp. 58-72.

Jones, A 2008, 'Micro-Computed Tomography Studies of Biomaterials and Bone', Australian National University.

Katz, Y, Yosibash, Z, Salai, M & Snir, N 2020, 'Strain shielding for cemented hip implants', *Clinical Biomechanics*, vol. 77, p. 105027.

Kharmanda, G 2016, 'Integration of multi-objective structural optimization into cementless hip prosthesis design: Improved Austin-Moore model', *Computer Methods in Biomechanics and Biomedical Engineering*, vol. 19, no. 14, pp. 1557-66.

Kinkel, S, Wollmerstedt, N, Kleinhans, JA, Hendrich, C & Heisel, C 2009, 'Patient activity after total hip arthroplasty declines with advancing age', *Clin Orthop Relat Res*, vol. 467, no. 8, pp. 2053-8.

Kováčik, J 1999, 'Correlation between Young's Modulus and Porosity in Porous Materials', *Journal of Materials Science Letters*, vol. 18, pp. 1007-10.

Kyocera 2024, *Kyocera A400 Standard Hip Stem Sizes and Specs*, KYOCERA Medical Technologies, Inc. All rights reserved, viewed 03/06/2024, <.

Lehil, MS & Bozic, KJ 2014, 'Trends in Total Hip Arthroplasty Implant Utilization in the United States', *The Journal of Arthroplasty*, vol. 29, no. 10, pp. 1915-8.

Limmahakhun, S, Oloyede, A, Sitthiseripratip, K, Xiao, Y & Yan, C 2017, 'Stiffness and strength tailoring of cobalt chromium graded cellular structures for stress-shielding reduction', *Materials & Design*, vol. 114, pp. 633-41.

Liu, B, Wang, H, Zhang, N, Zhang, M & Cheng, CK 2021, 'Femoral Stems With Porous Lattice Structures: A Review', *Front Bioeng Biotechnol*, vol. 9, p. 772539.

Lu, J & Chen, Y 2013, 'Topology optimisation and customisation of a prosthetic knee joint design', *International Journal of Computer Integrated Manufacturing*, vol. 26, no. 10, pp. 968-76.

Markatos, K, Savvidou, OD, Foteinou, A, Kosmadaki, S, Trikoupis, I, Goumenos, SD & Papagelopoulos, PJ 2020, 'Hallmarks in the History and Development of Total Hip Arthroplasty', *Surgical Innovation*, vol. 27, no. 6, pp. 691-4.

MatWeb 2024, *Titanium Ti-6Al-4V (Grade 5), STA Datasheet*, MatWeb Material Property Data, viewed 07/05/2024, <https://www.matweb.com/search/DataSheet.aspx?MatGUID=b350a789eda946c6b86a3e4d3c577b39&ckck=1>.

Mehboob, H, Tarlochan, F, Mehboob, A & Chang, S-H 2018, 'Finite element modelling and characterization of 3D cellular microstructures for the design of a cementless biomimetic porous hip stem', *Materials & Design*, vol. 149, pp. 101-12.

Mehboob, H, Tarlochan, F, Mehboob, A, Chang, S-H, Ramesh, S, Harun, WSW & Kadirgama, K 2020, 'A novel design, analysis and 3D printing of Ti-6Al-4V alloy bio-inspired porous femoral stem', *Journal of Materials Science: Materials in Medicine*, vol. 31, no. 9, p. 78.

Mendiolagoitia, L, Rodríguez, M, Crespo, I, Del Valle, M & Olmedillas, H 2020, 'Kinematic Gait Analysis After Primary Total Hip Replacement: A Systematic Review: Gait After Total Hip Replacement: A Systematic Review', *Indian J Orthop*, vol. 54, no. 6, pp. 767-75.

O'Dwyer Lancaster-Jones, O & Reddiough, R 2023, 'The occurrence of squeaking under wear testing standards for ceramic on ceramic total hip replacements', *Journal of the Mechanical Behavior of Biomedical Materials*, vol. 138, p. 105616.

Oltean-Dan, D, Apostu, D, Tomoaia, G, Kerekes, K, Păiuşan, MG, Bardas, CA & Benea, HRC 2022, 'Causes of revision after total hip arthroplasty in an orthopedics and traumatology regional center', *Med Pharm Rep*, vol. 95, no. 2, pp. 179-84.

Patel, I, Nham, F, Zalikha, AK & El-Othmani, MM 2023, 'Epidemiology of total hip arthroplasty: demographics, comorbidities and outcomes', *Arthroplasty*, vol. 5, no. 1, p. 2.

Paulsen, RT, Revald, PH, Kjærsgaard-Andersen, P, Timm, S & Varnum, C 2024, 'Ceramic-on-Ceramic Total Hip Arthroplasty and Noises: A Prospective Blinded Randomized Controlled Trial of Influence of Component Design', *The Journal of Arthroplasty*, vol. 39, no. 3, pp. 734-8.

Petis, S, Howard, JL, Lanting, BL & Vasarhelyi, EM 2015, 'Surgical approach in primary total hip arthroplasty: anatomy, technique and clinical outcomes', *Can J Surg*, vol. 58, no. 2, pp. 128-39.

Puijk, R, Rassir, R, Sierevelt, IN, Spekenbrink-Spooren, A, Nelissen, RGHH & Nolte, PA 2023, 'Association Between Surface Modifications for Biologic Fixation and Aseptic Loosening of Uncemented Total Knee Arthroplasties', *The Journal of Arthroplasty*, vol. 38, no. 12, pp. 2605-11.e1.

Rahaman, MN, Yao, A, Bal, BS, Garino, JP & Ries, MD 2007, 'Ceramics for Prosthetic Hip and Knee Joint Replacement', *Journal of the American Ceramic Society*, vol. 90, no. 7, pp. 1965-88.

Rotta, G, Seramak, T & Zasińska, K 2015, 'Estimation of Young's Modulus of the Porous Titanium Alloy with the Use of Fem Package', *Advances in Materials Science*, vol. 15.

Shanmugaraj, A, Kumar, MV, Al Naji, O, Simunovic, N, Philippon, MJ & Ayeni, OR 2023, 'Hip Arthroscopy Improves Outcomes With Moderate Conversion to Total Hip Arthroplasty Rates in Patients Aged 50 Years or Older: A Systematic Review', *Arthroscopy: The Journal of Arthroscopic & Related Surgery*, vol. 39, no. 6, pp. 1539-51.e1.

Shanto, RA, Khalil, M, Sultana, SZ, Epsi, EZ, Bose, SK, Latif, MS, Siddiquee, T, Russel, MTH & Sumi, SA 2024, 'Variation of Mid shaft Antero-posterior and Transverse Diameter of Femur in Bangladeshi People', *Mymensingh Med J*, vol. 33, no. 1, pp. 234-8.

Sheridan, G, Hughes, H, Welch-Phillips, A, Kenny, P, O'Toole, G & O'Byrne, J 2021, 'The varus cemented femoral stem in total hip arthroplasty: Predictors, implications and The Femoral Access Ratio', *J Orthop*, vol. 23, pp. 8-12.

Singh, SK & Tandon, P 2018, 'Heterogeneous modeling based prosthesis design with porosity and material variation', *Journal of the Mechanical Behavior of Biomedical Materials*, vol. 87, pp. 124-31.

Stewart, C, Akhavan, B, Wise, SG & Bilek, MMM 2019, 'A review of biomimetic surface functionalization for bone-integrating orthopedic implants: Mechanisms, current approaches, and future directions', *Progress in Materials Science*, vol. 106, p. 100588.

Tan, N & van Arkel, RJ 2021, 'Topology Optimisation for Compliant Hip Implant Design and Reduced Strain Shielding', *Materials (Basel)*, vol. 14, no. 23.

Vickers, OG, Culmer, PR, Isaac, GH, Kay, RW, Shuttleworth, MP, Board, T & Williams, S 2021, 'Is in vivo sensing in a total hip replacement a possibility? A review on past systems and future challenges', *Progress in Biomedical Engineering*, vol. 3, no. 4, p. 042004.

Wang, C, Xu, D, Lin, L, Li, S, Hou, W, He, Y, Sheng, L, Yi, C, Zhang, X, Li, H, Li, Y, Zhao, W & Yu, D 2021, 'Large-pore-size Ti6Al4V scaffolds with different pore structures for vascularized bone regeneration', *Materials Science and Engineering: C*, vol. 131, p. 112499.

Wang, X-h, Li, J-s, Hu, R, Kou, H-c & Zhou, L 2013, 'Mechanical properties of porous titanium with different distributions of pore size', *Transactions of Nonferrous Metals Society of China*, vol. 23, no. 8, pp. 2317-22.

Wendler, T, Edel, M, Möbius, R, Fakler, J, Osterhoff, G & Zajonz, D 2022, 'Fixation of intraoperative proximal femoral fractures during THA using two versus three cerclage wires - a biomechanical study', *BMC Musculoskeletal Disorders*, vol. 23, no. 1, p. 40.

Yang, L, Han, C, Wu, H, Hao, L, Wei, Q, Yan, C & Shi, Y 2020, 'Insights into unit cell size effect on mechanical responses and energy absorption capability of titanium graded porous structures manufactured by laser powder bed fusion', *Journal of the Mechanical Behavior of Biomedical Materials*, vol. 109, p. 103843.

Zhang, J, Shen, Y, Sun, Y, Yang, J, Gong, Y, Wang, K, Zhang, Z, Chen, X & Bai, L 2022, 'Design and mechanical testing of porous lattice structure with independent adjustment of pore size and porosity for bone implant', *Journal of Materials Research and Technology*, vol. 18, pp. 3240-55.

Zhang, Y, Sun, N, Zhu, M, Qiu, Q, Zhao, P, Zheng, C, Bai, Q, Zeng, Q & Lu, T 2022, 'The contribution of pore size and porosity of 3D printed porous titanium scaffolds to osteogenesis', *Biomaterials Advances*, vol. 133, p. 112651.

`

APPENDIX A – Working Spreadsheet

The following spreadsheet contains all raw data recorded from the model and FEA, as well as all calculations carried out for analysis of the data. The cells highlighted in green contain raw input data. The cells highlighted in blue contain the output data presented in the body of this report. The cells highlighted in purple present relative error rates between output data variables. All unhighlighted cells contain intermediate steps for calculation or were part of redundant analysis that was not used in the final report.

pressure applied (Pa)	4.00E+06
cell size (mm)	0.50
E solid	1.14E+11

Square unit cell	1																													
strut thickness	Pore size	V_total	V_model	porosity	A_ave	A_cell*(1-p)	A upper	F applied	VM stress (Pa)			YY Stress (P	Compressive stress analytical (Pa)				Strain					rigional lengt	change in length			E effective (Pa)					
(mm)	(mm)	(mm^3)	(mm^3)		mm^2	mm^2	mm^2	N	min	max	ave	Max	compres_ave	error % VM	compres_1-p	error % YY	min abs	max abs	ave	anal	error %	Lo (mm)	min (mm)	max (mm)	ave (mm)	model	Anal	Solid*pou	K (%)	K anal (%)	theoro (%
0.1667	0.3333	0.2963	0.1482	0.4999	0.2223	0.2223	0.3334	1.3336	1.55E+05	3.40E+07	1.71E+07	6.55E+06	6.00E+06	184.65	6.00E+06	9.18	2.94E-04	3.13E-05	1.63E-04	1.02E-04	60.3	0.667	1.03E-04	3.28E-05	6.77E-05	1.05E+11	5.91E+10	5.70E+10	-8.02	-48.19	-49.99
0.1381	0.3619	0.2598	0.1039	0.6001	0.1628	0.1628	0.2762	1.1048	1.81E+06	4.52E+07	2.35E+07	1.12E+07	6.79E+06	246.23	6.79E+06	64.63	9.31E-05	3.94E-04	2.43E-04	1.38E-04	76.6	0.638	1.44E-04	3.16E-05	8.80E-05	9.65E+10	4.92E+10	4.56E+10	-15.36	-56.83	-60.01
0.1110	0.3890	0.2281	0.0685	0.6997	0.1120	0.1121	0.222	0.888	1.78E+05	6.63E+07	3.32E+07	2.27E+07	7.93E+06	319.40	7.92E+06	186.59	5.80E-04	2.06E-04	3.93E-04	2.05E-04	92.1	0.611	2.23E-04	2.69E-05	1.25E-04	8.46E+10	3.87E+10	3.42E+10	-25.78	-66.03	-69.97
0.0838	0.4162	0.1990	0.0398	0.8000	0.0681	0.0682	0.1676	0.6704	1.57E+05	1.11E+08	5.53E+07	5.23E+07	9.84E+06	462.45	9.83E+06	431.85	9.76E-04	4.54E-04	7.15E-04	3.65E-04	95.8	0.584	4.16E-04	1.09E-05	2.13E-04	7.74E+10	2.69E+10	2.28E+10	-32.12	-76.38	-80.00
0.0543	0.4457	0.1703	0.0171	0.8996	0.0308	0.0308	0.1086	0.4344	4.67E+05	2.24E+08	1.12E+08	1.21E+08	1.41E+07	693.19	1.41E+07	759.30	1.94E-03	1.24E-03	1.59E-03	1.16E-03	37.4	0.554	6.23E-05	1.22E-03	6.41E-04	7.05E+10	1.22E+10	1.14E+10	-38.16	-89.32	-89.96

Square lattice	4																													
strut thickness	Pore size	V_total	V_model	porosity	A_ave	A_cell*(1-p)	A upper	F applied	VM stress (Pa)			YY Stress (P	Compressive stress analytical (Pa)				Strain					rigional lengt	change in length			E effective (Pa)					
(mm)	(mm)	(mm^3)	(mm^3)		mm^2	mm^2	mm^2	N	min	max	ave	Max	compres_ave	error % VM	compres_1-p	error % YY	min abs	max abs	ave	anal	error %	Lo (mm)	min (mm)	max (mm)	ave (mm)	model	Anal	Solid*pou	K (%)	K anal (%)	theoro (%
0.1667	0.3333	10.1718	3.35766	0.6699	1.5497	1.5497	2.91717	11.66868	7.90E+04	3.63E+07	1.82E+07	5.72E+06	7.53E+06	141.83	7.53E+06	24.04	5.20E-05	3.18E-04	1.85E-04	1.20E-04	54.6	2.167	3.23E-04	1.96E-04	2.60E-04	9.84E+10	6.29E+10	3.76E+10	-13.72	-44.85	-66.99
0.1381	0.3619	9.7743	2.3998	0.7545	1.1224	1.1224	2.4759	9.9036	1.08E+05	4.87E+07	2.44E+07	9.57E+06	8.82E+06	176.38	8.82E+06	8.44	4.32E-04	8.60E-05	2.59E-04	1.50E-04	72.8	2.138	2.24E-04	4.18E-04	3.21E-04	9.41E+10	5.88E+10	2.80E+10	-17.48	-48.41	-75.45
0.1110	0.3890	9.4073	1.6088	0.8290	0.7621	0.7621	2.03518	8.14072	8.12E+04	6.52E+07	3.26E+07	2.12E+07	1.07E+07	205.38	1.07E+07	98.47	5.73E-04	1.91E-04	3.82E-04	1.95E-04	95.9	2.111	2.65E-04	5.58E-04	4.12E-04	8.54E+10	5.48E+10	1.95E+10	-25.08	-51.93	-82.90
0.0838	0.4162	9.0483	0.95038	0.8950	0.4561	0.4561	1.57066	6.28264	8.80E-04	1.03E+08	5.14E+07	4.65E+07	1.38E+07	273.13	1.38E+07	237.78	8.99E-04	4.08E-04	6.54E-04	2.23E-04	193.5	2.084	2.96E-04	6.32E-04	4.64E-04	7.87E+10	6.19E+10	1.20E+10	-31.01	-45.72	-89.50
0.0543	0.4457	8.6695	0.41425	0.9522	0.2017	0.2017	1.0417	4.1668	5.63E+04	2.05E+08	1.03E+08	1.22E+08	2.07E+07	396.19	2.07E+07	489.44	1.15E-03	1.79E-03	1.47E-03	5.03E-04	192.5	2.054	1.69E-03	3.83E-04	1.03E-03	6.97E+10	4.11E+10	5.45E+09	-38.90	-63.98	-95.22

Square lattice	8 **excluding** top layer																													
strut thickness	Pore size	V_total	V_model	porosity	A_ave	A_cell*(1-p)	A upper	F applied	VM stress (Pa)			YY Stress (P	Compressive stress analytical (Pa)				Strain					rigional lengt	change in length			E effective (Pa)					
(mm)	(mm)	(mm^3)	(mm^3)		mm^2	mm^2	mm^2	N	min	max	ave	Max	compres_ave	error % VM	compres_1-p	error % YY	min abs	max abs	ave	anal	error %	Lo (mm)	min (mm)	max (mm)	ave (mm)	model	Anal	Solid*pou	K (%)	K anal (%)	theoro (%
0.2500	0.2500	76.7656	41.76	0.4560	9.8272	9.8259	14.06	56.24	4.80E+05	2.04E+07	1.04E+07	5.61E+06	5.72E+06	82.60	5.72E+06	1.94	1.62E-04	2.43E-05	9.33E-05	7.63E-05	22.4	4.250	3.55E-04	2.94E-04	3.24E-04	1.12E+11	7.50E+10	6.20E+10	-1.80	-34.18	-45.60
0.2200	0.2800	75.1514	34.1	0.5462	8.0823	8.0806	12.79	51.16	2.21E+05	2.06E+07	1.04E+07	5.93E+06	6.33E+06	64.47	6.33E+06	6.38	1.66E-04	2.09E-05	9.34E-05	9.09E-05	2.8	4.220	3.39E-04	4.28E-04	3.84E-04	1.11E+11	6.96E+10	5.17E+10	-2.26	-38.92	-54.62
0.1800	0.3200	73.0346	24.4	0.6659	5.8390	5.8373	10.92	43.68	1.96E+05	2.68E+07	1.35E+07	6.81E+06	7.48E+06	80.44	7.48E+06	8.96	1.96E-04	4.37E-05	1.20E-04	1.18E-04	1.3	4.180	5.69E-04	4.20E-04	4.94E-04	1.13E+11	6.33E+10	3.81E+10	-1.17	-44.48	-66.59
0.1400	0.3600	70.9579	15.717	0.7785	3.7964	3.7964	8.295	33.18	8.36E+04	2.64E+07	1.32E+07	8.89E+06	8.74E+06	51.51	8.74E+06	1.73	2.52E-04	5.70E-05	1.55E-04	1.75E-04	11.8	4.140	8.75E-04	5.75E-04	7.25E-04	8.57E+10	4.99E+10	2.53E+10	-24.82	-56.21	-77.85
0.1000	0.4000	68.9210	8.505	0.8766	2.0744	2.0744	6.57	26.28	1.14E+05	2.87E+07	1.44E+07	1.24E+07	1.27E+07	13.56	1.27E+07	2.12	1.55E-04	3.30E-04	2.42E-04	2.42E-04	0.1	4.100	1.15E-03	8.35E-04	9.93E-04	5.94E+10	5.23E+10	1.41E+10	-47.89	-54.09	-87.66

Square lattice	8 **including** top layerdefault mesh																Strain YY			Strain L/dL			
strut thickness	Pore size	V_total	V_model	porosity	A_ave	VM stress (Pa)			stress (Pa)		Strain YY					Origional	change in length					normal	Normal
(mm)	(mm)	(mm^3)	(mm^3)		m^2	min	max	ave	anal	error	min abs	max abs	ave	anal	error %	length Lo	min (mm)	max (mm)	ave (mm)	VM E (Pa)	VM K (%)	E (Pa)	K (%)
0.25	0.2500	76.7656	41.76	0.4560	9.83E-06	1.23E+05	2.39E+07	1.20E+07	5.72E+06	1.10	1.80E-04	3.06E-05	1.05E-04	7.63E-05	38.0	4.2500	3.55E-04	2.94E-04	3.24E-04	1.14E+11	0.14	7.50E+10	-34.18
0.22	0.2800	75.1514	34.1	0.5462	8.08E-06	6.06E+04	2.49E+07	1.25E+07	6.33E+06	0.97	1.93E-04	3.90E-05	1.16E-04	9.09E-05	27.3	4.2200	3.39E-04	4.28E-04	3.84E-04	1.08E+11	-5.36	6.96E+10	-38.92
0.18	0.3200	73.0346	24.4	0.6659	5.84E-06	8.09E+04	3.29E+07	1.65E+07	7.48E+06	1.20	2.23E-04	5.01E-05	1.37E-04	1.18E-04	15.7	4.1800	5.69E-04	4.20E-04	4.94E-04	1.20E+11	5.66	6.33E+10	-44.48
0.13	0.3700	70.4450	13.75	0.8048	3.33E-06	4.62E+04	5.32E+07	2.66E+07	9.97E+06	1.67	3.80E-04	1.16E-04	2.48E-04	1.76E-04	41.4	4.1300	8.75E-04	5.75E-04	7.25E-04	1.07E+11	-5.91	5.68E+10	-50.19
0.08	0.4200	67.9173	5.5987	0.9176	1.37E-06	1.17E+05	9.12E+07	4.57E+07	1.92E+07	1.38	7.97E-04	4.79E-04	6.38E-04	2.43E-04	162.2	4.0800	1.15E-03	8.35E-04	9.93E-04	7.16E+10	-37.21	7.87E+10	-30.94

Square lattice	8 excluding top layer																						
strut thickness	Pore size	V_total	V_model	porosity	A_ave	VM stress (Pa)			stress (Pa)		Strain YY					length Lo	change in length					normal	Normal
(mm)	(mm)	(mm^3)	(mm^3)		m^2	min	max	ave	anal	error	min abs	max abs	ave	anal	error %	(mm)	min (mm)	max (mm)	ave (mm)	VM E (Pa)	VM K (%)	E (Pa)	K (%)
0.25	0.2500	76.7656	41.76	0.4560	9.83E-06	4.80E+05	2.04E+07	1.04E+07	5.72E+06	82.57	1.62E-04	2.43E-05	9.33E-05	7.63E-05	22.4	4.2500	3.55E-04	2.94E-04	3.24E-04	1.12E+11	-1.80	7.50E+10	-34.18
0.22	0.2800	75.1514	34.1	0.5462	8.08E-06	2.21E+05	2.06E+07	1.04E+07	6.33E+06	64.43	1.66E-04	2.09E-05	9.34E-05	9.09E-05	2.8	4.2200	3.39E-04	4.28E-04	3.84E-04	1.11E+11	-2.26	6.96E+10	-38.92
0.18	0.3200	73.0346	24.4	0.6659	5.84E-06	1.96E+05	2.68E+07	1.35E+07	7.48E+06	80.38	1.96E-04	4.37E-05	1.20E-04	1.18E-04	1.3	4.1800	5.69E-04	4.20E-04	4.94E-04	1.13E+11	-1.17	6.33E+10	-44.48
0.14	0.3600	70.9579	15.717	0.7785	3.80E-06	8.36E+04	2.64E+07	1.32E+07	8.74E+06	51.51	2.52E-04	5.70E-05	1.55E-04	1.75E-04	11.8	4.1400	8.75E-04	5.75E-04	7.25E-04	8.57E+10	-24.82	4.99E+10	-56.21
0.10	0.4000	68.9210	8.505	0.8766	2.07E-06	1.14E+05	2.87E+07	1.44E+07	1.27E+07	13.56	1.55E-04	3.30E-04	2.42E-04	2.42E-04	0.1	4.1000	1.15E-03	8.35E-04	9.93E-04	5.94E+10	-47.89	5.23E+10	-54.09

$$A_{ave} \approx A_{total}(1-\varphi)$$

F (N) = 25

Hexagonal	4																						
strut thickness	Pore size	V_total	V_model	porosity	A_ave	VM stress (MPa)			stress (Pa)		Strain Max Principal					Origional	change in length					normal	Normal
(mm)	(mm)	(mm^3)	(mm^3)		m^2	min	max	ave	anal	error %	min abs	max abs	ave	anal	error %	length Lo	min (mm)	max (mm)	ave (mm)	VM E (Pa)	VM K (%)	E (Pa)	K (%)
0.30	0.7000	64.0000	25.3	0.6047	6.33E-06	0.04	41.80	20.92	3.95E+06	429.21	5.26E-06	3.81E-04	1.93E-04	8.13E-05	137.7	4.0000	3.60E-04	2.90E-04	3.25E-04	1.08E+11	-4.99	4.86E+10	-57.33
0.20	0.8000	64.0000	13.2	0.7938	3.30E-06	0.07	136.10	68.08	7.58E+06	798.72	1.54E-05	1.33E-03	6.73E-04	3.19E-04	110.7	4.0000	1.50E-03	1.05E-03	1.28E-03	1.01E+11	-11.22	2.37E+10	-79.18
0.16	0.8400	64.0000	8.945	0.8602	2.24E-06	0.15	351.80	175.97	1.12E+07	1474.08	2.67E-03	1.03E-03	1.85E-03	7.57E-04	144.3	4.0000	2.46E-03	3.60E-03	3.03E-03	9.51E+10	-16.56	1.48E+10	-87.05
0.12	0.8800	64.0000	5.305	0.9171	1.33E-06	0.22	844.00	422.11	1.89E+07	2139.28	7.33E-03	2.59E-03	4.96E-03	2.34E-03	112.1	4.0000	1.12E-02	7.56E-03	9.36E-03	8.51E+10	-25.35	8.06E+09	-92.93
0.10	0.9000	64.0000	3.78	0.9409	9.45E-07	0.23	1292.00	646.12	2.65E+07	2342.32	1.27E-02	3.71E-03	8.19E-03	5.16E-03	58.7	4.0000	2.52E-02	1.61E-02	2.06E-02	7.89E+10	-30.76	5.13E+09	-95.50

Diamond	4																						
strut thickness	Pore size	V_total	V_model	porosity	A_ave	VM stress (MPa)			stress (Pa)		Strain Max Principal					Origional	change in length					normal	Normal
(mm)	(mm)	(mm^3)	(mm^3)		m^2	min	max	ave	anal	error %	min abs	max abs	ave	anal	error %	length Lo	min (mm)	max (mm)	ave (mm)	VM E (Pa)	VM K (%)	E (Pa)	K (%)
0.25	0.6464	64.0000	33.997	0.4688	8.50E-06	0.23	19.86	10.04	2.94E+06	241.47	1.64E-04	3.01E-05	9.71E-05	6.16E-05	57.6	4.0000	2.44E-04	2.49E-04	2.46E-04	1.03E+11	-9.22	4.78E+10	-58.10
0.20	0.7172	64.0000	24.232	0.6214	6.06E-06	0.31	34.15	17.23	4.13E+06	317.54	2.82E-04	4.27E-05	1.62E-04	1.17E-04	38.2	4.0000	4.61E-04	4.78E-04	4.70E-04	1.06E+11	-6.90	3.51E+10	-69.18
0.15	0.7878	64.0000	15.02	0.7653	3.76E-06	0.23	49.34	24.79	6.66E+06	272.29	4.22E-04	7.34E-05	2.48E-04	2.64E-04	6.3	4.0000	1.00E-03	1.11E-03	1.06E-03	1.00E+11	-12.22	2.52E+10	-77.90
0.12	0.8303	64.0000	10.148	0.8414	2.54E-06	0.17	89.42	44.79	9.85E+06	354.58	7.74E-04	1.88E-04	4.81E-04	4.28E-04	12.5	4.0000	1.71E-03	1.82E+00	1.71E-03	9.32E+10	-18.28	2.31E+10	-79.78
0.10	0.8585	64.0000	7.295	0.8860	1.82E-06	0.13	124.90	62.51	1.37E+07	356.03	1.15E-03	2.83E-04	7.14E-04	9.37E-04	23.8	4.0000	3.70E-03	3.80E-03	3.75E-03	8.76E+10	-23.19	1.46E+10	-87.17

Stress Shielding

		zone 1				zone 2				zone 3				zone 4				zone 5				zone 6				zone 7		
	min	max	Ave	SS	min	max	Ave	SS	min	max	Ave	SS	min	max	Ave	SS	min	max	Ave	SS	min	max	Ave	SS	min	max	Ave	SS
Intact	0.372	3.692	2.032	0.000	4.569	9.605	7.087	0.000	4.128	10.500	7.314	0.000	0.635	15.351	7.993	0.000	14.070	7.145	10.608	0.000	13.070	7.623	10.347	0.000	0.399	21.310	10.855	0.000
Solid	0.169	1.039	0.604	70.272	1.269	2.295	1.782	74.855	0.370	1.557	0.964	86.827	6.216	1.216	3.716	53.509	1.332	1.511	1.422	86.599	2.409	4.093	3.251	68.579	0.231	5.277	2.754	74.628
Hex	13.260	0.051	6.656	-227.545	2.496	11.100	6.798	4.078	9.895	3.168	6.532	10.699	0.311	15.600	7.956	0.469	7.313	13.760	10.537	0.669	5.479	17.196	11.338	-9.578	30.510	0.723	15.617	-43.869
Square	0.270	26.000	13.135	-546.423	0.220	5.755	2.988	57.845	1.860	5.821	3.841	47.491	7.626	0.407	4.017	49.750	4.013	0.452	2.232	78.955	3.005	11.850	7.428	28.212	0.422	24.300	12.361	-13.877
Diamond	0.230	13.910	7.070	-247.929	2.930	10.120	6.525	7.930	2.298	11.000	6.649	9.092	0.831	15.820	8.326	-4.160	11.470	7.189	9.330	12.048	16.820	6.856	11.838	-14.416	27.300	0.258	13.779	-26.940

WITH surface cell layer

	min	max	alt stress	mean
Solid	0.00075	56.99	28.493625	28.4943755
Hex	0.00271	809.20	404.59865	404.601355
Square	0.00191	681.00	340.49904	340.500957
Diamond	0.00183	3918.00	1958.9991	1959.00092

move 1mm from stress concentration point

		zone 1				zone 2				zone 3				zone 4				zone 5				zone 6				zone 7		
	min	max	Ave	SS	min	max	Ave	SS	min	max	Ave	SS	min	max	Ave	SS	min	max	Ave	SS	min	max	Ave	SS	min	max	Ave	SS
Intact	0.372	3.692	2.032	0.000	4.569	9.605	7.087	0.000	4.128	10.500	7.314	0.000	0.635	15.351	7.993	0.000	14.070	7.145	10.608	0.000	13.070	7.623	10.347	0.000	0.399	21.310	10.855	0.000
Solid	0.169	1.039	0.604	70.272	1.269	2.295	1.782	74.855	0.370	1.557	0.964	86.827	6.216	1.216	3.716	53.509	1.332	1.511	1.422	86.599	2.409	4.093	3.251	68.579	0.231	5.277	2.754	74.628
Hex	0.051	3.907	1.979	2.603	2.496	11.100	6.798	4.078	9.895	3.168	6.532	10.699	0.311	15.600	7.956	0.469	7.313	13.760	10.537	0.669	5.479	17.196	11.338	-9.578	0.723	15.950	8.337	23.199
Square	0.270	4.451	2.361	-16.169	0.220	5.755	2.988	57.845	1.860	5.821	3.841	47.491	7.626	0.407	4.017	49.750	4.013	0.452	2.232	78.955	3.005	11.850	7.428	28.212	0.422	13.100	6.761	37.713
Diamond	0.230	5.124	2.677	-31.733	2.930	10.120	6.525	7.930	2.298	11.000	6.649	9.092	0.831	15.820	8.326	-4.160	11.470	7.189	9.330	12.048	16.820	6.856	11.838	-14.416	0.258	18.920	9.589	11.660

q

WITHout surface cell layer

	min	max	alt stress	mean
Solid	0.00075	56.99	28.493625	28.4943755
Hex	0.00271	132.30	66.148645	66.151355
Square	0.00191	153.60	76.799043	76.800957
Diamond	0.00183	168.50	84.249085	84.250915

Rel change in comparable studies

E = 1.14E+11

source	p	E	rel_change
ELDa	57	9.27E+09	-91.87
ELDa	64	4.74E+09	-95.84
Mehboob	89.6	4.86E+09	-95.74
	21.6	7.14E+10	-37.40

`

APPENDIX B – MATLAB Script

```
% 03/06/24 - 1934 the equation for v total is wrong
% 03/06/24 - 1946 the equation for As total is also wrong
```

Here we are calculating the loading conditions for the cell, and sample.

```
m = 80;          % kg    mass used to calculate pressure
d = 25e-3;       % m     diameter of femur
g = 9.81;        % m/s^2 gravity

F = m*g          % N     Force on bone
A = pi*(d/2)^2   % m2    Area
P = F/A          % Pa    Pressure

number_of_cells = 8;
cell_size = 0.5e-3;
A_sample = (cell_size*number_of_cells)^2
F_sample = P*A_sample
```

Here I am analytically calculating the total volume and volume of the strut to compare against the model. I am varying the thickness of the strut t to change the porosity.

$$A_{\text{cell}} = (n+t)^2$$

$$V_{\text{cell}} = (n+t)^3$$

$$\varphi = \frac{V_{total} - V_s}{V_{total}}$$

```
% this is all in mm and mm^3
n = 0.5;

t = 0.1667;  % thickness of wall mm to the +-1 um
V_total = (n + t)^3;
Vs = t^2*( 12*(n-t) + 8*t )
pour = (V_total-Vs)/V_total

t = 0.1381;  % thickness of wall mm to the +-1 um
V_total = (n + t)^3;
Vs = t^2*( 12*(n-t) + 8*t )
pour = (V_total-Vs)/V_total

t = 0.1110;  % thickness of wall mm to the +-1 um
V_total = (n + t)^3;
Vs = t^2*( 12*(n-t) + 8*t )
pour = (V_total-Vs)/V_total
```

```
t = 0.0838;  % thickness of wall mm to the +-1 um
V_total = (n + t)^3;
Vs = t^2*( 12*(n-t) + 8*t )
pour = (V_total-Vs)/V_total

t = 0.0543;  % thickness of wall mm to the +-1 um
V_total = (n + t)^3;
Vs = t^2*( 12*(n-t) + 8*t )
pour = (V_total-Vs)/V_total

syms t n pour
V_total = (n + t)^3;
Vs = t^2*( 12*(n-t) + 8*t );
pour = (V_total-Vs)/V_total
```

The analytical calcs match the volume of the model. the porosity at this step has been validated now we can move on to simulate.

$$A_{\text{cell}} = (n+t)^2$$

$$V_{\text{cell}} = (n+t)^3$$

```
a = (2*t) / (n+t)
b = (n-t) / (n+t)
A1 = (n+t)^2 - (n-t)^2
A2 = t^2
A_ave = A1*a + A2*b
```

Plotting porosity as a function of the number of cells

```
syms c n t
n = 0.5
t = 0.1667

for t = 0.05:0.05:0.2

V_total = (c*n + t)^3;

A1 = (c*n+t)^2 - (n-t)^2*c^2;
A2 = t^2*(c+1)^2;

V1 = A1*t;
V2 = A2*(n-t);

Vs = V1*(c+1) + V2*c

pour = (V_total-Vs)/V_total;
```

```
 hold on
 fplot(pour)
 xlim([0 10])
 end
 grid on
 xlabel('n')
 ylabel('Porosity')
 legend('t = 0.05 mm','t = 0.10 mm','t = 0.15 mm','t = 0.20
mm','Location','southeast')
 hold off
```

Calculating the required thickness to achieve a given porosity

```
 n = 100;
 c = 0.5;

 for pour = 0.5:0.1:0.9

 syms t
 V_total = (n*c + t)^3;
 A1 = (n*c+t)^2 - (c-t)^2*n^2;
 A2 = t^2*(n+1)^2;
 V1 = A1*t;
 V2 = A2*(c-t);
 Vs = V1*(n+1) + V2*n;

 eqn = pour == (V_total-Vs)/V_total;

 t = double(solve(eqn));
 t = t(t<0.5 & t>0)

 end
```

Calculating the average cross-sectional area of a square lattice

```
 syms t c n

 l_total = (n*c + t);
 A_total = l_total^2;
 l_pore = (c-t);
 A_pore = l_pore^2;

 A1 = A_total - A_pore*n^2;
 A2 = t^2*(n+1)^2;
```

```
A_ave = A1*t*(n+1)/l_total + A2*l_pore*n/l_total
```

Force and moment calculations for full stem and cross sections. (not used in final version)

```
F1 = 2.385e3; % applied resultant force
beta = 90-18.47 % angle from horizontal plane
Fx = -F1*cosd(beta)
Fy = -F1*sind(beta)

w = 4e-3; % width of slice
F1 = 2.385e3; % applied resultant force
beta = 90-18.47; % angle from horizontal plane

d = 50e-3; % diamater of cross section
F = F1*4*w/(pi*d) % adjusted resultant force
%fx_norm = cosd(beta-51.4)
%fy_norm = sind(beta-51.4)

Fx = -F*cosd(beta)
Fy = -F*sind(beta)
```

This section is plotting the measured relative change elastic modulus and calculating the line of best fit

```
p1 = [0.4560 0.5462 0.6659 0.7785 0.8766];
k1 = [0.98 0.98 0.99 0.75 0.52];

p2 = [0.6047 0.7938 0.8602 0.9171 0.9409];
k2 = [0.95 0.89 0.83 0.75 0.69];

p3 = [0.4688 0.6214 0.7653 0.8414 0.8860];
k3 = [0.91 0.93 0.88 0.82 0.77];

[xData1, yData1] = prepareCurveData( p1, k1 );

% Set up fittype and options.
ft1 = fittype( 'power2' );
opts1 = fitoptions( 'Method', 'NonlinearLeastSquares' );
opts1.Display = 'Off';
opts1.StartPoint = [0.712441430247708 -0.360729212387818
0.00725073328327437];
% Fit model to data.
[fitresult1, gof1] = fit( xData1, yData1, ft1, opts1 );

[xData2, yData2] = prepareCurveData( p2, k2 );

% Set up fittype and options.
ft2 = fittype( 'power2' );
```

```
 opts2 = fitoptions( 'Method', 'NonlinearLeastSquares' );
 opts2.Display = 'Off';
 opts2.StartPoint = [0.712441430247708 -0.360729212387818
0.00725073328327437];

 % Fit model to data.
 [fitresult2, gof2] = fit( xData2, yData2, ft2, opts2 );

 [xData3, yData3] = prepareCurveData( p3, k3 );

 % Set up fittype and options.
 ft3 = fittype( 'power2' );
 opts3 = fitoptions( 'Method', 'NonlinearLeastSquares' );
 opts3.Display = 'Off';
 opts3.StartPoint = [0.712441430247708 -0.360729212387818
0.00725073328327437];

 % Fit model to data.
 [fitresult3, gof3] = fit( xData3, yData3, ft3, opts3 );

 % Plot fit with data.
 figure( 'Name', 'untitled fit 1' );
 hold on
 plot(fitresult1, xData1, yData1);
 plot(fitresult2, xData2, yData2);
 plot(fitresult3, xData3, yData3);
 legend( 'a', 'aa','b', 'b', 'c', 'cc' );
 % Label axes
 xlabel( 'p1', 'Interpreter', 'none' );
 ylabel( 'k1', 'Interpreter', 'none' );
 grid on
 hold off
```

This section is plotting the Soderberg failure criteria graph.

```
 % MATLAB Script to plot a line in intercept form

 % Clear workspace and figures
 clear; clc; close all;

 % Prompt user for intercepts
 a = 1070/2; %input('Enter the x-intercept (a): ');
 b = 400/3; %input('Enter the y-intercept (b): ');

 % Define the x range for plotting
 x = linspace(-2*a, 2*a, 100);  % Generate 100 points between -2*a and 2*a

 % Calculate corresponding y values using the intercept form equation
 y = b * (1 - x/a);
```

```
% Create the plot
figure;
plot(x, y, 'b-', 'LineWidth', 1,'Color','k', 'DisplayName', 'Soderberg
line');  % Plot the line
hold on;

% Plot the intercepts
plot(28.4, 28.4, 'ro', 'MarkerSize', 8, 'DisplayName', 'Solid','Color','r');
plot(404, 404, 'ro', 'MarkerSize', 8, 'DisplayName',
'Hexagonal','Color','g');
plot(304, 304, 'ro', 'MarkerSize', 8, 'DisplayName', 'Square','Color','b');
plot(1959, 1959, 'ro', 'MarkerSize', 8, 'DisplayName',
'Diamond','Color','m');

plot(28.4, 28.4, 'x', 'MarkerSize', 8, 'DisplayName', 'Solid','Color','r');
plot(66, 66, 'x', 'MarkerSize', 8, 'DisplayName', 'Hexagolan','Color','g');
plot(76, 76, 'x', 'MarkerSize', 8, 'DisplayName', 'Square','Color','b');
plot(64, 64, 'x', 'MarkerSize', 8, 'DisplayName', 'Diamond','Color','m');

% Set the limits of the axes
xlim([0, 600]);
ylim([0, 500]);

% Add labels and title
xlabel('\sigma_m (MPa)');
ylabel('\sigma_a (MPa)');
title('Soderberg Failure Criteria');
grid on;
legend show;

% Hold off to prevent further plotting on the same figure
hold off;
```

In this section I am working out the analytical volume of a square lattice

```
syms t c n

V_total = (n*c + t)^3;

A1 = (n*c+t)^2 - (c-t)^2*n^2;
A2 = t^2*(n+1)^2;

V1 = A1*t;
V2 = A2*(c-t);

Vs = V1*(n+1) + V2*n
```

In this section I am working out the correction factor for the resultant applied force in the 2.5d representation

```
syms l w r A d

d = 31.6 % diamater mm

A1 = 1/4*pi*d^2  % Area of circular cross section mm
A2 = d*4  % Area of rectangular cross section mm

j = A2/A1 % correction factor
```

APPENDIX C – Risk Assessment

4681	RISK DESCRIPTION	STATUS	TREND	CURRENT	RESIDUAL
	ENP4111 - Design of Fully Porous Femoral Stem to Reduce the Occurrence of Stress Shielding in Total Hip Arthroplasty	Live		Very Low	Very Low

RISK OWNER	RISK IDENTIFIED ON	LAST REVIEWED ON	NEXT SCHEDULED REVIEW
Clay Twomey	13/05/2024	13/05/2024	13/05/2025

RISK FACTOR(S)	EXISTING CONTROL(S)	CURRENT	PROPOSED CONTROL(S)	TREATMENT OWNER	DUE DATE	RESIDUAL
Long periods of computer use will be required for this project, and may result in repetitive stress injuries or eye strain.	Control: An ergonomic desktop office setup is used, including keyboard, mouse, monitor, sit/stand desk, chair and anti-fatigue mat. Control: Regular breaks are taken to reduce eye strain and back strain	Very Low	No Control:			Very Low
Psychological stress may occur during the conduct of the research project	Control: A well-designed project timeline, time management strategies and regular meetings with the project supervisor reduce the chance of project-related stress.	Very Low	No Control:			Very Low
The use of a computer, printer and other miscellaneous office appliances provide an electrical hazard risk.	Control: All equipment in the office environment is connected to an appropriately sized, surge protected power board.	Very Low	No Control:			Very Low
There is the risk of trip hazards in the office environment.	Control: The floorspace will be kept clear of all unnecessary items, and care will be exercised when moving around the environment.	Very Low	No Control:			Very Low
There is a residual fire risk within the office environment.	Control: Fire alarms are fitted and tested.	Very Low				Very Low